Walking droplets confined by applied or topographically-induced potentials: dynamics and stability

by

Lucas Dorigo Tambasco

Submitted to the Department of Mathematics
in partial fulfillment of the requirements for the degree of

Doctor of Philosophy

at the

MASSACHUSETTS INSTITUTE OF TECHNOLOGY

June 2018

Signature redacted

Author .....
Department of Mathematics
May 4, 2018

Signature redacted

Certified by ...
John W. M. Bush
Professor of Applied Mathematics
Thesis Supervisor

Signature redacted

Accepted by ...
Jonathan Kelner
Chairman, Department Committee on Graduate Theses

Walking droplets confined by applied or topographically-induced potentials: dynamics and stability

by

Lucas Dorigo Tambasco

Submitted to the Department of Mathematics
on May 4, 2018, in partial fulfillment of the
requirements for the degree of
Doctor of Philosophy

Abstract

In 2005, Yves Couder and coworkers discovered that a millimetric droplet of silicone oil may walk on the surface of a vertically-vibrating fluid bath, displaying features that were once thought to be peculiar to quantum mechanics. We here explore this hydrodynamic pilot-wave system through an integrated theoretical and experimental approach. We provide a theoretical characterization of the transition to chaos in orbital pilot-wave dynamics for droplets walking in the presence of a Coulomb, Coriolis, or central harmonic force. We proceed by investigating this hydrodynamic system above the Faraday threshold experimentally, with an aim of finding mechanisms to trap drops. We report a hydrodynamic analog of optical trapping with the Talbot effect, showing that drops may become trapped at the extrema of waves generated in the vicinity of a linear array of pillars. We also characterize the dynamics of droplets bouncing and walking above the Faraday threshold, indicating regimes of particle trapping and Brownian motion. We investigate the effect of bath topography in drop dynamics by considering a circular well that induces a circularly-symmetric Faraday wave pattern. In this regime, we show that droplets become trapped into stable circular orbits around the extrema of the well-induced wavefield. Finally, with a view to extending the phenomenological range of this hydrodynamic system, we consider a generalized pilot-wave framework, in which the relative magnitudes of dynamical parameters are altered relative to those relevant in the fluid system. In this generalized framework, we validate the theoretical result of Durey *et al.* relating the particle's mean wavefield to the emerging statistics, and characterizing the timescale of emergence of the statistically steady state for the chaotic pilot-wave dynamics.

Thesis Supervisor: John W. M. Bush
Title: Professor of Applied Mathematics

Acknowledgments

First and foremost, I would like to thank my advisor, John Bush, for introducing me to this project in my freshman year of undergraduate and keeping me around for the last nine years. I am very grateful for all these years working together, and for all the valuable discussions taking place anywhere from Santa Teresa to Taormina.

I would also like to thank my two incredible mentors, pioneers in the study of bouncing droplets, Dan Harris and Anand Oza. Dan Harris was my first mentor from my UROP days, introducing me to the rig and having the eternal patience to teach me how to do experiments. He has become much more than a mentor but a great friend. Anand was a constant source of motivation and inspiration: a Skype meeting with him was able to turn every major complication into a small bump, and every small success into a huge win. Thank you both for your vital support.

I would like to thank Luiz Faria and Giuseppe Pucci for the motivation and constant pushes towards the right direction; they assured everything kept running, despite all the challenges. Ruben Rosales, thank you for being there continuously, always having an answer, and many other stories. André Nachbin, thank you for hosting me at IMPA, the great experience with 18.04 and all the soccer we played together! I am proud of my great mentees, Jessica Pilgram and Paul Twijukye, and very thankful for their dedicated work. Thanks to an amazing group, Jonasz, Kristin, Juncal, Pedro, PT, Sam and Miles: you made every day at the office better and I couldn't have done it without you.

I would also like to acknowledge the Brazilian community at MIT, especially Ivo, Lara, Rosabelli and MISTI Brazil in general. It is great to have a home away from our home(country). I am grateful to all my friends in Brazil, especially Bruna Ferreira for your support since the beginning.

I could not have completed this without the support of all my family: aunts, uncles, cousins, and especially my grandparents, Chicho, Leninha, Hélio e Marly, muito obrigado por tudo. Special thanks to mom for the daily conversations, dad for your Polyanna way of seeing life, Bruno for every "pergunta que não quer calar," vô

for inspiring me into the academic life from a young age, and Gian for showing me what an incredible impact you can have on peoples' lives through teaching.

Finally, I would like to thank the unending support from Carol Guimarães. You have no idea how many times a simple text message from you made my day. I am extremely thankful for you being there for me even from afar, from the roughest patches to the happiest celebrations. You are capable of inspiring me to be my best and you push me to follow my passions. I am very lucky to have you by my side. Thank you for your tremendous patience to hear all my complaints and for your tremendous love and care.

Contents

List of Figures

List of Tables

Chapter 1

Introduction

> *"History shows that there long has been dispute over two viewpoints on the nature of light: corpuscular and undulatory; perhaps, however, these two are less at odds with each other than heretofore thought."*
>
> – Louis de Broglie, 1925 [18].

The nature of the interaction between particles and fields on both the macroscopic and microscopic scales has been a subject of interest for scientists for centuries. Examples include the interaction of fish schools and bird flocks with their suspending fluids, and the interaction of an electron with its self-induced electromagnetic field. Some such interactions remain unresolved. An inability to resolve dynamics on the microscopic scale has resulted in a number of quantum paradoxes, such as the wave-particle duality of an electron passing through a double slit. In most introductory quantum mechanics courses, one is invited to believe that electrons are neither particles, nor waves, but both (or neither), suggesting irreconcilable differences between the classical and quantum realms.

An underlying principle of classical mechanics is the concept of determinism as formalized by Newton in the late 1600s, and initially believed to hold at all scales. Determinism states that, given a complete set of initial conditions, a system's behavior can be determined entirely for all future time from the laws of physics. For example, planets and galaxies behave deterministically, obeying Newton's laws of gravitation

and following well-determined trajectories. However, determinism does not imply predictability, as noted by Henri Poincaré in 1908:

> *It may happen that small differences in the initial conditions produce very great ones in the final phenomena. [...] Prediction becomes impossible, and we have the fortuitous phenomenon* [87].

This lack of predicability is evident in many classical systems, from a double-pendulum [97] to gravitational systems of three or more bodies [56], to the weather [65]. It was only in the 1960s that the notion of chaotic dynamics was formalized: systems that are sensitive to initial conditions are not necessarily predictable [65]. This lack of predictability often means that one can do no better than a probabilistic prediction; for example, weather reports will only list the chance of rain for the following day. It is noteworthy that the advent of quantum mechanics took place 60 years prior to the development of chaos theory.

One of the pioneers of quantum theory, Louis de Broglie in 1925 [18] proposed a physical framework for understanding quantum mechanics. By equating the particle's rest mass energy m_0c^2 with the vibrational energy $\hbar\omega$, he proposed that each particle has an associated Compton frequency $\omega_C = m_0c^2/\hbar$, where m_0 is the particle's proper mass, c the speed of light, and $\hbar$ the reduced Planck's constant. He postulated that each particle has an internal vibration occurring at that frequency and that the particle moves in resonance with an underlying wave, a synchrony he referred to as the "harmony of phases" [20, 14]. For the case of a monochromatic wave, de Broglie derived the relation between a particle's momentum and its wavelength, $\boldsymbol{p} = \hbar\boldsymbol{k}$ (where $|\boldsymbol{k}| = 2\pi/\lambda$, and λ its de Broglie wavelength). Although de Broglie's relations, $\boldsymbol{p} = \hbar\boldsymbol{k}$ and $mc^2 = \hbar\omega$, were adopted into the mathematical framework of quantum mechanics, his realist interpretation of a particle moving in resonance with an underlying wave at the Compton frequency was largely discarded.

Schrödinger set out to derive the equation governing de Broglie's pilot-wave. He proposed that the pilot-wave was a solution of the Klein-Gordon equation, a relativis-

tic wave equation that obeys Lorentz invariance [95],

$$\frac{1}{c^2}\frac{\partial^2\Psi}{\partial t^2} + \nabla^2\Psi + \frac{m^2c^2}{\hbar^2}\Psi = 0. \tag{1.1}$$

One may decompose the solution to Eq. 1.1, $\Psi(\boldsymbol{x}, t)$, into a product of two terms: a term oscillating rapidly at the Compton frequency $\omega_C = mc^2/\hbar$, and a term $\psi(\boldsymbol{x}, t)$ that varies slowly relative to the Compton frequency. Considering the ansatz $\Psi(\boldsymbol{x}, t) = e^{i\omega_C t}\psi(\boldsymbol{x}, t)$, one obtains

$$i\hbar\frac{\partial}{\partial t}\psi = -\frac{\hbar^2}{2m}\nabla^2\psi + \frac{\hbar}{2\omega_C}\frac{\partial^2}{\partial t^2}\psi. \tag{1.2}$$

Provided the enveloping term ψ varies slowly relative to the Compton frequency, the last term in Eq. 1.2 is negligible, and Eq. 1.2 reduces to the Linear Schrödinger Equation (LSE), which describes the evolution of a free-particle wavefunction:

$$i\hbar\frac{\partial}{\partial t}\psi = -\frac{\hbar^2}{2m}\nabla^2\psi. \tag{1.3}$$

While originally derived by Schrödinger to describe the pilot-wave in de Broglie's mechanics, the wavefunction has since been adopted to describe the statistical behavior of quantum systems, with its squared modulus, $|\psi(\boldsymbol{x}, t)|^2$, indicating the probability density of measuring the particle at a given position. This probabilistic interpretation of the wavefunction has led to many successful predictions about quantum states, but also to a schism between quantum and classical mechanics.

According to the Copenhagen Interpretation of quantum mechanics, the wavefunction $\psi(\boldsymbol{x}, t)$ provides a complete description of an isolated quantum state. According to Bohr, one of the original proponents of the Copenhagen Interpretation:

> *The very fact that repetition of the same experiment [...] in general yields different recordings pertaining to the object, immediately implies that a comprehensive account of experience in this field must be expressed by statistical laws.* (1963) [10]

It is valuable to juxtapose Bohr's statement with that of Poincaré's regarding different

measurements of the "same" experiment. According to Bohr, this indeterminism implies that quantum mechanics is inherently probabilistic; for Poincaré, it simply implied sensitivity to initial conditions, a hallmark of chaos.

By claiming that the microscopic world was inherently probabilistic, and that the wavefunction provided a complete description of quantum systems, the Copenhagen Interpretation raised philosophical questions about the nature of reality. Critics of the Copenhagen Interpretation, including de Broglie, Schrödinger, and Einstein, expressed strong objections to the philosophical implications of the completeness of the statistical description of quantum mechanics. In particular, Einstein [35] saw a logical conflict between his theory of relativity and the Copenhagen interpretation: how could the wavefunction be delocalized instantaneously before measurement, and localized after? According to Einstein,

> *It seems hard to sneak a look at God's cards. But that he plays dice and uses "telepathic" methods (as the present quantum theory requires of him) is something that I cannot believe for a single moment* [27].

By "telepathic," or elsewhere "spooky action at a distance" [34], Einstein referred to the superluminal transmission of information that must accompany the act of measurement if one insists on the completeness of quantum mechanics. According to the Copenhagen Interpretation, measuring a particle at a specific position does not imply that the particle was there instantaneously before measurement, as one would expect classically. If the wavefunction is taken to be a complete description of the quantum system, there cannot be additional "hidden" variables, such as the particle's position or momentum. Thus, the particle is effectively smeared out over space with a density prescribed by a wavefunction, which collapses instantaneously to a point in response to the act of measurement.

In response to the philosophical difficulties introduced by the Copenhagen Interpretation, a myriad other quantum interpretations emerged, some even more philosophically extravagant. For instance, the Many-Worlds Interpretation developed by Hugh Everett in 1957 [36] and popularized by Bryce deWitt [25] claims that every

time a quantum measurement is made, all possible outcomes are realized. In order to account for the simultaneous realization of all outcomes, this interpretation relies on the metaphysical artifact of a "continual splitting of the universe into a multitude of mutually unobservable but equally real worlds..." [25]. According to the Many-Worlds Interpretation, there is a wavefunction, or state vector, which governs the entire universe, including all of the many worlds, and hence never collapses upon measurement [105]. An equally farfetched variant to the splitting of worlds comes in the form of the Many-Minds interpretation, presented by Michael Lockwood [64], which claims that

> *[A]ssociated with a sentient being at any given time, there is a multiplicity of distinct conscious points of view. [...] it is these conscious points of views or 'minds,' rather than 'worlds,' that are to be conceived as literally dividing or differentiating over time.*

While most physicists are agnostic concerning quantum foundations, recent polls at conferences on the subject indicate that the Copenhagen Interpretation and the Many-Worlds Interpretation are among the most widely ascribed to [96].

In the opposite direction, towards a more common-sensical interpretation of quantum mechanics, Max Born proposed the Statistical Interpretation of quantum mechanics, for which he obtained the Nobel prize in 1954. In his Nobel lecture [11], Born discussed the concept of determinism in classical and quantum mechanics,

> *Can absolute predictions really be made for all time on the basis of the classical equations of motion? It can easily be seen, by simple examples, that this is only the case when the possibility of absolutely exact measurement (of position, velocity, or other quantities) is assumed. [...] I should like only to say this: the determinism of classical physics turns out to be an illusion, created by overrating mathematico-logical concepts. It is an idol, not an ideal in scientific research and cannot, therefore, be used as an objection to the essentially indeterministic statistical interpretation of quantum mechanics.*

The statistical interpretation of quantum mechanics was extended by Ballentine [1] into the Ensemble Interpretation, which claims that the wavefunction describes an ensemble of similarly prepared systems, rather than a single isolated system. Through conceding that quantum mechanics does not provide a complete description of an isolated quantum system, the Ensemble Interpretation obviates the need for the philosophical extravagances that accompany the Copenhagen, Many-Worlds and Many-Minds interpretations. In particular, it does not require metaphysical artifacts such as branching worlds and minds, as presented in the Many-Worlds and Many-Minds interpretations. Likewise, it avoids the issues of wavefunction collapse and superluminal signaling that plague the Copenhagen Interpretation.

Finally, we consider the pilot-wave theory proposed by Bohm [7] in 1952, which included a trajectory interpretation for single-particle quantum systems. The Madelung transformation [66] casts the Linear Schrödinger Equation 1.3 in a hydrodynamic form, and so represents the original Hydrodynamic Interpretation of quantum mechanics. Substituting a wavefunction written in polar form, $\psi(\boldsymbol{x},t) = R(\boldsymbol{x},t)e^{iS(\boldsymbol{x},t)/\hbar}$, into the LSE and equating the real and imaginary parts yields

$$\begin{aligned} \frac{\partial S}{\partial t} - \frac{\hbar^2}{2m}\frac{\nabla^2 R}{R} + \frac{(\nabla S)^2}{2m} &= 0, \\ \frac{\partial R^2}{\partial t} + (\nabla S)\cdot\nabla R^2 + R^2\nabla\cdot(\nabla S) &= 0. \end{aligned} \tag{1.4}$$

One thus obtains a Hamilton-Jacobi description of quantum statistics. The square modulus of the wavefunction R^2 corresponds to the probability density, while the gradient of the action, ∇S prescribes the quantum velocity of probability $\boldsymbol{u} = \nabla S/m$. It is of note that there is only one term in Eq. 1.4 that contains Planck's constant $\hbar$,

$$Q = \frac{-\hbar^2}{2m}\frac{\nabla^2 R}{R}, \tag{1.5}$$

the so-called "quantum potential" [8]. Bohm [7] proposed to extract dynamics out of this formulation, by equating the particle velocity $\boldsymbol{v}_p$ to the quantum velocity of probability, $\boldsymbol{v}_p = \nabla S/m$. The trajectory of a particle of mass m subjected to a

classical potential V is thus governed by:

$$m\dot{v}_p = -\nabla Q - \nabla V \tag{1.6}$$

Bohm's proposal was important in providing a counterexample to the Impossibility Proofs that held sway at the time [75] and erroneously suggested the impossibility of a dynamical completion of quantum mechanics [2]. Bohm's formulation did not, however, provide a description of wave generation as envisioned by de Broglie in his "harmony of phases" picture, where a vibrating particle moves in resonance with a monochromatic guiding wave.

We here explore the first macroscopic realization of a pilot-wave system of the form envisioned by de Broglie: the walking droplet system. In a remarkable series of experiments, Yves Couder, Emmanuel Fort and collaborators discovered a hydrodynamic system in which a millimetric droplet of silicone oil walks on the surface of a vertically-vibrating fluid bath [17, 88]. The drop generates a monochromatic wave at each impact position, and that wave, in turn, guides the drop. This hydrodynamic pilot-wave system consists of a particle exchanging energy with a monochromatic wave at its vibrational frequency, as in de Broglie's pilot-wave theory. In the hydrodynamic case, the wave-particle interaction may be measured experimentally and modeled theoretically.

The walking droplet pilot-wave system exhibits many features that were once thought to be peculiar to quantum mechanics, including quantized orbits [41, 52, 61, 79, 86], Zeeman splitting [41, 79], spin states [79, 63, 81], double quantization [86, 28, 59], tunneling [31, 73], and the emergence of multimodal statistics in confined geometries [55, 42, 43, 94]. This hydrodynamic pilot-wave system and its relation to realist models of quantum mechanics has been recently reviewed by Bush [14, 13].

The experimental system consists of a millimetric droplet of radius R, bouncing in place [110] on the surface of a fluid bath vibrating vertically with vertical acceleration $\Gamma = \gamma \cos(2\pi f t)$. Provided the vibrational amplitude $\gamma < \gamma_F$, where γ_F is the Faraday instability [3] threshold, the surface would remain flat in the absence of

the drop. When the bouncing drop becomes synchronized with its wavefield, its bouncing period corresponds to the Faraday period $T_F = 2/f$, and it is said to be a resonant bouncer. Then, at each impact, it generates a localized field of Faraday waves with characteristic wavelength $\lambda_F = 2\pi/k_F$ prescribed by the standard water-wave dispersion relation [58],

$$\left(\frac{\omega}{2}\right)^2 = \left(gk + \frac{\sigma}{\rho}k^3\right)\tanh kh, \tag{1.7}$$

where ω is the driving frequency, g the acceleration due to gravity, σ the surface tension, ρ the density, and h the fluid depth.

As the vibrational amplitude is increased, the bouncing state destabilizes into a walking state, as shown by Yves Couder, Emmanuel Fort and collaborators [17, 88]. The characterization of the droplet dynamics in terms of the non-dimensional vibrational acceleration γ/γ_F and vibration number $\Omega = \omega/\sqrt{\sigma/(\rho R^3)}$ is shown in Fig. 1-1 for 20 cS oil and vibration frequency 80 Hz [71, 72]. In the absence of vertical vibration, all drops coalesce into the fluid bath. As the vibrational acceleration is increased progressively, the drop passes through a variety of static bouncing states. Once its bouncing period has doubled with respect to the bath vibration period, the drop achieves resonance with its underlying subharmonic Faraday wavefield. Beyond the walking threshold, this resonant bouncer destabilizes into a dynamic state. The resulting walker self-propels along the bath surface, guided by its own wavefield. Exotic bouncing and walking states were reported by Wind-Willassen *et al.* [115]. In Chapter 4, we consider an extension of this regime diagram for vibrational accelerations above the Faraday threshold γ_F.

Moláček & Bush [71, 72] developed a theoretical description of the vertical and horizontal motion of the walking drops by considering the long-time many-bounces approximation to the wave generated by droplet impact. The vertical motion of the droplet is characterized in terms of free-flight when the drop is not in contact with the bath, and impact, during which the interface behaves like a logarithmic spring [71, 72]. The wavefield is expressed as a discrete sum of Bessel functions weighted by a temporal

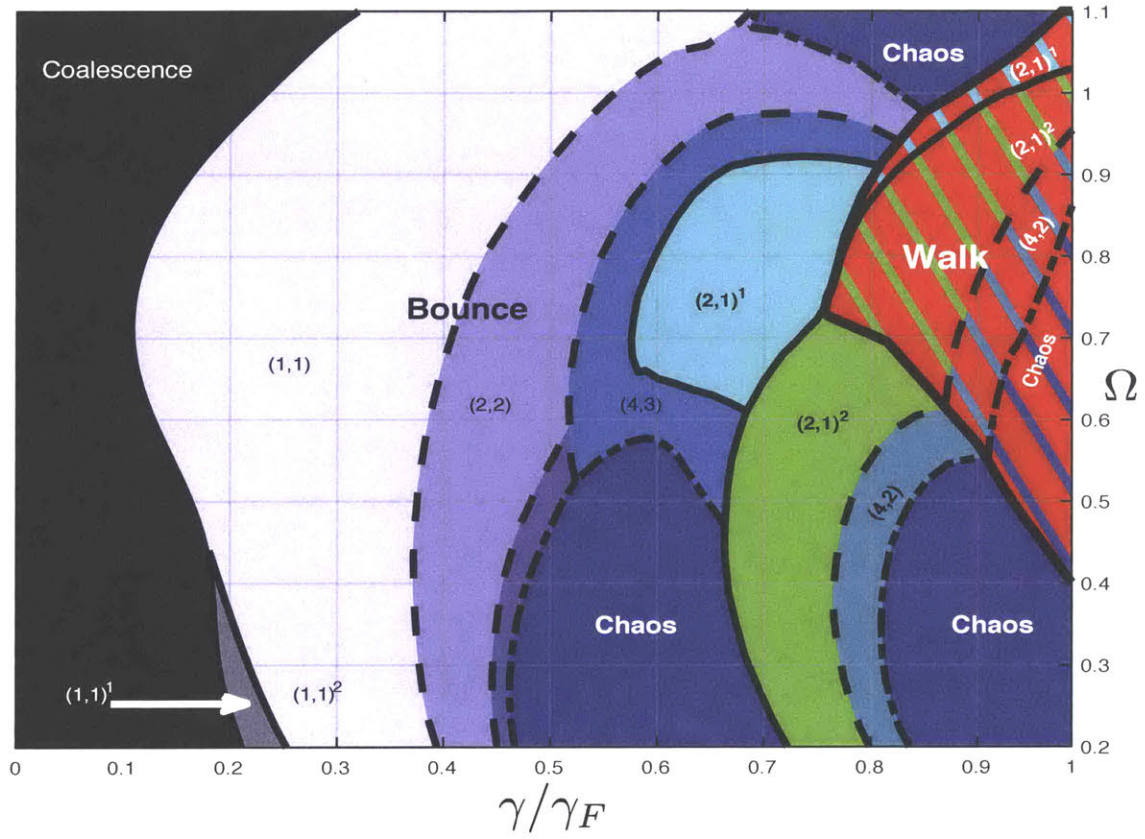

Figure 1-1: Regime diagram for 20 cS silicone oil droplets bouncing and walking on the surface of a bath vibrating vertically at 80 Hz, as a function of the non-dimensional vibrational acceleration γ/γ_F and vibration number $\Omega = \omega/\sqrt{\sigma/(\rho R^3)}$ [71]. The bouncing mode, denoted by $(m, n)^p$, indicates that for every every m driving periods, the particle will bounce n times [44]. We distinguish different bouncing states with the same mode number according to energy, with higher values of p corresponding to more energetic modes [71, 106]. The behavior of droplets above the Faraday threshold is reported in Chapter 4.

damping term that depends on the vibrational acceleration, with each individual wave mode solving a damped Matthieu equation [72]. By considering that there is a dominant unstable wave mode with wavenumber $k = k_F$, Moláček & Bush [72] asymptotically obtained an analytical expression for the wave form in terms of the fluid parameters.

Building upon the modeling efforts of Moláček & Bush [71, 72], Oza *et al.* [80] developed an integro-differential trajectory equation to describe the walker's horizontal motion. When the vertical dynamics is fast relative to the horizontal dynamics, the discrete sum of waves may be expressed in terms of a continuous integral equation for the wavefield. The propulsive force on the droplet is then prescribed by the gradient of the underlying wavefield. The resulting trajectory equation, henceforth the "stroboscopic model," is able to capture the supercritical pitchfork bifurcation from bouncing to walking, and the stability of straight-line walking solutions: specifically, straight-line trajectories are stable to perturbations along the direction of motion, and neutrally stable to perpendicular perturbations.

The first theoretical model for the horizontal motion was proposed by Emmanuel Fort []. Refined models of the wavefield have recently been developed by Milewski *et al.* [70], Blanchette [6], Oza *et al.* [82], Faria [38], and Durey *et al.* [28]. A reduced dynamical model for the horizontal dynamics of a constrained walker has been developed by Gilet [42] and examined by Rahman & Blackmore [91]. The various wave models have been recently reviewed by Turton *et al.* [108].

Experimental explorations of orbital pilot-wave dynamics have provided analogs to various quantum systems. For example, Fort *et al.* [41], demonstrated experimentally the quantization of circular orbital radii for walkers in a rotating bath. Since the Coriolis force is identical in form to the Lorentz force acting on a charged particle moving through a uniform magnetic field, the authors drew the physical analogy between their quantized inertial orbits and Landau levels in quantum mechanics. Harris *et al.* [52] demonstrated experimentally that quantized orbits in the rotating frame may become unstable, and eventually chaotic. In an accompanying theoretical study, Oza *et al.* [79] performed a linear stability analysis of orbital solutions to the

stroboscopic trajectory equation in a rotating frame, predicting that all circular orbits are stable for sufficiently low vibrational acceleration, but eventually become unstable as the acceleration increases progressively. In the chaotic regime, the drop moves in an aperiodic fashion, but coherent quantum-like statistics emerges, where traces of the unstable orbital modes are evident.

Perrard *et al.* [86] examined experimentally the dynamics of walking droplets subjected to a central harmonic potential. The resulting drop trajectories exhibited double quantization in radial position and angular momentum. At large vibrational forcing, chaotic trajectories arose [85], in which the particle erratically switched between unstable periodic orbits. Labousse *et al.* [61] considered theoretically the stability of circular orbits in a simple harmonic potential, characterizing the radial quantization of circular trajectories. The rich dynamical behavior of walkers in a harmonic potential has also been explored numerically [61, 28, 59], where exotic orbits including lemniscates and trefoils are observed, as in experiments. Although chaotic dynamics are evident experimentally for both walker motion in a rotating frame and in the presence of a simple harmonic potential, the detailed transition from periodic to chaotic trajectories had not yet been examined. We characterize this transition theoretically in Chapter 2, using the stroboscopic model of Oza *et al.* [80].

This thesis is motivated by the following questions:

1. Might chaotic pilot-wave dynamics underlie quantum statistics?

2. What is the mechanism for the emergence of chaos in orbital pilot-wave dynamics?

3. Can the stroboscopic model be generalized theoretically to capture and elucidate additional quantum analogs?

In Chapter 2, we explore the onset of chaos in orbital pilot-wave dynamics. We conduct a numerical investigation of droplets walking on a vertically-vibrating bath and acted upon by either a Coriolis, Coulomb or linear spring force. As the vibrational acceleration is increased progressively, circular orbits tend to destabilize into

wobbling, and eventually chaotic trajectories. The manner in which chaos appears, however, is dependent on the form of the external force. When acted upon by Coriolis or Coulomb forces, the orbital trajectories undergo a period-doubling cascade leading to chaos. In the presence of a linear spring force, the transition to chaos is reminiscent of the Ruelle-Takens-Newhouse scenario. These results have been published in: "The onset of chaos in orbital pilot-wave dynamics," L. D. Tambasco, D. M. Harris, A. U. Oza, R. R. Rosales, and J. W. M. Bush, Chaos **26**, 103107 (2016) [103].

In Chapter 3, we examined experimentally the ability to trap walking droplets with an underlying wavefield. We first explored a novel optical analogy, the Faraday-Talbot effect: when a row of equally-spaced pillars is placed on a vibrating fluid bath driven above the Faraday threshold, the resulting wavefield is marked by images of the pillars projected at integer multiples of a fixed distance from the row, provided that the spacing between the pillars is a multiple of the Faraday wavelength. This underlying wavefield is shown to attract both bouncing and walking droplets to its troughs, similar to a potential field. The Faraday-Talbot effect and droplet trapping were first reported in: "Hydrodynamic analog of particle trapping with the Talbot effect," N. Sungar, L. D. Tambasco, G. Pucci, P. J. Sáenz, and J. W. M. Bush, Physical Review Fluids **2**, 103602 [100], and further extended for the cases of alternating phase and circular arrays in: "Faraday-Talbot effect: alternating phase and circular arrays," N. Sungar, J. P. Sharpe, J. J. Pilgram, J. Bernard and L. D. Tambasco, (Submitted, 2018) [99]. These experiments motivated our experimental and theoretical exploration of droplet dynamics subjected to a topographically-induced wavefield.

In Chapter 4, we explored the horizontal dynamics of droplets driven above the Faraday threshold, extending the regime diagram for droplets of 20 cS and 50 cS. Above threshold, we observed that straight-line walking is unstable, with drops moving in meandering, zig-zagging, and chaotic trajectories, or otherwise becoming trapped by the underlying wavefield. We investigated the chaotic trajectories, where drops appear to exhibit Brownian motion, and we experimentally showed that the effective diffusivity of the drops increases with vibrational acceleration and decreases with drop radius. This chapter was submitted for publication as: "Bouncing droplet

dynamics above the Faraday threshold," L. D. Tambasco, J. J. Pilgram and J. W. M. Bush, (Submitted, 2018) [104].

In Chapter 5, we explored the effects of an imposed potential with both oscillatory and quadratic components on the dynamics of walking droplets. We first conducted an experimental investigation of droplets walking on a bath with a central circular well. The well acts as a source of Faraday waves that may serve to trap walking droplets into circular orbits. The observed orbits are stable and quantized, with the preferred radii aligning with the extrema of the well-induced Faraday wave pattern. We then used the stroboscopic model of Oza *et al.* with an added potential to examine the interaction of the droplet with the underlying well-induced wavefield. We showed that quantized orbits are stable for accessible fluid parameters. We proceeded by considering a generalized pilot-wave system, in which the relative magnitudes of the pilot-wave force and drop inertia may be tuned. When the drop inertia is dominated by the pilot-wave force, the quantized circular orbits may all become unstable, with the drop chaotically switching between them. The probability distribution of the drop's position then reflects the relative instability of the circular orbits. This chapter was submitted for publication as: "Exploring orbital dynamics and trapping with a generalized pilot-wave framework," L. D. Tambasco and J. W. M. Bush (Submitted, 2018) [102].

Finally, in Chapter 6, we summarize our findings and discuss future directions in the theoretical and experimental study of pilot-wave dynamics.

Chapter 2

Chaos in orbital pilot-wave dynamics

In this chapter, we detail the manner in which stable circular orbits, for walking droplets in the presence of Coriolis, linear spring or Coulomb forces, give way to chaotic trajectories as the forcing acceleration is increased progressively. Orbital pilot-wave dynamics were first examined by Fort *et al.* [41], who demonstrated experimentally the quantization of orbital radii for walkers in a rotating frame, and rationalized this quantization with accompanying simulations. Owing to the identical forms of the Coriolis force acting on a mass moving in a rotating frame and the Lorentz force acting on a charge in a uniform magnetic field, the authors drew the analogy between these quantized inertial orbits and Landau levels in quantum mechanics. Harris & Bush [52] demonstrated experimentally that these quantized circular orbits can destabilize into wobbling and chaotic trajectories, features captured in the theoretical models of Oza *et al.* [80, 83].

Perrard *et al.* [86] explored walkers in a harmonic potential, and reported a double quantization of orbital radius and angular momentum, features also captured in their simulations [61]. In both of these orbital pilot-wave systems, the walker dynamics becomes complex and presumably chaotic for sufficiently high forcing acceleration γ. Nevertheless, traces of the unstable orbital solutions are evident in the emergent chaotic trajectories, which exhibit multimodal quantum-like statistics.

These results have been published in: "The onset of chaos in orbital pilot-wave dynamics," L. D. Tambasco, D. M. Harris, A. U. Oza, R. R. Rosales, and J. W. M. Bush, Chaos **26**, 103107 (2016) [103].

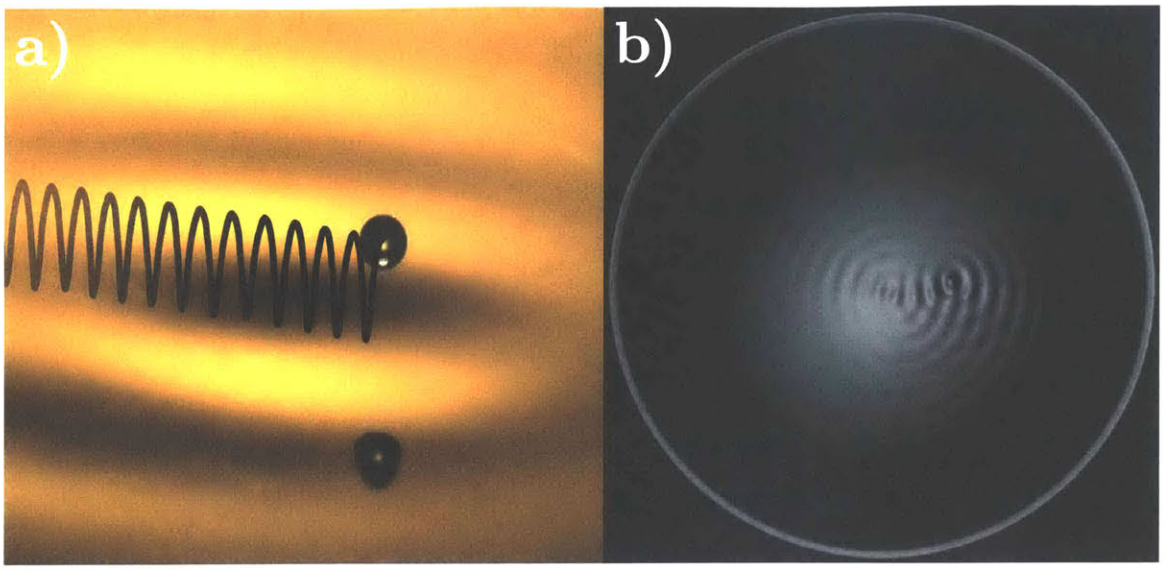

Figure 2-1: (a) Oblique view of a resonant walker [13]. The solid line tracks the center of the walking droplet. (b) Top view of a walking droplet orbiting on a rotating bath [52], a system to be explored numerically in Section 2.2.

In Section 2.1, we review the theoretical stroboscopic model for the horizontal dynamics of walking droplets, and discuss the numerical method used to simulate the drop's trajectories. We present the evolution from circular orbits to chaotic trajectories for drops subject to Coriolis (Section 2.2), linear spring (Section 2.3) and Coulomb (Section 2.4) forces. In Section 2.5 we discuss the two routes to chaos observed, specifically the classic period-doubling cascade for orbits in the presence of Coriolis and Coulomb forces, and a path to chaos reminiscent of the Ruelle-Takens-Newhouse scenario for orbital dynamics in the presence of a linear spring force.

2.1 Trajectory equation and numerical method

We first summarize the stroboscopic trajectory equation of Oza *et al.* [80] which forms the basis of our numerical investigation. We consider a resonant walker of mass m, bouncing with frequency $f/2$ on a vertically vibrated fluid bath shaken with forcing acceleration $\gamma \cos(2\pi f t)$ and subjected to an applied force $\boldsymbol{\mathcal{F}}$. We denote its horizontal position at time t by $\boldsymbol{x}_p(t) = (x_p(t), y_p(t))$. As shown by Moláček & Bush [72] and Oza *et al.* [80], time-averaging the vertical dynamics leads to the

Symbol	Definition	Typical Range of Values
R	Drop radius	0.1 – 0.5 mm
ν	Drop kinematic viscosity	20–50 cS
μ	Drop dynamic viscosity	10^{-3}–10^{-1} kg m^{-1} s^{-1}
μ_a	Air dynamic viscosity	10^{-5} kg m^{-1} s^{-1}
σ	Drop surface tension	20-21 mN m^{-1}
ρ	Silicone oil density	949-960 kg m^{-3}
g	gravitational acceleration	9.81 m s^{-2}
γ	forcing acceleration	0 – 60 m s^{-2}
γ_F	Faraday threshold acceleration	40 – 50 m s^{-2}
f	Bath shaking frequency	50–80 Hz
T_F	(= 2/f) Faraday period	.025 – 0.04 s^{-1}
ω	(=$2\pi f$) Shaking angular frequency	314–504 rad s^{-1}
ω_F	(=$\omega/2$) Faraday frequency	107–252 rad s^{-1}
h	Fluid depth	1–6 mm
λ_F	Faraday wavelength	4.75 – 6 mm
k_F	(=$2\pi/\lambda_F$) Faraday wavenumber	167 – 210 m^{-1}

Table 2.1: List of symbols for dimensional variables, along with typical range of experimental values explored.

integro-differential equation for the horizontal motion:

$$m\ddot{\boldsymbol{x}}_p + D\dot{\boldsymbol{x}}_p = -mg\boldsymbol{\nabla}h(\boldsymbol{x}_p(t), t) + \boldsymbol{\mathcal{F}}, \tag{2.1}$$

with the wavefield

$$h(\boldsymbol{x}, t) = \frac{A}{T_F}\int_{-\infty}^{t} J_0\left(k_F\left|\boldsymbol{x} - \boldsymbol{x}_p(s)\right|\right) \mathrm{e}^{-(t-s)/T_M}\,\mathrm{d}s,$$

where g is the gravitational acceleration, $T_F = 2/f$ is the Faraday period, and $k_F = 2\pi/\lambda_F$ is the wavenumber of the most unstable Faraday wave. We assume that the fluid bath consists of silicone oil with viscosity $\nu = 20$ cS, driven at $f = 80$ Hz, and that the walker has radius $R_D = 0.4$ mm and mass $m = 0.25$ mg. For this particular case, the time-averaged drag $D = 2.0$ mg/s and the wave amplitude $A = 3.5$ μm were calculated from system parameters [72, 80]. We note that A depends on the droplet's bouncing phase Φ, chosen such that $\sin\Phi = 0.2$ to provide the best fit between predicted and observed walking speeds [80]. Typical range of experimental

parameters is reported in Table 2.1.

In addition to the applied force $\boldsymbol{\mathcal{F}}$, the walker experiences a drag force opposing its motion and a propulsive force proportional to the local slope of the interface. The wavefield h is expressed as the sum of waves generated by all prior droplet impacts. Contributions to the wavefield from previous impacts are exponentially damped over the memory timescale $T_M = T_d/(1-\gamma/\gamma_F)$, where T_d is the wave decay time in the absence of forcing [72, 32]. Note that the memory time is a monotonically increasing function of the forcing acceleration for $\gamma < \gamma_F$, so we will use the terms memory and vibrational forcing interchangeably in what follows.

We non-dimensionalize according to $\hat{\boldsymbol{x}} \to k_F \boldsymbol{x}$, $\hat{t} \to t/T_M$ and $\hat{\boldsymbol{\mathcal{F}}} \to k_F T_M \boldsymbol{\mathcal{F}}/D$. Dropping carets yields the dimensionless system:

$$\begin{aligned} \kappa \ddot{\boldsymbol{x}}_p + \dot{\boldsymbol{x}}_p &= -\beta \boldsymbol{\nabla} h(\boldsymbol{x}_p(t), t) + \boldsymbol{\mathcal{F}}, \\ h(\boldsymbol{x}, t) &= \int_{-\infty}^{t} J_0\left(|\boldsymbol{x} - \boldsymbol{x}_p(s)|\right) \mathrm{e}^{-(t-s)} \, \mathrm{d}s, \end{aligned} \tag{2.2}$$

where $\kappa = m/DT_M$ and $\beta = mgAk_F^2 T_M^2/DT_F$. This system is solved numerically by a fourth-order Adams-Bashforth linear multistep method, the details of which are reported elsewhere [83]. We initialize the simulations in a circular orbit, $\boldsymbol{x}_p(t) = r_0\left(\cos(\omega t), \sin(\omega t)\right)$, where the orbital radius r_0 and angular frequency ω are solutions of the algebraic equations

$$\begin{aligned} -\kappa r_0 \omega^2 &= \beta \int_0^\infty J_1\left(2r_0 \sin\frac{\omega z}{2}\right) \sin\frac{\omega z}{2} \mathrm{e}^{-z} \, \mathrm{d}z + \boldsymbol{\mathcal{F}} \cdot \hat{\boldsymbol{r}}, \\ r_0 \omega &= \beta \int_0^\infty J_1\left(2r_0 \sin\frac{\omega z}{2}\right) \cos\frac{\omega z}{2} \mathrm{e}^{-z} \, \mathrm{d}z + \boldsymbol{\mathcal{F}} \cdot \hat{\boldsymbol{\theta}}, \end{aligned} \tag{2.3}$$

where $\hat{\boldsymbol{r}}$ and $\hat{\boldsymbol{\theta}}$ are the unit vectors in the radial and tangential directions respectively. Eq. (2.3) guarantees that $\boldsymbol{x}_p(t) = r_0\left(\cos(\omega t), \sin(\omega t)\right)$ is an exact solution of Eq. (2.2), which is stable for sufficiently low forcing acceleration γ/γ_F. After initializing the simulation in a stable circular orbit, we increase the forcing acceleration in increments

of $\Delta(\gamma/\gamma_F)$, using the results from the previous simulation as the initial data. In order to resolve the bifurcations, we adapt the step value $\Delta(\gamma/\gamma_F)$, decreasing it as γ/γ_F increases. Each simulation is run using a dimensionless time step $\Delta t = 2^{-6}$ and up to a dimensionless time $t/T_M = 10^4$ in order to integrate beyond any transient behaviors.

2.2 Coriolis force

We first consider the pilot-wave dynamics of a walking droplet in a frame rotating with angular frequency $\boldsymbol{\Omega} = \Omega\hat{\boldsymbol{z}}$. The walker experiences a Coriolis force, $\boldsymbol{\mathcal{F}} = -2m\boldsymbol{\Omega} \times \dot{\boldsymbol{x}}_p$, which assumes the dimensionless form $\boldsymbol{\mathcal{F}} = -\hat{\boldsymbol{\Omega}} \times \dot{\boldsymbol{x}}_p$, where $\hat{\boldsymbol{\Omega}} = 2m\boldsymbol{\Omega}/D$. It was demonstrated in prior experiments [41, 52] that, in certain parameter regimes, the walkers execute circular orbits in the rotating frame of reference, $\boldsymbol{x}_p(t) = r_0(\cos\omega t, \sin\omega t)$. Above a critical value of the forcing acceleration, certain radii are forbidden; thus, the stable orbits are quantized in radius, roughly separated by half-integer multiples of the Faraday wavelength λ_F. The linear stability of the system, as elucidated by Oza *et al.* [79], is summarized in Fig. 2-2. Laboratory experiments [52] and numerical simulations [83, 51] revealed that, as the forcing acceleration is progressively increased, the quantized circular orbits destabilize into wobbling orbits, characterized by a periodic oscillation in the radius of curvature. As the memory is increased further, wobbling orbits then destabilize into drifting orbits, in which the orbital center drifts on a time scale that is long relative to the orbital period. Above a critical value of memory, the orbital dynamics becomes chaotic. We here characterize the progression from wobbling to drifting to chaotic dynamics as the memory is increased progressively.

Since the applied force is the Coriolis force, the circular orbits are not necessarily centered at the origin, so we cannot characterize the orbits simply by the radius $r(t) = |\boldsymbol{x}_p|$. We instead use the radius of curvature $R(t) = |\dot{\boldsymbol{x}}_p|^3 / |\dot{\boldsymbol{x}}_p \times \ddot{\boldsymbol{x}}_p|$. Fig. 2-3 shows the trajectories obtained by numerically integrating Eq. (2.2) for a fixed dimensionless rotation rate $\hat{\Omega} = 0.6$ and progressively increasing memory. The resulting

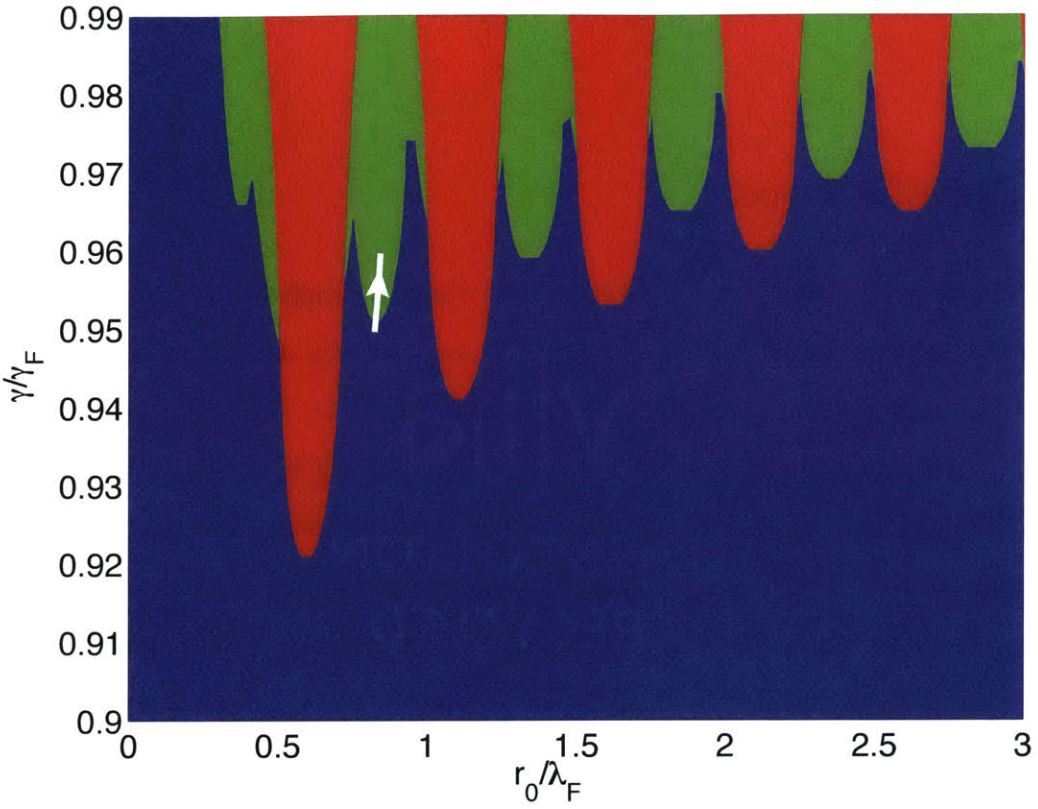

Figure 2-2: Linear stability diagram [79] of orbital solutions of radius r_0 arising in the presence of a Coriolis force $\boldsymbol{\mathcal{F}} = -2m\boldsymbol{\Omega} \times \dot{\boldsymbol{x}}_p$. γ is the driving acceleration, γ_F is the Faraday threshold and λ_F is the Faraday wavelength. The droplet's radius is $R_D = 0.4$ mm, impact phase $\sin\Phi = 0.2$, viscosity $\nu = 20$ cS and forcing frequency 80 Hz. Blue regions indicate stable circular orbits. Green regions correspond to circular orbits that destabilize via an oscillatory instability. Red regions correspond to orbits that destabilize via a nonoscillatory instability. The transition to chaos is found by starting with an initially stable solution (r_0, ω, Ω) to Eq. (2.3) and increasing the dimensionless forcing acceleration γ/γ_F progressively while keeping Ω constant, following the procedure described in Section 2.1. The white curve indicates the path through parameter space for the results shown in Section 2.2. The transition to chaos through a period-doubling cascade appears to be generic in this system; specifically, it arises in passing from blue to green regions with increasing memory.

path through parameter space is indicated by the white curve in Fig. 2-2. In this parameter regime, the circular orbits have radius $r_0 \sim 0.8\lambda_F$ and period $T \sim 6T_M$. The linear stability analysis [79] of these orbits (see Fig. 2-2) indicates that they are stable for $\gamma/\gamma_F < 0.951$.

For $\gamma/\gamma_F \gtrsim 0.951$, the circular orbit destabilizes into a wobbling orbit with an oscillatory radius of curvature $R(t)$, as shown in Fig. 2-3(a). The frequency spectrum of $R(t)$ shows a single peak at the wobbling frequency $\omega_{\text{wobble}} \approx 2\omega$. As the memory is increased, the wobbling orbits destabilize into drifting orbits, where the radius of curvature $R(t)$ evidently undergoes a period-doubling bifurcation. These drifting orbits consist of roughly circular loops of radius $\mathcal{O}(r_0)$ and orbital period $T \approx 2\pi/\omega$ that slowly drift, such as those highlighted in red in the first column of Fig. 2-3(b)-(e). Since the drifting is slow relative to T, we can define the orbital center for any loop:

$$\boldsymbol{x}_c(t) \equiv \frac{1}{T}\int_t^{t+T} \boldsymbol{x}_p(s)\,\mathrm{d}s, \tag{2.4}$$

where T corresponds to the strongest peak in the power spectrum of $\boldsymbol{x}_p(t)$.

The orbital center for drifting orbits traces a circle on a timescale long relative to the orbital period ($t_{\text{drift}} \sim 100T$). Fig. 2-3(c) shows a period-4 drifting orbit at a still higher value of memory, which is confirmed by the presence of additional frequencies and their integer linear combinations in the frequency spectrum of $R(t)$. As the memory is increased progressively, the trajectories undergo a period-doubling cascade and eventually become chaotic, as suggested by the broadband frequency spectrum of $R(t)$ evident in Fig. 2-3(d). As one might expect, the trajectory of the orbital center $\boldsymbol{x}_c(t)$ is aperiodic for chaotic orbits.

Within the regime of chaotic trajectories, $\gamma/\gamma_F \geq 0.95994$, we observe a periodic window consisting of period-10 orbits, an example of which is shown in Fig. 2-3(e). The period-doubling cascade observed along the white path shown in Figure 2-2 is analogous to that seen in 1-dimensional unimodal maps. As the forcing acceleration is increased beyond the white curve, our system departs from the behavior of unimodal maps. In particular, we do not observe period-3 or period-5 windows for the parame-

ters explored herein, but instead observe exotic orbits. An extensive numerical study of these exotic orbits in the case of a rotating frame is presented in Oza *et al.* [83].

The period-doubling cascade may be seen more clearly in the bifurcation diagram shown in Fig. 2-4. The points shown correspond to local maxima $R_m > r_0$ in the radius of curvature $R(t)$, corresponding to the circles in the plots of $R(t)$ (middle column of Fig. 2-3). We note that the trajectory has secondary local maxima that are present throughout the period-doubling cascade and do not seem to affect it. Similar period-doubling cascades were observed for paths crossing from blue to green regions with increasing memory for other values of $\hat{\Omega}$ and larger values of the initial orbital radius r_0.

We now provide a qualitative explanation for why the period-doubling bifurcation coincides with the transition from wobbling to drifting orbits. Consider a simple model for a wobbling orbit, $\boldsymbol{x}_p(t) = r_0(1 + a_0 \cos \alpha\omega t)(\cos \omega t, \sin \omega t)$, where a_0 is the wobbling amplitude and $\alpha\omega$ the wobbling frequency. Our linear stability analysis [79] has shown that circular orbits destabilize into wobbling orbits via a Hopf bifurcation as the memory is progressively increased, and that the most unstable eigenvalues have imaginary part $\pm\alpha\omega$ with $\alpha \approx 2$. The linear theory only provides an estimate for the wobbling frequency near the onset of wobbling, but the numerical simulations in Fig. 2-3(a) confirm that the wobbling frequency is indeed approximately 2ω.

A simple model for a period-doubled orbit is thus given by

$$\boldsymbol{x}_p(t) = r_0 \left[1 + a_0 \cos(\alpha\omega t) + a_1 \cos(\alpha\omega t/2)\right] (\cos \omega t, \sin \omega t), \tag{2.5}$$

where a_0 is the wobbling amplitude and a_1 is the amplitude of the new period-doubled frequency. Note that, because α is close to 2, $\boldsymbol{x}_p(t)$ will consist of loops that do not close. Plugging the expression for $\boldsymbol{x}_p(t)$ into Eq. (2.4) yields an expression for the orbital center of the trajectory:

$$\boldsymbol{x}_c(t) = \frac{r_0}{2} \sum_{i=0}^{1} \sum_{j=0}^{1} a_i \frac{\sin \pi\beta_{ij}}{\pi\beta_{ij}} \left(\cos\left[\beta_{ij}\Theta(t)\right], \sin\left[\beta_{ij}\Theta(t)\right]\right), \tag{2.6}$$

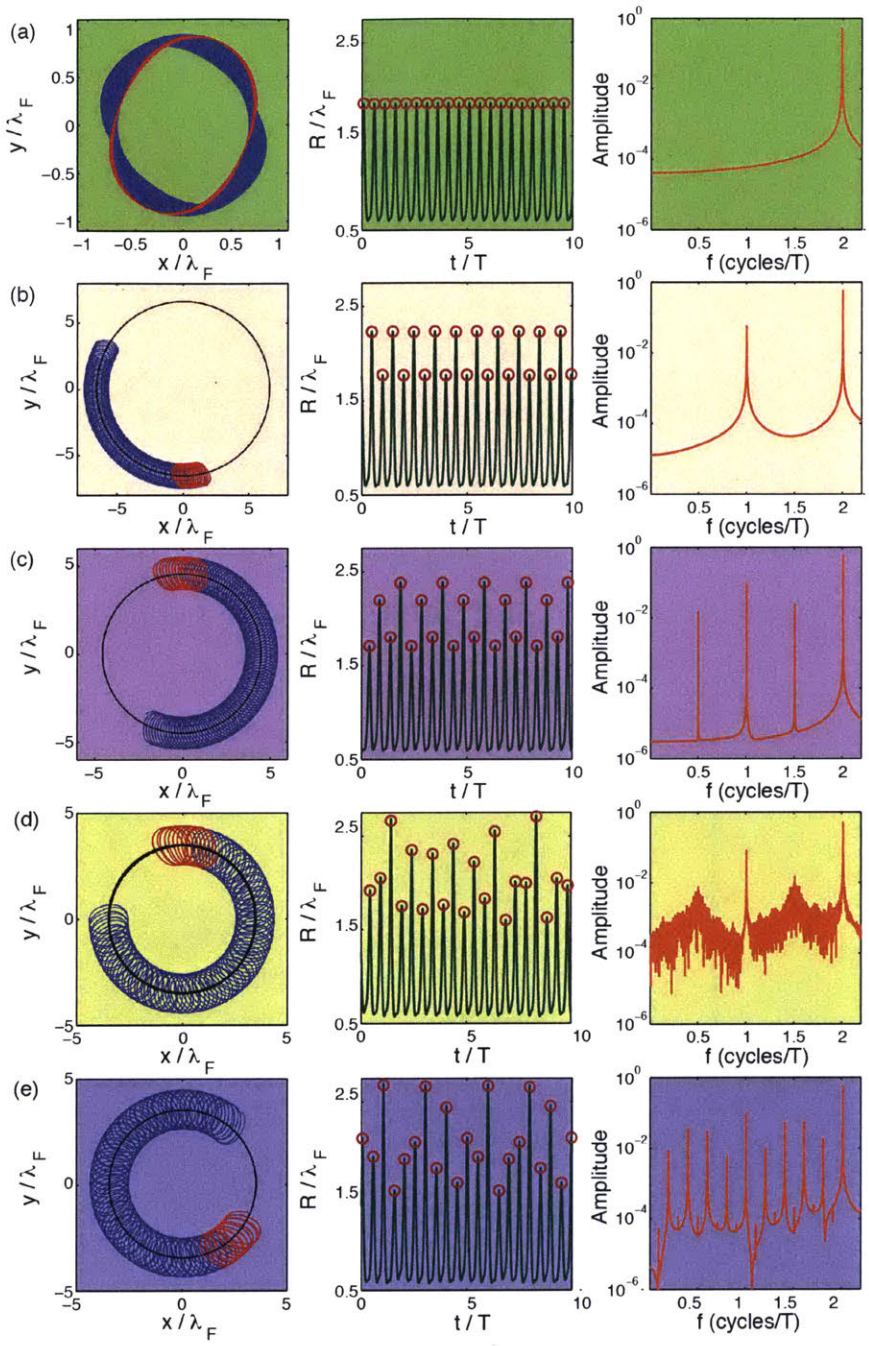

Figure 2-3: Numerical solutions to the trajectory equation (Eq. 2.2) with a Coriolis force $\boldsymbol{\mathcal{F}} = -\hat{\boldsymbol{\Omega}} \times \dot{\boldsymbol{x}}_p$, which describes pilot-wave dynamics in a rotating frame with dimensionless angular frequency $\hat{\Omega} = 0.6$. The first column shows the simulated trajectories $\boldsymbol{x}_p(t)$ plotted over 100 orbital periods T (blue), with the last 10 orbital periods (red) and the orbital center $\boldsymbol{x}_c(t)$ (black) superimposed. The second column shows the radius of curvature $R(t)$, with the local maxima greater than r_0 indicated by the red circles. The third column shows the frequency spectrum of $R(t)$. The rows correspond to (a) a wobbling orbit ($\gamma/\gamma_F = 0.957$), (b) a period-2 drifting orbit ($\gamma/\gamma_F = 0.959$), (c) a period-4 drifting orbit ($\gamma/\gamma_F = 0.9595$), (d) a chaotic trajectory ($\gamma/\gamma_F = 0.96004$), and (e) a period-10 orbit ($\gamma/\gamma_F = 0.960066$) in a periodic window within the chaotic regime.

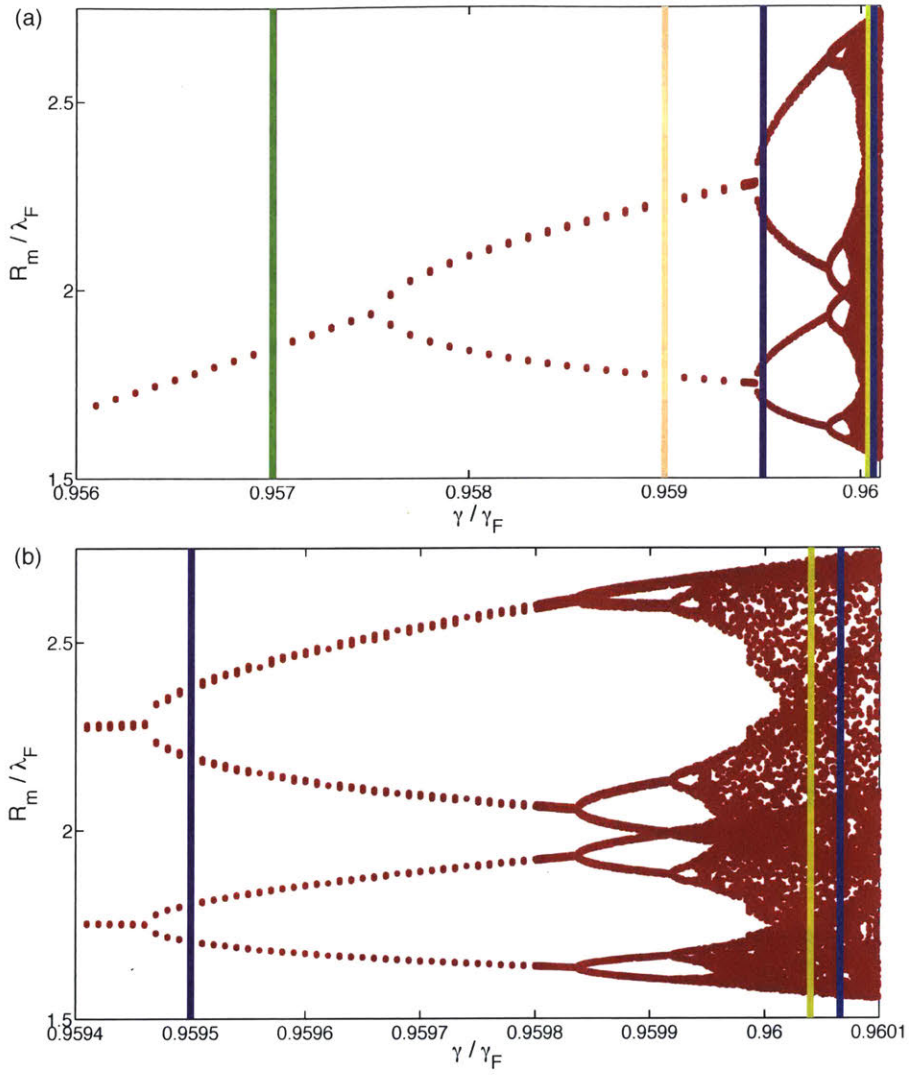

Figure 2-4: Bifurcation diagrams showing the transition to chaos for a walker in a rotating frame with dimensionless angular frequency $\hat{\Omega} = 0.6$. For each value of the dimensionless forcing acceleration γ/γ_F, the points correspond to local maxima R_m in the radius of curvature $R(t)$. Panel (b) shows a magnified view illustrating the period-doubling cascade for $\gamma/\gamma_F > 0.9594$. The color-coded vertical lines correspond to the trajectories shown in Fig. 2-3. The dimensionless forcing acceleration is changed in increments of $\Delta(\gamma/\gamma_F) = 10^{-3}$ for $\gamma/\gamma_F \in [0.950, 0.956]$, $\Delta(\gamma/\gamma_F) = 10^{-4}$ for $\gamma/\gamma_F \in [0.9561, 0.9594]$, $\Delta(\gamma/\gamma_F) = 10^{-5}$ for $\gamma/\gamma_F \in [0.95941, 0.95980]$ and $\Delta(\gamma/\gamma_F) = 10^{-6}$ for $\gamma/\gamma_F \in [0.959801, 0.960099]$.

where $\Theta(t) = \omega t + \pi$ and $\beta_{ij} = \alpha/2^i + (-1)^j$. Because $\alpha \approx 2$, $\beta_{00} \approx 3$, $\beta_{10} \approx 2$, $\beta_{01} \approx 1$ and $\beta_{11} \approx 0$. Hence, the coefficients $\sin(\pi\beta_{ij})/\pi\beta_{ij}$ in Eq. (2.6) all nearly vanish, except for that corresponding to β_{11}, which leads to

$$\boldsymbol{x}_c(t) \approx -\frac{1}{2} a_1 r_0 \left(\cos[\beta_{11}(\omega t + \pi)], \sin[\beta_{11}(\omega t + \pi)]\right). \tag{2.7}$$

This formula shows that the orbital center approximately traces out a circle of radius proportional to a_1 (the period-doubled amplitude), whose period $2\pi/(\beta_{11}\,\omega)$ is necessarily long relative to the orbital period T. In order for this argument to hold, the following conditions must be met.

Criterion 1: α must be close to, but not exactly equal to 2.

Criterion 2: A period-doubling bifurcation must happen after the wobbling state emerges.

This argument provides a new rationale for the onset of period-doubling coinciding with the onset of drifting, a feature highlighted in previous experiments [52] and simulations [83].

2.3 Simple harmonic potential

We next consider the pilot-wave dynamics of a droplet walking in a harmonic potential. In this scenario, the walker is subjected to a radial spring force, $\boldsymbol{\mathcal{F}} = -k\boldsymbol{x}_p$. This system was realized experimentally by Perrard *et al.* [86, 85] by encapsulating a small amount of ferromagnetic fluid in a walking droplet and exposing this compound droplet to a radially non-uniform vertical magnetic field. They demonstrated that, as the forcing amplitude is increased progressively, quantized circular orbits emerge, followed by more complex periodic and aperiodic trajectories. A key observation was the emergence of orbits that were quantized in both mean radius and angular momentum, a quantum-like feature also captured in their simulations. They also noted

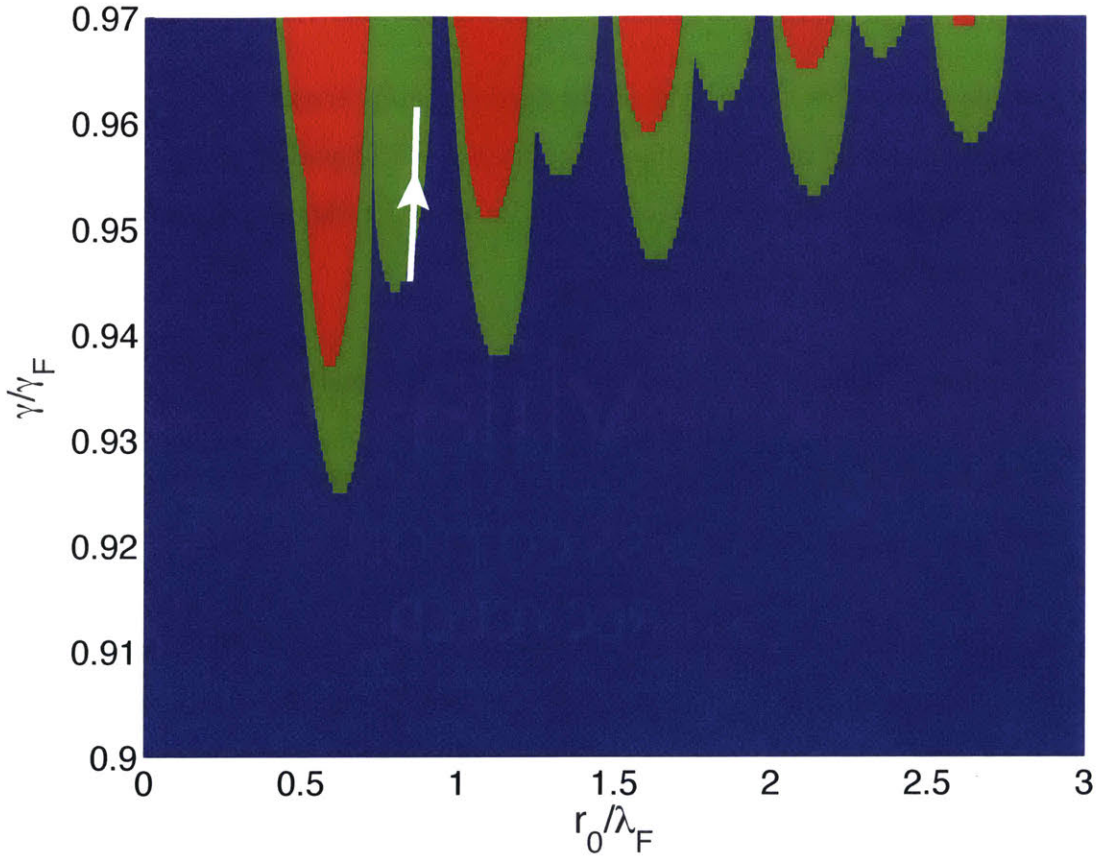

Figure 2-5: Linear stability diagram [79] of orbital solutions of radius r_0 arising in the presence of a linear spring force $\boldsymbol{\mathcal{F}} = -k\boldsymbol{x}_p$. γ/γ_F is the dimensionless driving acceleration and λ_F is the Faraday wavelength. The drop's radius is $R_D = 0.4$ mm, impact phase $\sin\Phi = 0.2$, viscosity $\nu = 20$ cS and forcing frequency 80 Hz. Blue regions indicate stable circular orbits. Green regions correspond to circular orbits that destabilize via an oscillatory instability. Red regions correspond to orbits that destabilize via a nonoscillatory instability. The white curve indicates the path through parameter space for the results shown in Section 2.3. The transition to chaos is generic in this system; specifically, it arises in passing from blue to green regions with increasing memory.

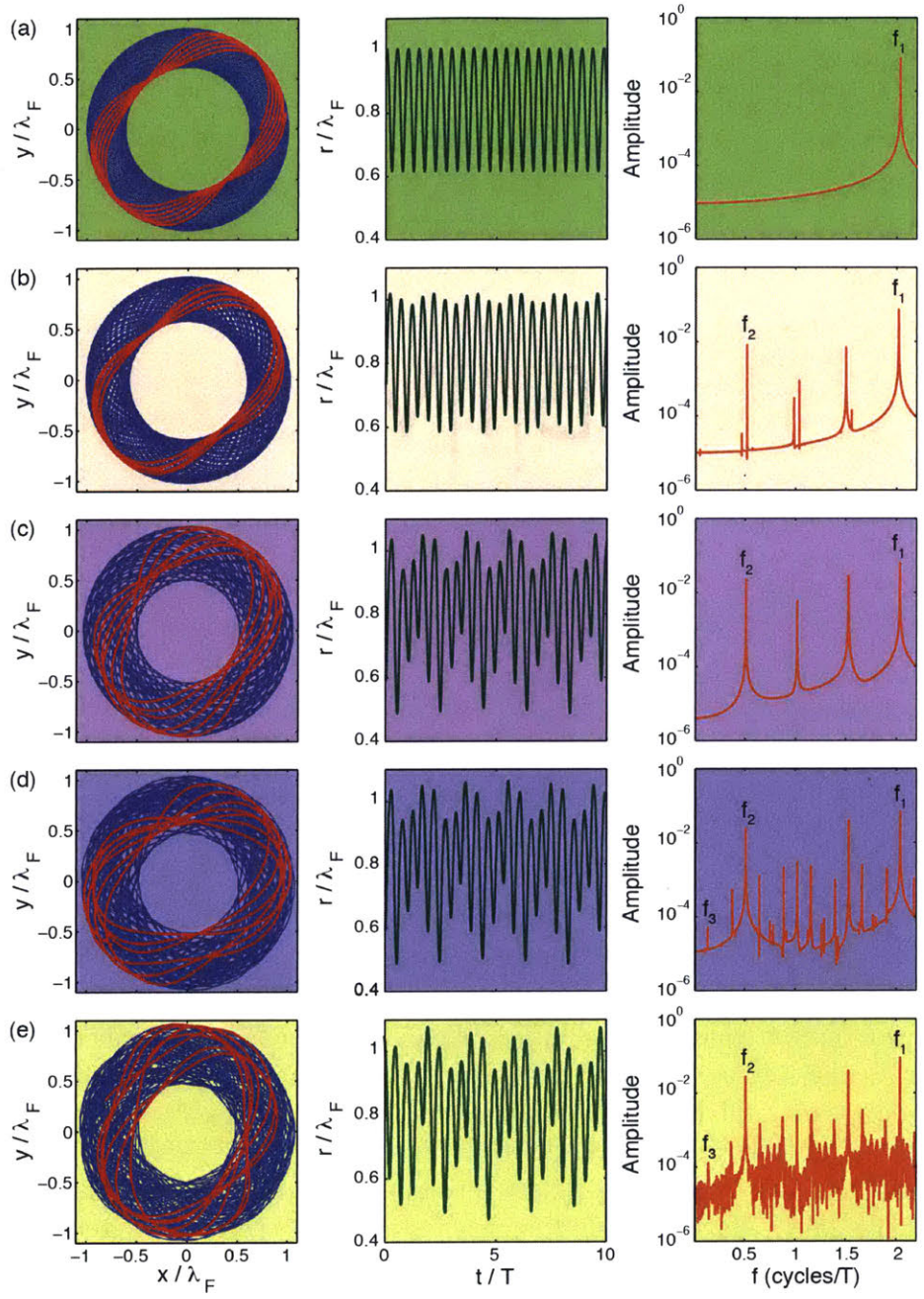

Figure 2-6: Numerical solutions to the trajectory equation (Eq. 2.2) with a spring force $\boldsymbol{\mathcal{F}} = -k\boldsymbol{x}_p$ and a fixed dimensional spring constant $k = 3.2$ μN/m which describes pilot-wave dynamics in a harmonic potential. The first column shows the simulated trajectories $\boldsymbol{x}_p(t)$ plotted over many orbital periods (blue) along with the last few orbital periods (red). The second column shows the orbital radius $r(t) = |\boldsymbol{x}_p(t)|$. The third column shows the frequency spectrum of $r(t)$. The rows correspond to (a) a wobbling orbit ($\gamma/\gamma_F = 0.9573$), (b) a quasiperiodic wobbling orbit ($\gamma/\gamma_F = 0.9583$), (c) a frequency-locked wobbling orbit ($\gamma/\gamma_F = 0.9600$), (d) a frequency-locked wobbling orbit with an additional incommensurate frequency ($\gamma/\gamma_F = 0.9610$), and (e) a chaotic trajectory ($\gamma/\gamma_F = 0.9613$).

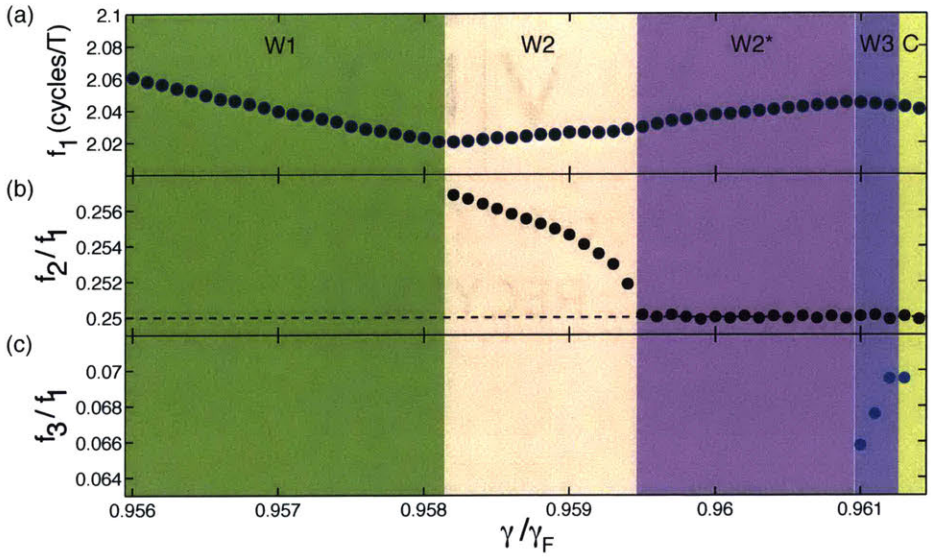

Figure 2-7: Diagram detailing the evolution with memory of the independent peak frequencies in the spectrum of $r(t)$ arising during the transition to chaos in a harmonic potential with dimensional spring constant $k = 3.2\ \mu$N/m. Panel (a) tracks the principal wobbling frequency f_1, which first appears when the circular orbit becomes unstable. As the forcing acceleration is increased further, a second independent frequency f_2 appears, which later becomes locked with f_1 at $f_2/f_1 = 1/4$, as shown in panel (b). At higher accelerations, a third independent frequency f_3 appears that precedes the transition to a broadband spectrum in the chaotic regime, as shown in panel (c). We label W1 the single-frequency state, W2 the two-frequency quasiperiodic state, W2* the two-frequency frequency-locked state, W3 the state with a third incommensurate frequency, and C the chaotic orbital state. The dimensionless forcing acceleration is changed in increments of $\Delta(\gamma/\gamma_F) = 10^{-3}$ for $\gamma/\gamma_F \in [0.945, 0.956]$ and $\Delta(\gamma/\gamma_F) = 10^{-4}$ for $\gamma/\gamma_F \in [0.9560, 0.9614]$.

that in certain parameter regimes, an intermittent switching between the quantized periodic states could be observed.

We here confine our attention to the stability of the quantized circular orbits. As in Section 2.2, we examine the transition from a stable circular orbit to a chaotic wobbling orbit as the forcing acceleration is increased. We proceed to demonstrate that the transition to chaos is qualitatively different. We characterize the orbits in terms of their local radius $r(t) = |\boldsymbol{x}_p(t)|$, the distance to the center of the fixed harmonic potential, as well as the associated frequency spectrum.

The dimensional spring constant is here fixed to be $k = 3.2\ \mu$N/m which results in circular orbital solutions of radius $r_0 \sim 0.8\lambda_F$ for our choice of system parameters. For $\gamma/\gamma_F < 0.948$ these circular orbits are stable, in accordance with the linear stability analysis [61] summarized in Fig. 2-5. For $\gamma/\gamma_F \geq 0.948$, the circular orbit destabilizes into a wobbling orbit (Fig. 2-6a) whose radius oscillates with a single well-defined frequency f_1 that is approximately twice the orbital frequency $\omega/2\pi$. When the forcing acceleration is increased to $\gamma/\gamma_F = 0.9482$, a second independent frequency f_2 appears in the wobbling spectrum as shown in Fig. 2-6(b). Note that the additional peaks apparent in the spectrum of $r(t)$ correspond to integer linear combinations of the two base frequencies f_1 and f_2. As the forcing acceleration is increased further, the ratio of these frequencies changes continuously until they lock onto a fixed integer ratio at $\gamma/\gamma_F = 0.9495$ (Fig. 2-6c). For the simulations at higher memory, f_2 remains locked with f_1 in a ratio $f_2/f_1 = 1/4$. When the forcing acceleration reaches $\gamma/\gamma_F = 0.9610$, an additional incommensurate frequency f_3 (along with its integer linear combinations with f_1 and f_2) appears as shown in Fig. 2-6(d). Shortly after the appearance of this new frequency, for $\gamma/\gamma_F \geq 0.9613$, the spectrum begins to show evidence of broadband noise and the trajectory becomes chaotic, as shown in Fig. 2-6(e). Similar transitions to chaos were observed in other tongues for paths crossing from blue to green regions with increasing memory. We note that evidence of this particular route to chaos has also been observed in experiments [84].

In summary, we observe a transition from a base state (circular orbit), to a single-frequency state (W1), to a two-frequency quasiperiodic state (W2), to a two-frequency

frequency-locked state (W2*). Thereafter, a state with an additional incommensurate frequency emerges (W3), followed by a chaotic orbital state (C). This evolution can be summarized by the emergence of independent peaks in the frequency spectrum of $r(t)$ as shown in Fig. 2-7. This transition from a stable circular orbit to a chaotic wobbling orbit is notably different from the classic period-doubling transition, but instead appears similar to the Ruelle-Takens-Newhouse route to chaos [93, 77]. In the Ruelle-Takens-Newhouse scenario, a finite sequence of bifurcations gives rise to additional frequencies in the spectrum and after three such bifurcations, it is *likely* (but not guaranteed) that a strange attractor appears in phase space [30].

2.4 2D Coulomb potential

Finally, we consider a walking droplet subjected to a two-dimensional radial Coulomb force $\boldsymbol{\mathcal{F}} = -Q\boldsymbol{x}_p/|\boldsymbol{x}_p|^2$. Such a force would correspond to a walking droplet with electric charge q attracted to an infinite line charge with charge density Λ placed at the origin normal to the fluid bath where $Q = q\Lambda/2\pi\epsilon_0$ (with electric constant $\epsilon_0 = 8.8 \times 10^{-12}$ F/m). In dimensionless form, $\boldsymbol{\mathcal{F}} = -\hat{Q}\boldsymbol{x}_p/|\boldsymbol{x}_p|^2$, where $\hat{Q} = Qk_F^2T_M/D$. Although this system is yet to be realized experimentally, we can investigate it numerically using the integro-differential equation (2.2), which has been validated against experiments for walkers in Coriolis [52] and central harmonic [86] forces.

Note that circular orbits $\boldsymbol{x}_p(t) = r_0(\cos\omega t, \sin\omega t)$, with radius r_0 and orbital frequency ω, are exact solutions of Eq. (2.3) with an external Coulomb force $\boldsymbol{\mathcal{F}}$. We assess linear stability of these solutions by a procedure analogous to that used by Oza *et al.* [79], and summarize our results in Fig. 2-8. Orbits with radii $0.3 < r_0/\lambda_F < 0.5$ are predicted to be stable provided $\gamma/\gamma_F < 0.915$. Thus, we initialize the simulation with $\gamma/\gamma_F = 0.91$ and a fixed charge parameter $Q = 0.35$ nJ that corresponds to a stable circular orbit of radius $r_0 = 0.385\lambda_F$. We evolve the system as described in Section 2.1 with an initial increment of $\Delta(\gamma/\gamma_F) = 10^{-3}$.

As indicated by the linear stability analysis (Fig. 2-8), the circular orbit becomes unstable to a wobbling orbit at $\gamma/\gamma_F \gtrsim 0.920$. An example of a wobbling orbit is

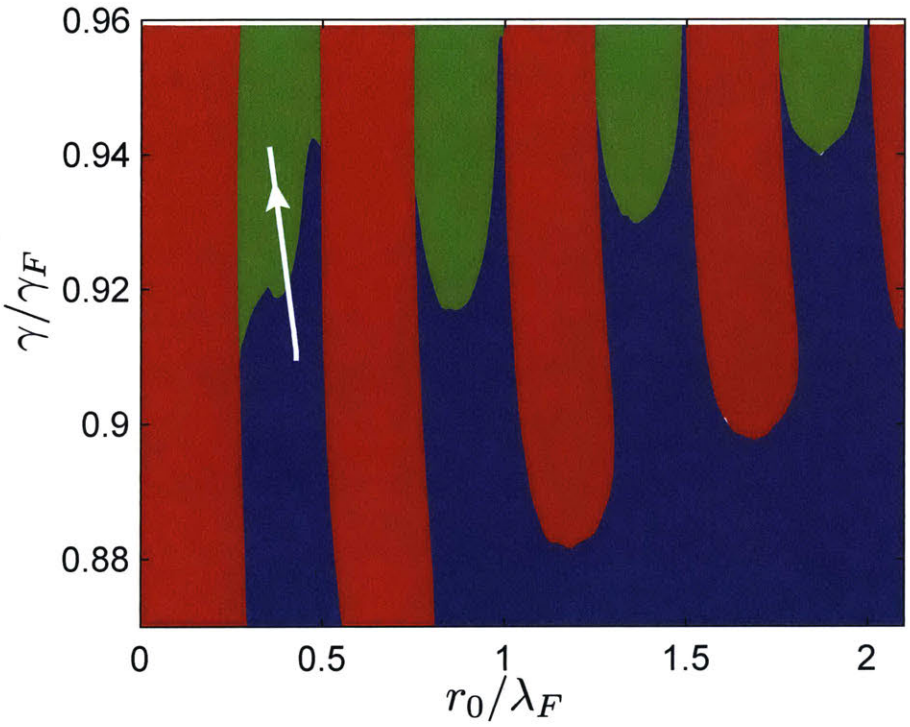

Figure 2-8: Linear stability diagram of orbital solutions of radius r_0 arising in the presence of a 2D Coulomb force $\boldsymbol{\mathcal{F}} = -Q\boldsymbol{x}_p/\left|\boldsymbol{x}_p\right|^2$. γ/γ_F is the dimensionless driving acceleration and λ_F is the Faraday wavelength. Blue regions indicate stable circular orbits. Green regions correspond to circular orbits that destabilize via an oscillatory instability. Red regions correspond to orbits that destabilize via a nonoscillatory instability. The transition to chaos is tracked along the white curve by finding an initial stable solution (r_0, ω, Q) to Eq. (2.3) and increasing the dimensionless forcing acceleration γ/γ_F progressively while keeping Q constant.

shown in the first panel of Fig. 2-9(a) for $\gamma/\gamma_F = 0.9375$. We use the fact that the system has an imposed center to characterize the trajectory by its radius $r(t) = |\boldsymbol{x}_p(t)|$, plotted in the second panel of Fig. 2-9(a), which exhibits a periodic oscillation between two values. The frequency spectrum of $r(t)$, shown in the third panel of Fig. 2-9(a) indicates that the wobbling frequency is $\omega_{\text{wobble}} \sim 0.65\omega$. Since, $\omega_{\text{wobble}}/\omega$ is not close to 2 (Criterion 1), this system does not exhibit drifting orbits.

As the memory is further increased, the frequency spectra shown in the last column of Fig. 2-9 exhibit evidence of successive period-doubling bifurcations: half-frequencies $\omega_{\text{wobble}}/2$ emerge at $\gamma/\gamma_F \sim 0.9394$, quarter-frequencies at $\gamma/\gamma_F \sim 0.94141$, and eventually a broadband frequency spectrum at $\gamma/\gamma_F \sim 0.941791$, evidence of chaotic dynamics. We also see a period-20 orbit when $\gamma/\gamma_F \sim 0.941815$ (Fig. 2-9(e)), an example of a periodic window within the chaotic regime. The period-doubling cascade is more clearly evident in Fig. 2-10, where we plot the local maxima r_m of the radius $r(t)$ as a function of the forcing acceleration γ/γ_F.

Unlike those arising in the presence of a Coriolis force or a simple harmonic potential, the transition to chaos was specific to the leftmost green tongue (Fig. 2-8), where it was observed for different initial radii $0.3 < r_0/\lambda_F < 0.5$ and corresponding Q. Chaotic orbits have not been observed in other isolated regions of oscillatory instability, where unstable orbits tend to spiral into the center or away to infinity instead of undergoing a period-doubling cascade.

2.5 Discussion

We have characterized the transition from stable circular orbits to chaos in three pilot-wave systems as the forcing acceleration is increased progressively. Walking droplets subject to Coriolis (Section 2.2) and Coulomb (Section 2.4) forces follow a period-doubling route to chaos, whereby circular orbits are destabilized into wobbling trajectories of increasing complexity. The main difference between these two scenarios, arising from the fact that the rotating system does not have a fixed center of force, is the existence of drifting orbits in the rotating frame. These orbits emerge when

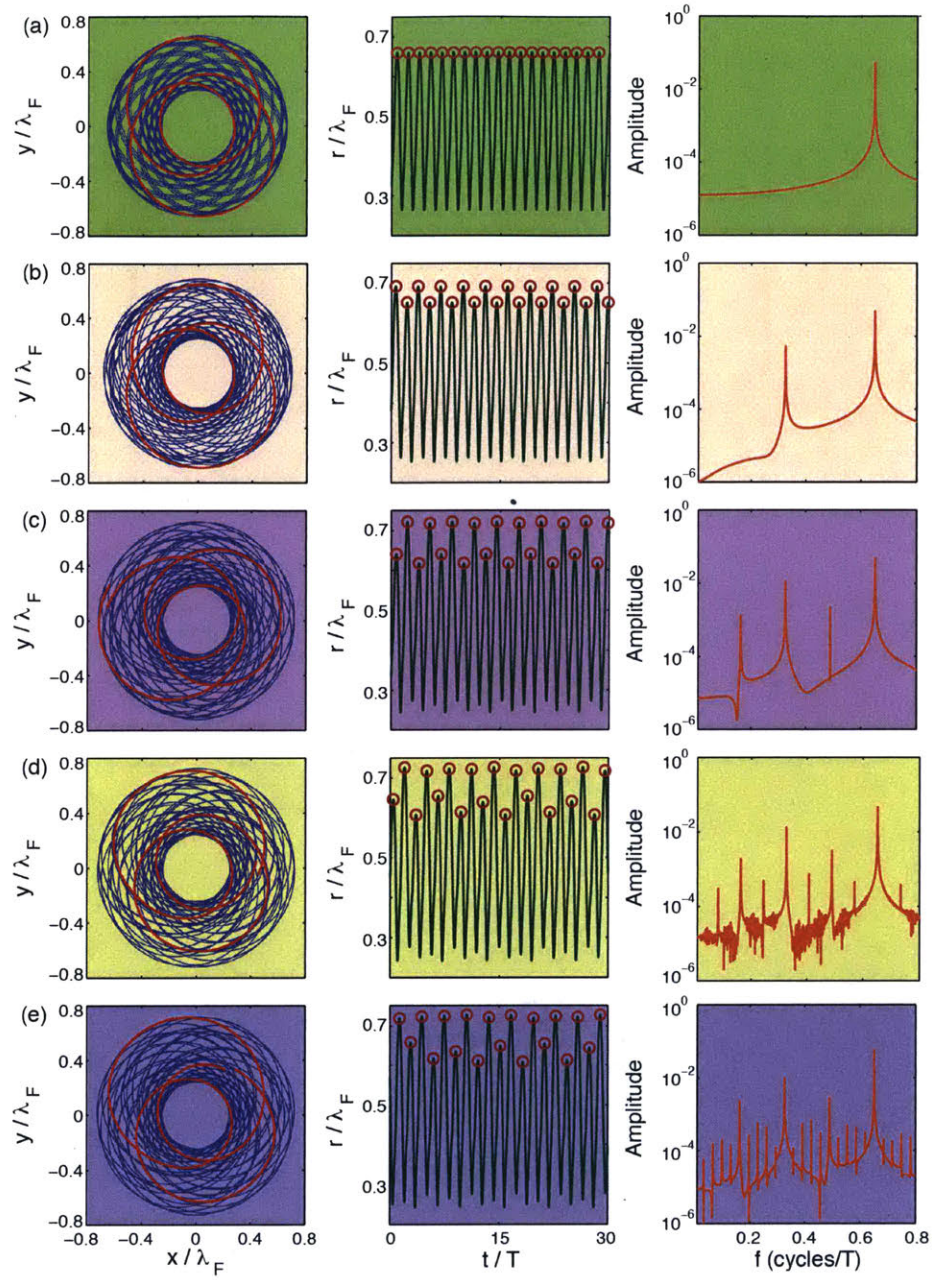

Figure 2-9: Numerical simulations of Eq. (2.2) with $\boldsymbol{\mathcal{F}} = -Q\boldsymbol{x}_p/|\boldsymbol{x}_p|^2$, which describes the pilot-wave dynamics of a walking droplet subject to a two-dimensional Coulomb force. The first column shows the trajectory $\boldsymbol{x}_p(t) = (x_p(t), y_p(t))$ with the long term trajectory shown in blue, and the last few orbits colored red. The radius of the orbit $r(t) = |\boldsymbol{x}_p(t)|$ is plotted in the middle column with local maxima r_m indicated by red circles. The third column shows the frequency spectrum of $r(t)$. The memory parameter is progressively increased from panels (a) through (e) with rows corresponding to: (a) a wobbling orbit ($\gamma/\gamma_F = 0.9375$), (b) a period-2 wobbling orbit ($\gamma/\gamma_F = 0.9394$), (c) a period-4 wobbling orbit ($\gamma/\gamma_F = 0.94141$), (d) a chaotic trajectory ($\gamma/\gamma_F = 0.941791$), and (e) a period-20 orbit ($\gamma/\gamma_F = 0.941815$) in a periodic window within the chaotic regime.

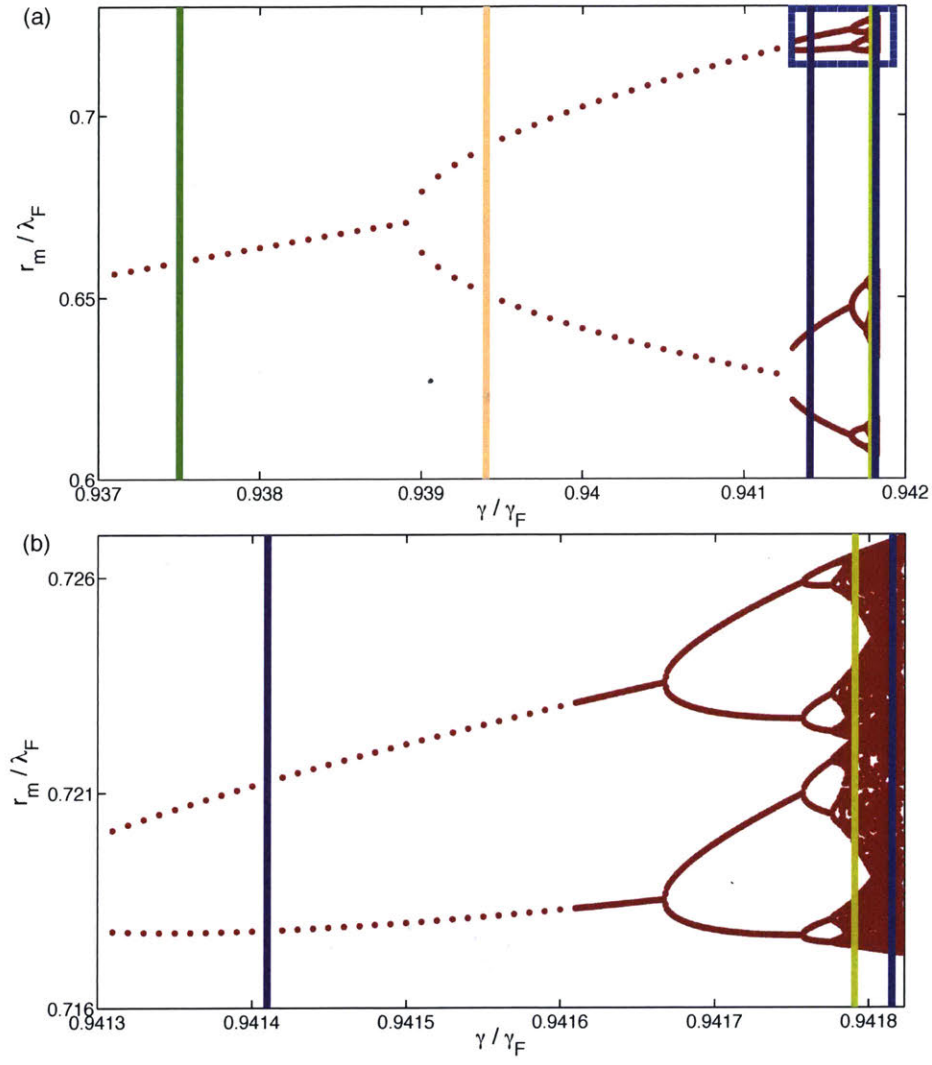

Figure 2-10: Bifurcation diagrams showing the route to chaos for a walking droplet subject to a two-dimensional Coulomb force with charge parameter $Q = 0.35$ nJ. We track the local maxima r_m of the orbital radius $r(t) = |\boldsymbol{x}_p|$ as a function of the non-dimensional forcing acceleration γ/γ_F. Panel (b) gives a magnified view of the upper right corner (delineated by the blue box) of panel (a), showing the details of the period-doubling cascade immediately preceding the transition to chaos. Color-coded vertical lines correspond to the trajectories depicted in Fig. 2-9. The dimensionless forcing acceleration is changed in increments of $\Delta(\gamma/\gamma_F) = 10^{-3}$ for $\gamma/\gamma_F \in [0.910, 0.936]$, $\Delta(\gamma/\gamma_F) = 10^{-4}$ for $\gamma/\gamma_F \in [0.9361, 0.9413]$, $\Delta(\gamma/\gamma_F) = 10^{-5}$ for $\gamma/\gamma_F \in [0.94131, 0.94161]$ and $\Delta(\gamma/\gamma_F) = 10^{-6}$ for $\gamma/\gamma_F \in [0.941611, 0.941900]$.

a wobbling orbit of frequency approximately twice the orbital frequency undergoes a period-doubling bifurcation. The rotating system is thus seen to support stable non-linear states characterized by a drifting self-orbiting motion, which are related to the hydrodynamic spin states discussed in Oza *et al.* [79], Bush [14], and Labousse [60].

The case of a walking droplet in a simple harmonic potential (Section 2.3) exhibits an entirely different transition to chaos. The circular orbits destabilize into wobbling orbits, but successive bifurcations lead to the appearance of new independent frequencies in the power spectrum of the orbital radius. These independent frequencies eventually lock; subsequently, just before the chaotic regime, we see the emergence of an additional incommensurate frequency. The observed transition is similar to the Ruelle-Takens-Newhouse route to chaos, as has been observed previously in other fluid systems, including Rayleigh-Bernard convection [45] and Taylor-Couette flow [46], as well as in simulations of converging-diverging channel flows [50].

As noted in the experimental realizations of walking droplets subject to Coriolis [52] and central [86] forces, increasing the forcing acceleration has the effect of destabilizing circular orbits. The evolution from stable circular orbits to chaotic trajectories occurs over a small range $\Delta(\gamma/\gamma_F) \sim 10^{-4}$; thus, resolving this transition requires extremely precise experiments. In our numerical investigation, we were able to capture the details of each bifurcation and explore the transition to chaos by finely adjusting our memory parameter. For Coulomb and Coriolis forces, we note that the forcing acceleration was increased by increments as small as $\Delta(\gamma/\gamma_F) = 10^{-6}$, which allowed us to capture period-16 and period-32 orbits within exceedingly narrow parameter windows. Such an exploration is not possible with current experimental capabilities [53].

Relating the periodic and quasiperiodic trajectories observed at low memory to the multimodal statistical behavior of chaotic trajectories in the high-memory limit is the subject of ongoing research. Establishing a quantitative link between the unstable periodic orbits and the emergent statistical behavior in the high-memory limit is an objective reminiscent of that of Gutzwiller, who related classical periodic orbits with solutions of the time-independent Schrödinger equation [49]. It is hoped that this

study, the first theoretical investigation of routes to chaos in a pilot-wave system, will attract the attention of the dynamical systems community to a remarkably rich new class of problems.

Chapter 3

The Faraday-Talbot effect

3.1 Introduction

Hydrodynamics has long served as a rich source of physical analogy. Newton described corpuscles of light generating waves through the ether like stones dropped on a pond [78], while Thomas Young argued the wave nature of light by analogy with ripple tank experiments [117]. On an astrophysical scale, hydrodynamic analogs of black holes [109] and white holes [57] have been explored. In the quantum realm, both the Aharanov-Bohm [4] and Casimir effects [23] have been examined using fluid analog systems. The quantum-like features of droplets walking on a vibrating fluid bath [17, 88] are a subject of growing interest [14, 13].

As first reported by Faraday [37] in 1831, the free surface of a fluid bath vertically vibrated with amplitude A, frequency f, and acceleration $\Gamma(t) = \gamma\cos(2\pi ft)$ may become unstable to standing surface waves with frequency $f/2$. For a vibrational acceleration $\gamma = A(2\pi f)^2$ below the Faraday threshold γ_F, the free surface is stable. For $\gamma > \gamma_F$ the surface becomes unstable to subharmonic Faraday waves with wavelength $\lambda_F = 2\pi/k_F$ prescribed by the standard water-wave dispersion relation

Parts of this chapter were published in "Hydrodynamic analog of particle trapping with the Talbot effect," N. Sungar, L. D. Tambasco, G. Pucci, P. J. Sáenz, and J. W. M. Bush, Physical Review Fluids **2**, 103602 [100]. Section 3.3 was submitted in: "Faraday-Talbot effect: alternating phase and circular arrays," N. Sungar, J. P. Sharpe, J. J. Pilgram, J. Bernard and L. D. Tambasco, (Submitted, 2018) [99].

$$\omega^2(k) = \left(gk + \frac{\sigma}{\rho}k^3\right)\tanh(hk), \tag{3.1}$$

where k is the wavenumber, g the gravitational acceleration, σ the surface tension, ρ the fluid density and h the fluid depth. Faraday waves have been extensively investigated both experimentally and theoretically [26, 3, 69]. Just below the Faraday threshold $\gamma < \gamma_F$, perturbations of the surface generate Faraday waves that decay over a characteristic memory time $T_M = \lambda_F^2/\left[8\pi^2\nu\left(1-\gamma/\gamma_F\right)\right]$, where ν is the fluid's kinematic viscosity. The Faraday system has recently been used to study hydrodynamic quantum analogs, as may arise when millimetric droplets levitating on the vibrating bath self-propel through a resonant interaction with their own wavefield [17, 88, 14].

The optical Talbot effect occurs in the near field when a monochromatic wave is modulated by a spatially periodic structure [116]. The effect was discovered in 1836 by Henry Fox Talbot in his examination of the optical pattern behind an illuminated diffraction grating [101]. The supporting theory was developed in 1881 by Lord Rayleigh, who showed that the effect results from the interference of monochromatic, coherent waves emitted from the diffraction grating [92]. In his analysis, Rayleigh expressed the optical field resulting from the interference of waves from individual slits in terms of a sum over monochromatic plane waves with wavelength λ and transverse wave-vector components $2\pi n/d$, where d is the slit spacing and $n \in \mathbb{N}_0$. He showed that at integer multiples of a distance z_T perpendicular to the grating, the intensity distribution at the grating is reproduced. This distance, called the Talbot length, is given by

$$z_T(\lambda) = \frac{\lambda}{2\left(1-\sqrt{1-\left(\frac{\lambda}{d}\right)^2}\right)}. \tag{3.2}$$

When $\lambda \ll d$, Eq. 3.2 reduces to a better-known formula for the Talbot length $z_T = d^2/\lambda$. The analysis shows that at even integer multiples of the Talbot length, self-images are spatially in phase with the grating. At odd integer multiples of the Talbot length, self-images are shifted by half the slit spacing $(d/2)$, and so referred

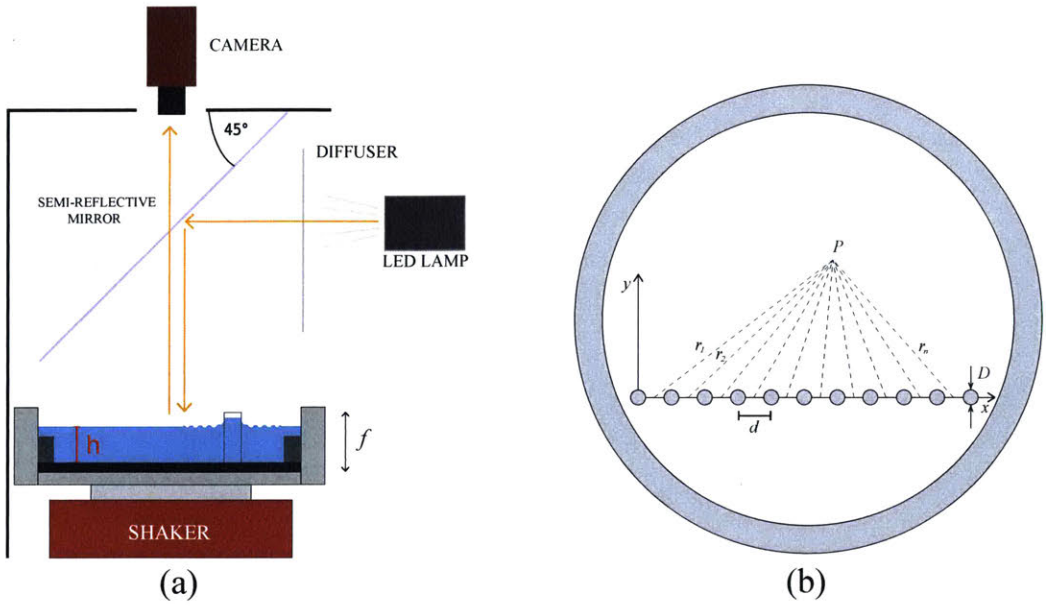

Figure 3-1: (a) Experimental arrangement [53]. The fluid bath is shaken using an electromagnetic shaker and imaged using a CCD camera through a 45° semi-reflective mirror with diffuse illumination [26]. (b) Top view of the fluid bath shows the row of N protruding pillars of diameter D and center-to-center separation d.

to as shifted self-images [15].

The Talbot effect has since been extensively studied and applied in optics [113, 5]. This phenomenon has also been used in a variety of applications including optical trapping of atoms [76] and particles [98], atom wave interference [16], Bose-Einstein condensates [24], plasmonics [120], and X-ray imaging [112]. We here present a hydrodynamic analog of the Talbot effect in the Faraday system, and demonstrate its ability to trap bouncing and walking droplets.

3.2 The hydrodynamic Talbot effect

3.2.1 Experiment

The setup consists of a circular bath 15.8 cm in diameter that is vertically shaken and imaged from above using a diffuse light source. A schematic of the experiment is shown in Fig. 3-1. Silicone oil of viscosity $\nu = 20.9$ cSt, density $\rho = 950$ kg/m^3 and surface tension $\sigma = 20.6$ mN/m fills the circular bath to a depth of $h = 6.10 \pm 0.05$

mm. The bath is surrounded by a shallow region of depth 1.1 mm and width 12.7 mm that serves to damp the waves at the bath boundaries. A linear, periodic array of N pillars, each with diameter $D = 3.1 \pm 0.1$ mm and separated by a center-to-center distance d, protrudes from the bath to a height of 2.1 mm above the fluid surface.

The recording camera directly above the bath images the surface at a frame rate slightly higher than $f/4$ in order to reveal fast oscillations in the observed patterns. The setup is illuminated from the side by an LED lamp, and the light is redirected by a 45° semi-reflective mirror, as shown in Fig. 3-1. The incident light is normal to the bath, then reflects back to the camera. With this imaging technique, flat areas of the interface appear as bright regions, sloped areas as dark regions.

We report here experimental results with two different array separations of $d = 9.5$ mm and $d = 12.5$ mm with a total number of pillars $N = 14$ and $N = 11$, respectively. Arrays with larger d necessarily had a smaller number of pillars and so produced images only in the central region of the near field. Forcing frequencies in the range of $40 - 90$ Hz were explored for each array. At every frequency investigated, the Faraday threshold γ_F was determined by decreasing γ, initially above γ_F, by decrements of $0.01g$ until Faraday waves far from the boundaries died out within 1 minute. The Faraday threshold is then set to be $0.005g$ above this acceleration.

We note that meniscus waves of the form seen in Fig. 3-2(a) are evident around the pillars even for $\gamma < \gamma_F$. The static menisci attached to the pillars have a characteristic height corresponding to the capillary length $\sqrt{\sigma/\rho g} \approx 1.5$ mm. When the bath is shaken, the variation in g causes the menisci to oscillate, emitting waves at the driving frequency f with a wavelength $\lambda_M = 2\pi/k_M$ (of order 3 mm for the frequencies considered) prescribed by Eq. 3.1 that is notably different from λ_F. We note that the attenuation length of the harmonic meniscus waves can be shown to scale as $c(k_M)/(2\nu k_M^2)$, where $c(k) = \mathrm{d}\omega/\mathrm{d}k$ is the group velocity [114]. For the range of frequencies considered, this attenuation length is of order 2 mm, consistent with Fig. 3-2(a), where meniscus waves are seen to extend no further than 1 cm beyond the pillars. While the meniscus waves contribute negligibly to the far field, they do modify the waves near the pillars, perturbing and coupling to the subharmonic

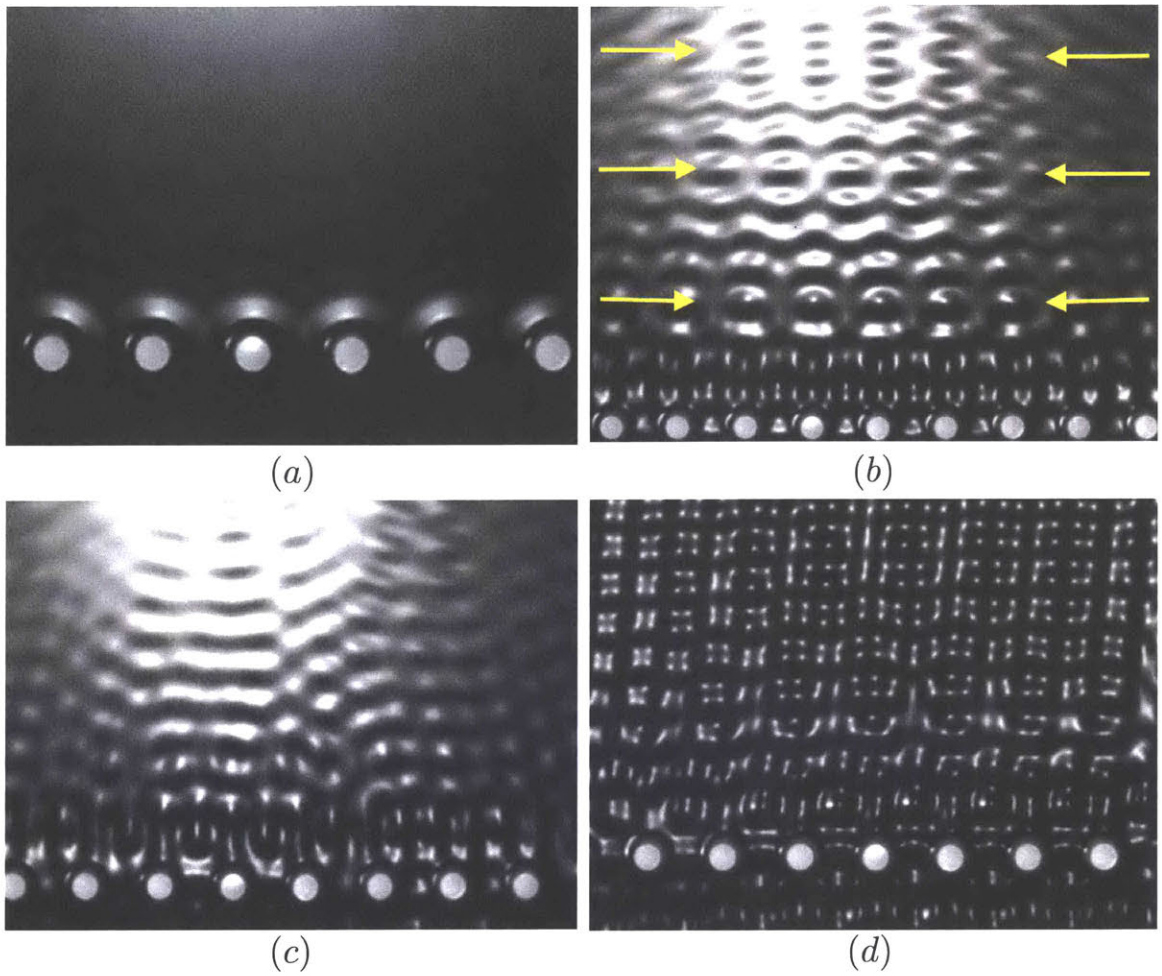

Figure 3-2: The surface of the shaken fluid. Pillars with diameter $D = 3.1$ mm are spaced $d = 9.5$ mm apart from center to center. (a) $f = 80$ Hz, $\gamma = 0.99\gamma_F$. Meniscus waves are evident around the pillars. (b) $f = 80$ Hz, $\gamma = 1.007\gamma_F$. Rows of images in front of the pillars are marked with arrows. (c) $f = 70$ Hz, $\gamma = 1.007\gamma_F$. The pattern has lost its periodicity. (d) $f = 80$ Hz, $\gamma = 1.012\gamma_F$. The self-imaging pattern is lost, replaced by a checkerboard of Faraday waves.

Faraday waves that emerge for $\gamma > \gamma_F$.

In a narrow range of driving frequencies that depends on the pillar spacing, standing wave patterns that replicated the periodicity of the pillar array were apparent (see Fig. 3-2(b)). Outside this frequency range, patterns did not form regular periodic structures and were distorted with defects as shown in Fig. 3-2(c). We note that even at the requisite driving frequency, sharp self-images were observed only at accelerations within $0.2 - 1\%$ of γ_F. At higher γ, the self-image was destroyed and a checkerboard of Faraday waves, such as those shown in Fig. 3-2(d), dominated the fluid surface. High speed videos of the fluid motion reveal that the oscillation frequency of the pattern of all the pillar images is the resonant subharmonic, $f/2$, indicating that the patterns result from interfering Faraday waves.

The self-imaging arises over a narrow frequency range in which the center-to-center pillar spacing corresponds to approximately twice the Faraday wavelength $d \approx 2\lambda_F$. For the array with $d = 9.5$ mm, the self-imaging is observed for $f = 78 - 82$ Hz, corresponding to a Faraday wavelength range of $\lambda_F \approx 4.7$ mm and meniscus wavelength $\lambda_M \approx 2.8$ mm. Similarly, for the array with $d = 12.5$ mm, self-imaging happens at $57 - 61$ Hz, corresponding to $\lambda_F \approx 6.0$ mm and $\lambda_M \approx 3.6$mm. In both cases, at the frequencies where self-imaging arises we observe that curved ridges form between the pillars, and slosh laterally, normal to the array direction, in phase with each other at $f/2$. Two video frames, taken half a Faraday period $T_F/2 = 1/f$ apart, are shown in Fig. 3-3. The patterns on opposite sides of the pillar arrays are temporally out of phase, following the phase of the sloshing inter-pillar ridges.

We attribute these sloshing inter-pillar ridges to the interaction of Faraday and meniscus waves in the vicinity of the pillars. For an individual pillar at the onset of instability, $\gamma \geq \gamma_F$, waves are generated along the curved wall, producing wavefronts projecting perpendicular to the pillars [26]. The wavefronts from neighboring pillars evidently merge to form the sloshing ridges. These ridges persist even above the regime where self-imaging is observed (see Fig. 3-2(d)). We infer that when a periodic row of pillars is present, laterally sloshing ridges between the pillars act as sources of Faraday waves emitted from between the pillars. In the context of our subsequent

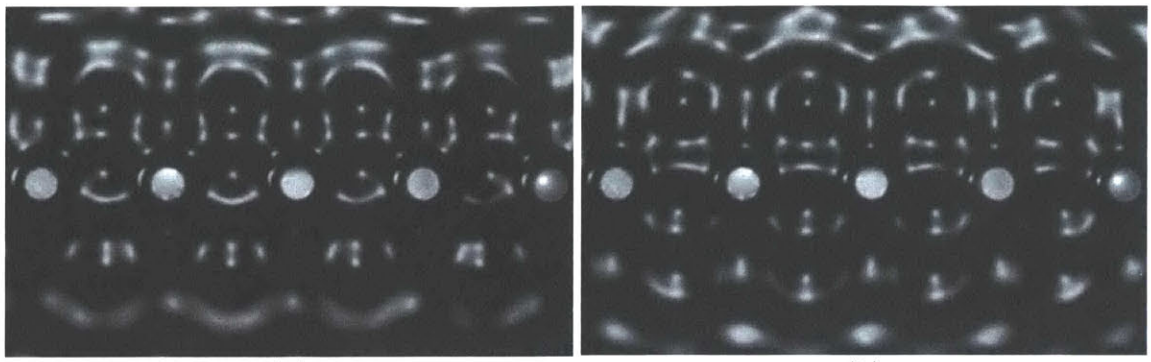

(a) (b)

Figure 3-3: Video frames showing the wavefield around the pillars, captured $T_F/2$ apart. The waves on either side of the pillars are temporally out of phase and the inter-pillar ridge sloshes back and forth in synchrony with the wave patterns.

theoretical developments it is important to note that it is not the pillars themselves that act as sources of Faraday waves, but rather the sloshing ridges between them.

3.2.2 Modeling

We model this hydrodynamic Talbot effect in terms of a periodic array of point sources emitting scalar waves. Guided by our observations, we treat the sources as emitters of subharmonic Faraday waves located between the pillars. We define the x-axis as lying along the pillars and the y-axis transverse to the pillars (see Fig. 3-1(b)). The elementary solution to the two-dimensional wave equation is $J_0(kr)e^{-i\omega t}$ where $J_0(kr)$ is the Bessel function of the first kind. When $kr \gg 1$, the Bessel function can be approximated as $J_0(x) \sim \cos(x - \pi/4)/\sqrt{\pi x/2}$. In adding waves from coherent sources, we can suppress the phase $\pi/4$, and so write the displacement of fluid at a position $P(x, y)$ (Fig. 3-1(b)) as the following superposition:

$$u(x, y, t) = A_F \sum_{n=1}^{N-1} \frac{\cos\left(k_F r_n - \omega_F t\right)}{\sqrt{k_F r_n}} \tag{3.3}$$

where A_F is the wave amplitude, $r_n = \sqrt{y^2 + \left(x - (n - 1/2)\, d\right)^2}$, $\omega_F = \pi f$, and k_F is the wave number for Faraday waves, prescribed by the standard water-wave dispersion relation, Eq. 3.1. Using Eq. 3.3, we compute the displacement $u(x, y, t)$ at each

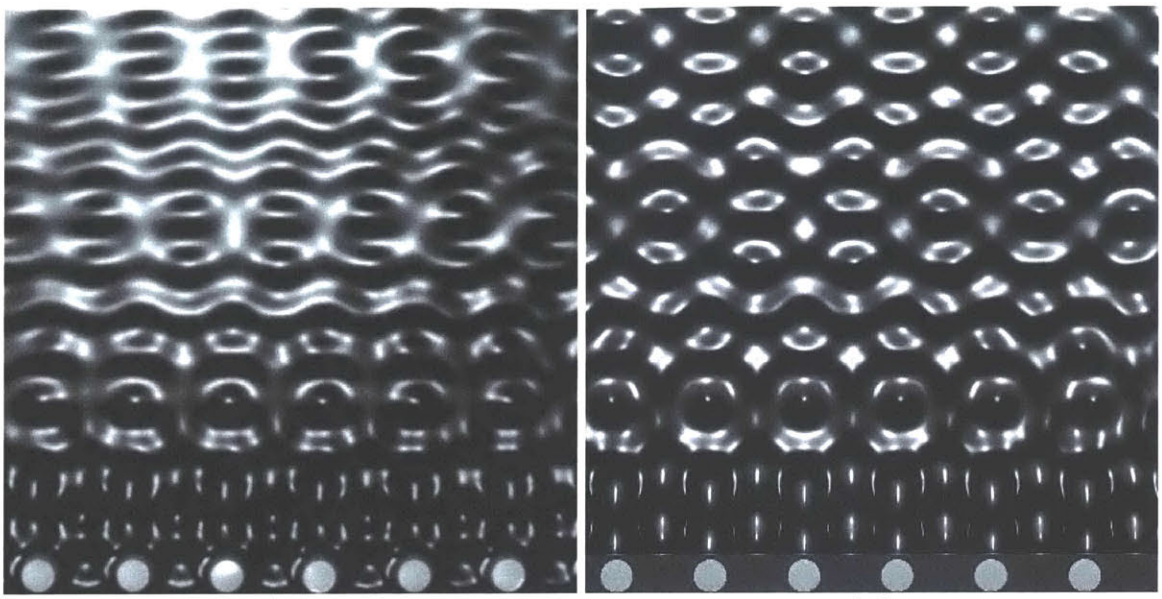

Figure 3-4: (a) Observed and (b) computed fluid surface height viewed from directly above, under oblique illumination. Circles at the bottom indicate the location of the pillars. Pillar spacing $d = 9.5$ mm, number of pillars $N = 14$, driving frequency $f = 80$ Hz, Faraday wavelength $\lambda_F = 4.75$ mm and forcing acceleration $\gamma = 1.007\gamma_F$.

point, nondimensionalized by the wave amplitude A_F. In order to compare the simulation results with experimental videos, we use Surface Plot in MATLAB to visualize the surface elevation. The reflectance properties of the surface are chosen such that the resulting greyscale in our simulations are consistent with that captured in our experiments. Fig. 3-4 shows a side-by-side comparison of the simulated and experimentally observed fluid surface, revealing that the essential features of the observed patterns are adequately captured by Eq. 3.3.

In our system, the self-images are generated predominantly by the Faraday waves emitted between the pillars. For comparison between our experiments and classical optics theory, which is for a monochromatic source of wavelength λ, we use the Faraday wavelength in Eq. 3.2 to evaluate the Faraday-Talbot length,

$$z_F = z_T(\lambda_F) = \frac{\lambda_F}{2\left(1 - \sqrt{1 - \left(\frac{\lambda_F}{d}\right)^2}\right)}. \tag{3.4}$$

Since the sources of Faraday waves are the subharmonic sloshing ridges between the pillars, self-images that are aligned with the pillars occur at odd integer multiples of z_F while those aligned with the gaps are at even integer multiples of z_F. Fig. 3-5 shows the measured distances of the self-images and shifted self-images in the video frames. Self-images further from the pillars are not as sharp, resulting in larger measurement errors.

For both arrays, the measured image locations are in agreement with the calculated Faraday-Talbot length z_F. Fig. 3-6 summarizes the results in a plot of experimental image position versus predicted image position. Note that the image positions are integer multiples of z_F.

3.3 Circular arrays

The Faraday-Talbot patterns formed by linear arrays preserves the transverse periodicity of the generating array, producing peaks that are separated by the inter-pillar distance d in the self-images. Curved arrays shift the locations of the self-images and magnify (or demagnify) the transverse periodicities p_n, the peak-to-peak separation in the n^{th} self image. In recent optical experiments with cylindrical gratings [107, 119], the modified Talbot length z_{TC} and the periodicity p_n of the n^{th} self-image was found to be

$$z_{\text{TC}} = \frac{nRz_T}{R - nz_T} \quad \text{and} \quad p_n = \frac{R}{R - nz_T}d, \tag{3.5}$$

where z_T is the Talbot length for a linear grating and d is the spacing of the grating. The radius of curvature R is positive if the images form on the convex side or negative if they form on the concave side. We here examine the images that form on the concave side of the array of pillars.

When a circular array consisting of 34 pillars, with separation $d = 9.5$ mm is driven at $f = 80$ Hz (corresponding to $\lambda_F = 4.75$ mm, $d = 2\lambda_F$), the ridges between the pillars oscillate coherently at $f/2$ giving rise to the Faraday-Talbot pattern shown in Fig. 3-7(a). The pattern is transient and decays within a few minutes, but it agrees

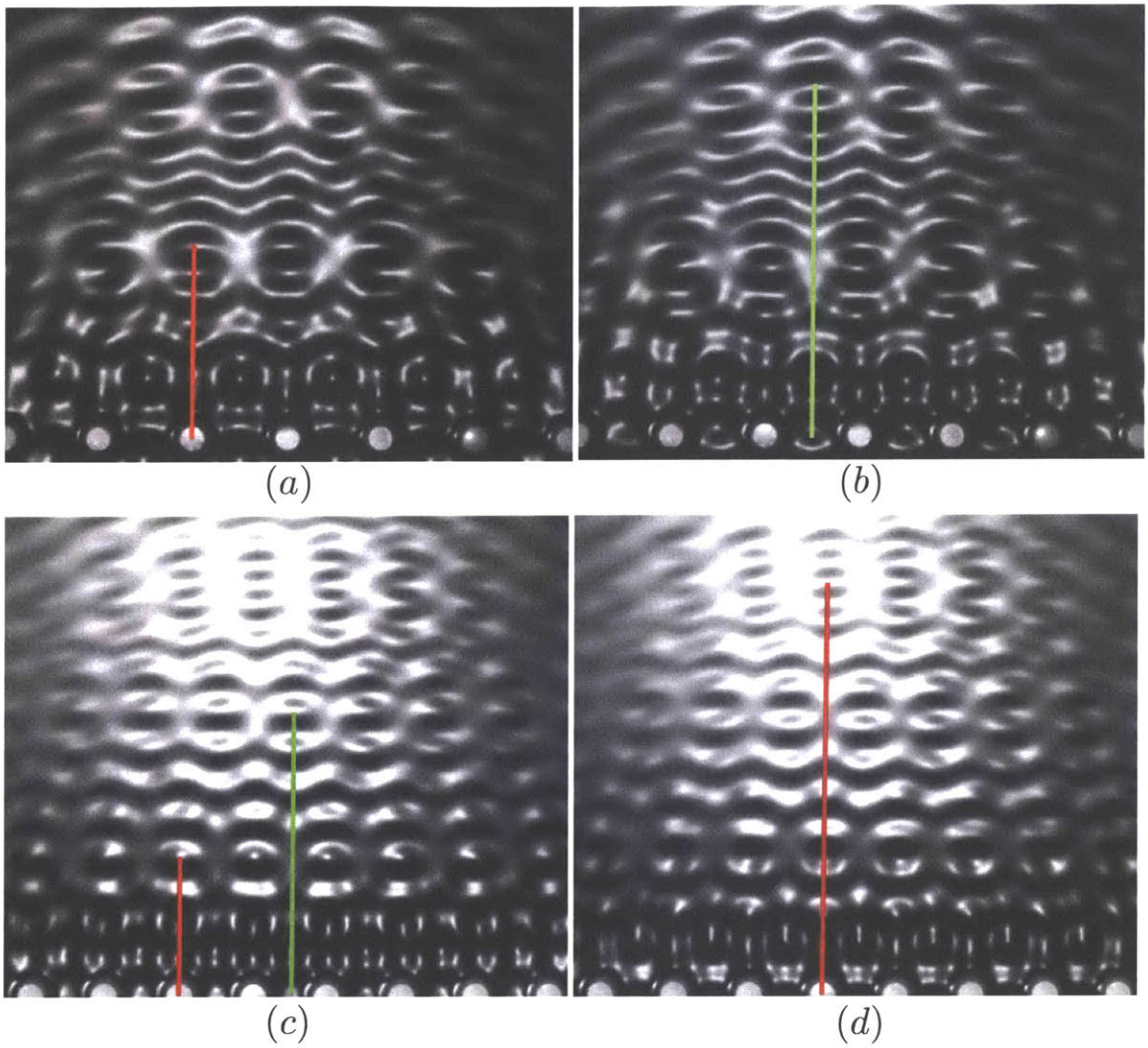

Figure 3-5: Self-image locations are evident on video frames half a Faraday period apart. Green lines indicate distances to the in-phase self-images of Faraday wave sources and red lines to the shifted self-images of Faraday wave sources. (a)-(b) Array spacing $d = 12.5$ mm, $f = 58$ Hz. Frames (a) and (b) are 1/58 s apart. (c)-(d) Array spacing $d = 9.5$ mm, $f = 80$ Hz. Frames (c) and (d) are 1/80 s apart.

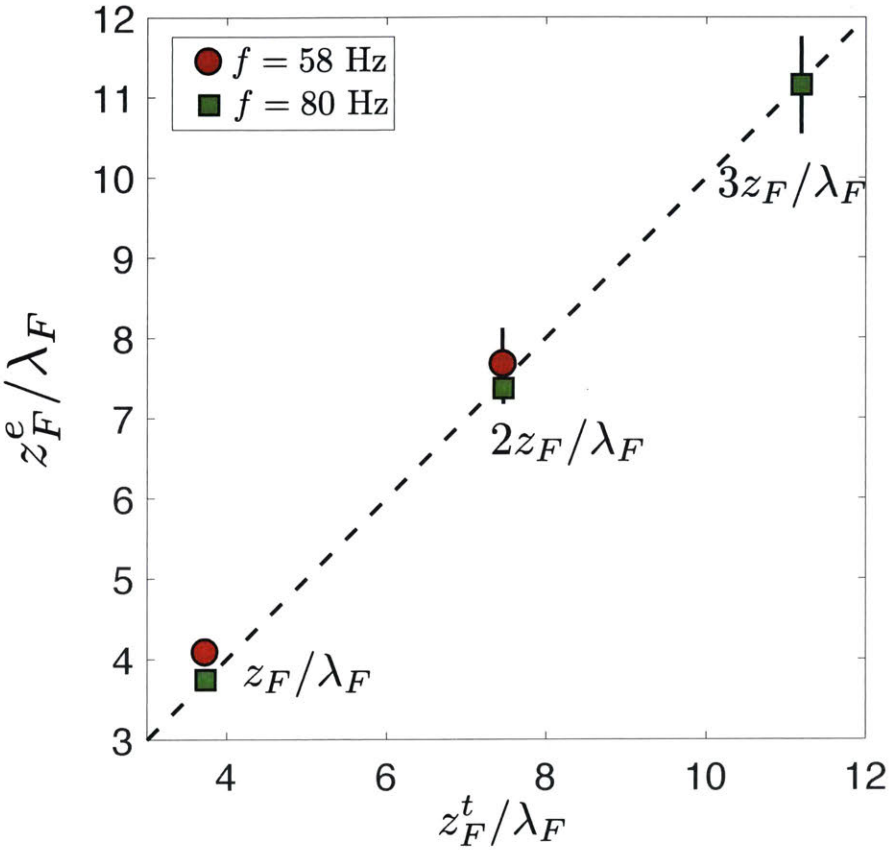

Figure 3-6: Plot of the experimentally observed self-image positions (z_F^e) versus predicted self-image positions (z_F^t) for two different forcing frequencies. Lengths are nondimensionalized by the Faraday wavelength λ_F. The predicted self-image positions are at integer multiples of the Faraday-Talbot length z_F, as defined in Eq. 3.4. Circles: Driving frequency $f = 58$ Hz, $\lambda_F = 6.13$ mm, pillar spacing $d = 12.5$ mm, $z_F = 23.9$ mm. Squares: $f = 80$ Hz, $\lambda_F = 4.75$ mm, $d = 9.5$ mm, $z_F = 17.7$ mm.

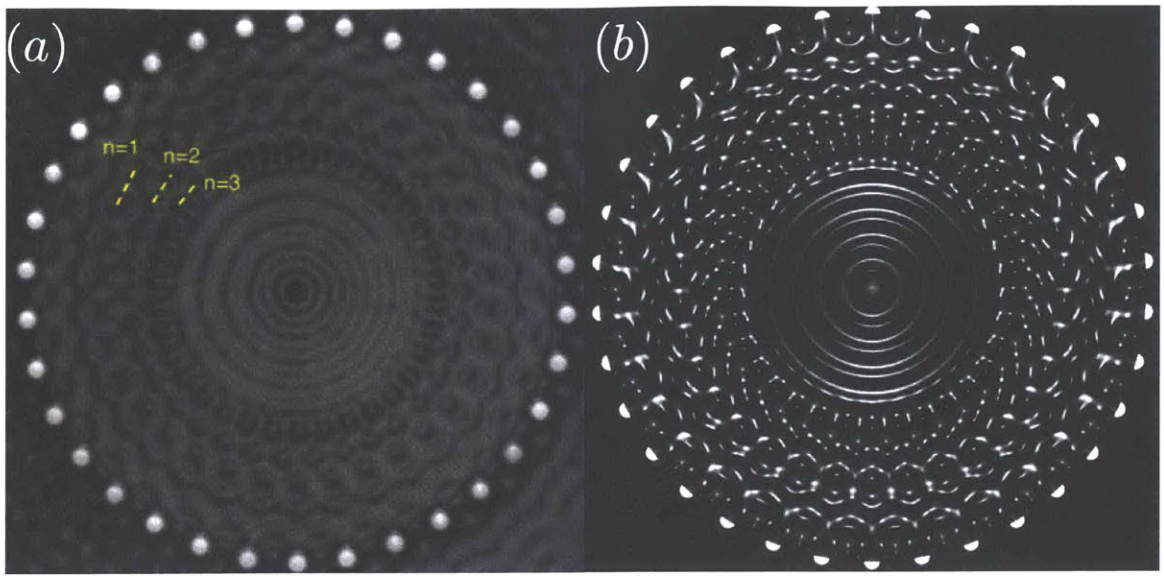

Figure 3-7: (a) Top view of the Faraday Talbot pattern for a circular array of pillars with coherently sloshing ridges. $f = 80$ Hz, $d = 9.5$ mm, $\lambda_F = 4.75$ mm, $R = 51.5$ mm. The dashed lines indicate the periodicities measured for the first three self-images. We note that this is a transient pattern; after a few minutes the pattern starts developing defects and destabilizes into an irregular pattern. (b) Computed fluid surface height viewed from above.

with numerical simulations with coherent sources of Faraday waves arranged on a circular array, shown in Fig. 3-7(b).

We compare the measured periodicities with those predicted by Eq. 3.5, using the Faraday-Talbot length z_F (Eq. 3.4). A plot of the measured periodicity is shown in Fig. 3-8.

With a circular array of 34 pillars, separated by $d = 11$ mm and driven at $f = 55$ Hz (where $\lambda_F = 6.4$ mm, $d \sim 1.5\lambda_F$), the sloshing ridges are alternately out of phase producing the stable pattern shown in Fig. 3-9(a). In this case, the sources have alternating phases, making the periodicity of the array $2d$. The stable Faraday-Talbot pattern matches that obtained from a wave superposition model with alternating phase, shown in Fig. 3-9(b).

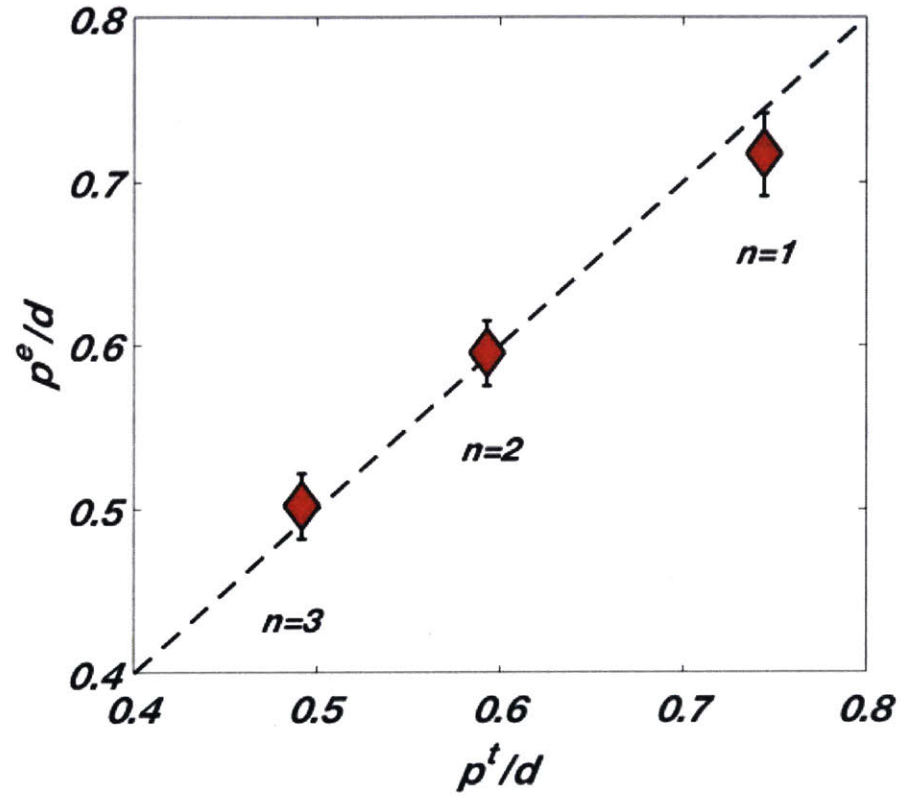

Figure 3-8: Experimentally observed periodicity p^e for a circular array of $R = 51.5$ mm versus predicted periodicity p^c from Eq. 3.5 for $n = 1, 2, 3$. Lengths are non-dimensionalized by the array spacing d. $f = 80$ Hz, $\lambda_F = 4.75$ mm, $d = 9.5$ mm.

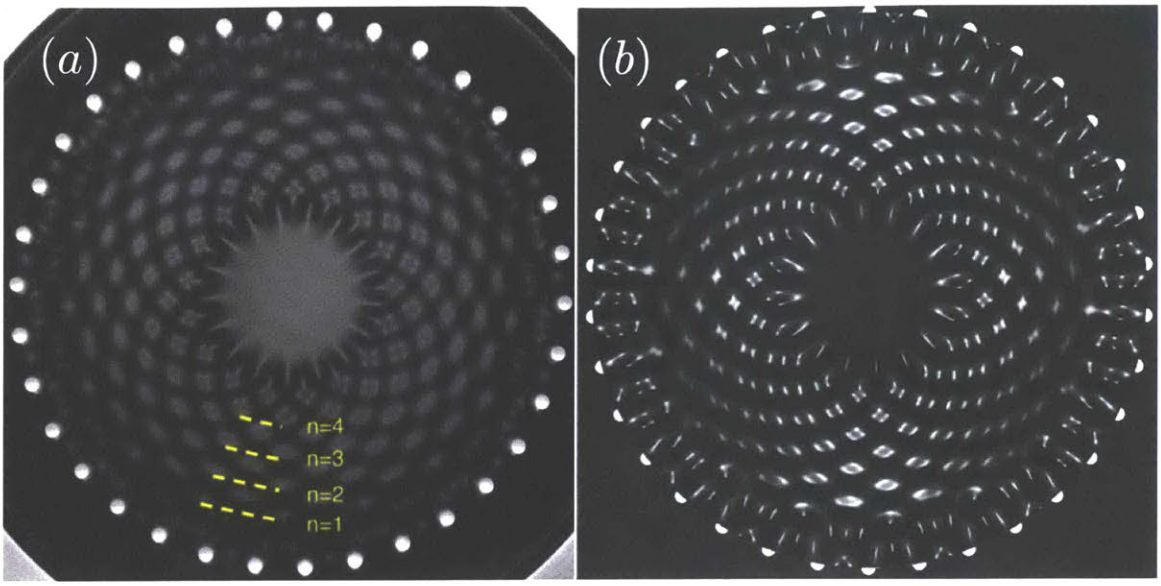

Figure 3-9: (a) Top view of the Faraday Talbot pattern for a circular array of pillars with out-of-phase sloshing ridges. $f = 55$ Hz, $d = 11$ mm, $\lambda_F = 6.40$ mm, $R = 59.5$ mm. The yellow dashed lines show the measured periodicities. (b) Computed fluid surface height viewed from above.

3.4 Trapping of bouncing and walking droplets

We explore the trapping properties of the resulting wavefield for bouncing and walking droplets by introducing droplets of silicone oil on the surface of the bath [17]. The dependence of the bouncing and walking behavior on drop size and forcing acceleration has been well characterized both experimentally [88] and theoretically [71]. We generate stationary bouncing droplets by rapidly extracting a pin to break the interface. We then gradually increase the forcing acceleration until the wavefield generated by the pillars is formed, and track the drift of the bouncing droplets over time. For self-propelling 'walking' droplets, where control of drop size was required, we utilize a piezo-electric droplet generator to make a single droplet of radius $R = 0.395 \pm 0.005$ mm [54]. We then increase the forcing acceleration beyond the Faraday threshold, and direct the walking droplet towards the row of pillars.

In the absence of pillars, static bouncing droplets would bounce in place indefinitely. However, as we gradually increase the forcing acceleration of the bath, enhancing the wavefield generated by the pillars, we note that the droplets begin to

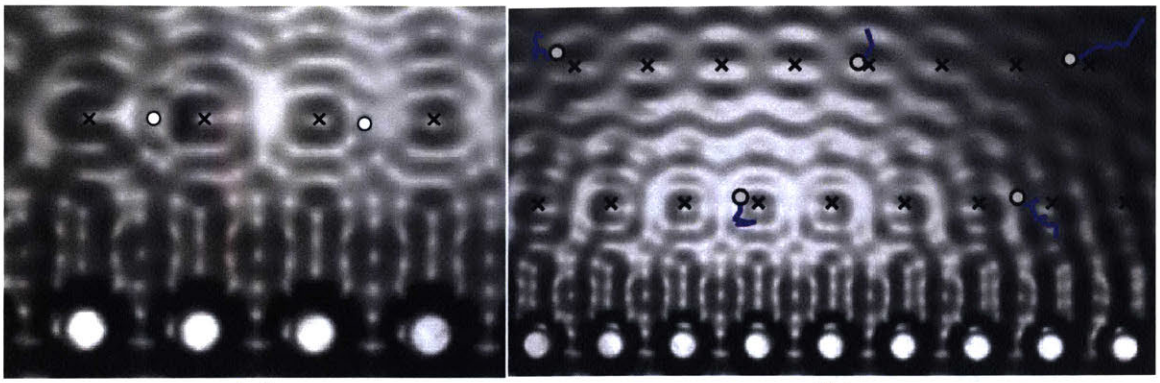

(a) (b)

Figure 3-10: Bouncing droplets (small white circles) drift towards the Faraday-Talbot length, and become localized between consecutive pillar images, denoted by black crosses. (a) Two bouncers trapped within the first row of images. This configuration arises for bouncing droplets of different sizes and bouncing modes. (b) Slow drifting motion of bouncing droplets over time: the white circles indicate the final bouncer positions, and the blue trail their trajectories. Bouncers initially close to the pillars tend to drift towards the first row of images, while more distant bouncers are attracted to the second row of images.

drift. Once the drifting is complete, bouncing droplets align along rows of images, specifically at distances an integer number of the Faraday-Talbot length away from the row of pillars. The bouncing droplets bounce stably between images, as shown in Fig. 3-10(a), where the images are denoted by black crosses.

We note that the drift towards the rows of images arises from a wide range of initial bouncing locations. Fig. 3-10(b) illustrates how bouncing droplets that start close to the row of pillars will drift towards the first row of images and settle there. Bouncers initially placed farther away generally drift towards the nearest row of images, which in Fig. 3-10(b) corresponds to twice the Faraday-Talbot length. The resulting lattice configurations may destabilize in response to drop-drop interactions, when the wavefield generated by the other bouncers supersedes the background wavefield generated by the pillars.

We also explored the behavior of relatively energetic walking droplets near the Talbot images when the forcing acceleration was above the Faraday threshold, $\gamma \geq \gamma_F$. Specifically, we generated droplets of radius $R = 0.395 \pm 0.005$ mm and free walking speed $u_0 \approx 16$ mm/s, and directed them toward the row of pillars. After

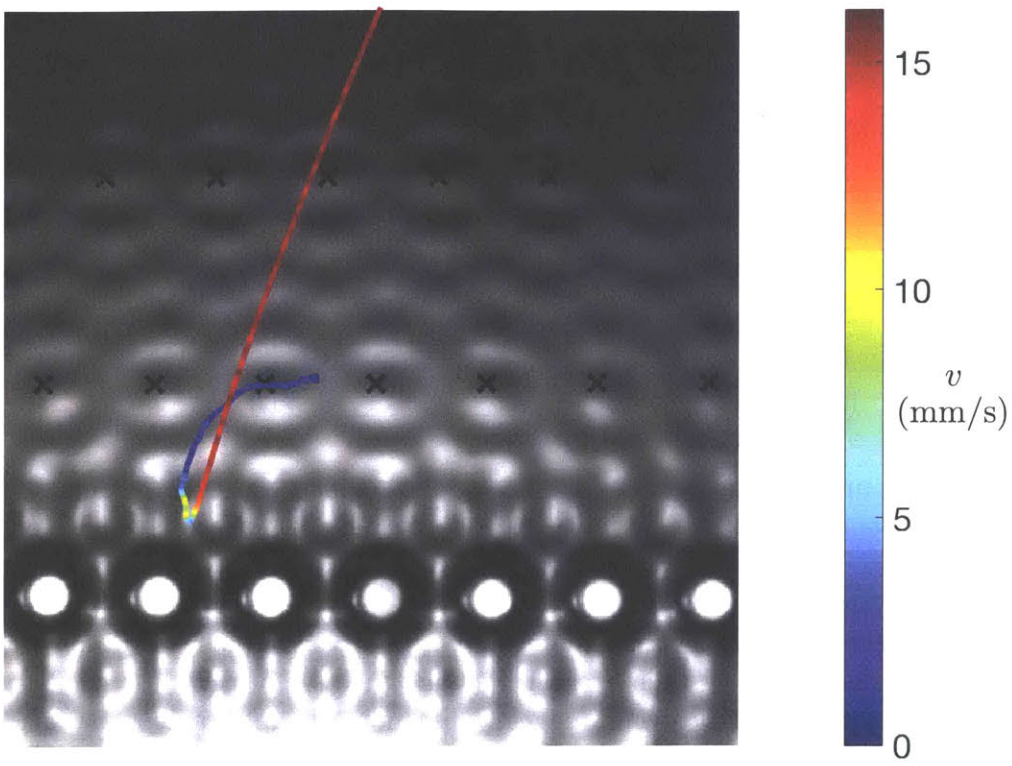

Figure 3-11: A walking droplet with radius $R = 0.395 \pm 0.005$ mm impinges on a row of pillars. The droplet approaches with a speed of approximately 16 mm/s before being transformed from a resonant walker to a chaotic bouncer. Thereafter, it slowly drifts towards the first row of Talbot images. The droplet trajectory is color-coded according to speed.

interacting with the row of pillars, the vertical dynamics of the droplets can change drastically, transforming a fast walker into a chaotic bouncer. This bouncer may then exhibit behavior similar to those in the previous experiments, slowly drifting towards the Faraday-Talbot length, with a tendency to settle between images. A sample trajectory is shown in Fig. 3-11, emphasizing how the droplet's horizontal speed changes drastically after interacting with the pillar.

3.5 Discussion

We have reported a hydrodynamic analog of the Talbot effect arising on the surface of a vertically shaken fluid with a periodic array of protruding pillars. The effect is observed only for driving frequencies such that the Faraday wavelength is approxi-

mately half the pillar spacing and for driving accelerations that are approximately $0.2 - 1\%$ above the Faraday threshold. The patterns oscillate at half the driving frequency, revealing their sources as sloshing Faraday waves excited between the pillars. A Faraday-Talbot length was defined (Eq. 3.4) that rationalizes the locations of the in-phase and shifted out-of-phase self-images.

Video recordings show laterally sloshing fluid ridges between the pillars that act as the Faraday wave sources. There are also quickly decaying meniscus waves emitted from the pillars at the driving frequency that mix with the Faraday waves close to the pillars. While the self-images are formed from Faraday waves, the presence of meniscus waves adjoining the pillars plays a critical role in seeding the Faraday waves. The importance of the meniscus waves was underscored when we tried the experiment using arrays of submerged pillars (0.3 mm below the fluid surface), and the self-imaging did not arise.

In the optical Talbot effect, the observed light intensity is due to the diffraction and interference of light from an illuminated grating. Although the grating is a passive element, it modulates the light, producing a coherent, periodic source of waves emanating from the grating. In our experiment, sloshing waves generated by the row of pillars serve as the active element. The coherent waves emanating from between the pillars interfere to form the observed Faraday-Talbot pattern. In both cases, the pattern is the result of interference of waves from coherent periodic sources.

We have also explored the emergence of Faraday-Talbot patterns generated by circular arrays of pillars, and compared the periodicity of the self-images to those reported in optical studies of the Talbot effect with curved gratings. We obtained transient patterns displaying the coherent Faraday-Talbot effect and stable patterns displaying the alternating phase Faraday-Talbot effect. As in the optical case the curvature of the array caused demagnification of the pattern.

The possibility of using the Faraday-Talbot effect for trapping bouncing and walking droplets has been demonstrated, and represents a hydrodynamic analog of particle trapping with the Talbot effect [76, 98, 68]. Stationary bouncers simply drift towards the images, to be trapped between them. The relatively energetic walkers have their

vertical dynamics altered through their interaction with the pillars, resulting in stationary bouncers trapped between the Faraday-Talbot images. Finally, in the broader context of hydrodynamic analogs with the Faraday system [14, 39], this represents the first example of an analog of an optical system arising above the Faraday threshold, a parameter regime to be explored further in Chapter 4.

Chapter 4

Crossing the Faraday threshold

4.1 Introduction

Droplets walking on a vibrating fluid bath have been shown to exhibit several features of quantum mechanical systems [14], including quantized orbits [41, 52, 86, 28], tunneling [31, 73], and the emergence of multimodal statistics in confined geometries [55, 94]. Walking droplets are an example of a pilot-wave system: the droplet generates a wave at every impact with the bath and is, in turn, guided by the local slope of the bath surface, whose form is prescribed by the superposition of waves generated from previous bounces. The longevity of the waves is controlled by the vibrational acceleration of the bath, γ. If $\gamma < \gamma_F$, where γ_F is the Faraday threshold, the surface would remain unperturbed in the absence of the drop [3]. As γ approaches γ_F from below, linear waves generated by the drop persist for the memory time $T_M = T_d/(1 - \gamma/\gamma_F)$, where $T_d \sim \lambda_F^2/\nu$ is the temporal decay time of the waves in the absence of forcing [32]. Nonlinear wave effects are expected to be important near the Faraday threshold. For $\gamma > \gamma_F$, the entire surface becomes unstable to the Faraday instability, so that waves appear throughout the bath. In previous experimental investigations of this hydrodynamic pilot-wave system, care was taken to ensure that γ remained below γ_F, thus avoiding the appearance of a background

This chapter was submitted for publication as: "Bouncing droplet dynamics above the Faraday threshold," L. D. Tambasco, J. J. Pilgram and J. W. M. Bush, (Submitted, 2018) [104].

Faraday wavefield and ensuring that the drop was guided solely by its pilot-wave field. For $\gamma < \gamma_F$, the walking drops execute rectilinear motion provided they are sufficiently far from boundaries [115, 89].

According to stochastic electrodynamics, microscopic quantum particles interact with a background field, specifically zero-point electromagnetic vacuum fluctuations [12]. Notably, the inferred energy spectrum of this zero-point field $E(\omega) = \hbar\omega/2$ allows for the introduction of Planck's constant, $\hbar$, into a classical theory [12]. The zero-point field has been sought as the basis for an electromagnetic pilot-wave theory in quantum mechanics [21, 22], in which case it would play the role of the vibrating bath in the hydrodynamic pilot-wave system in energizing the system [14]. Stochastic dynamics [74, 48], de Broglie's pilot-wave theory [20], and Bohmian mechanics [9] have all likewise sought to rationalize quantum mechanics in terms of interactions between microscopic particles and a stochastic background field. With a view to introducing an irregular forcing into this hydrodynamic pilot-wave system and so exploring a regime that might potentially yield new hydrodynamic quantum analogs, we were thus compelled to examine the dynamics of bouncing droplets interacting with a background field consisting of the Faraday wavefield arising for $\gamma > \gamma_F$.

In the hydrodynamic system, the waves serve to propel the bouncing drops by imparting an impulse during impact. If the vertical dynamics of the droplet are aperiodic, that is, the phase of impact relative to the Faraday wave changes with every bounce, then the resulting lateral impulses will be irregular. These impulses are thus expected to serve as a source of stochasticity in hydrodynamic pilot-wave systems and so may give rise to new dynamical states. For example, Oza *et al.* [79] theoretically demonstrated that self-orbiting states exist but are unstable for accessible fluid parameters below the Faraday threshold. The introduction of a stochastic element has been posited as a means to stabilize such hydrodynamic spin states [63]. The question naturally arises as to whether these spin states might exist above the Faraday threshold.

Only one previous study has examined the behavior of bouncing drops above the Faraday threshold [100], as reported in Chapter 3. We introduced an array of pillars

to the bath and observed that, for $\gamma/\gamma_F \simeq 1.02$, the form of the Faraday waves in the vicinity of the pillars is analogous to that arising in the optical Talbot Effect [101]. The resulting Faraday-Talbot wave pattern was capable of trapping both walking and bouncing droplets in its troughs, a hydrodynamic analog of particle trapping with the Talbot effect [76, 98, 68]. We here characterize the dynamics of droplets above the Faraday threshold in the absence of pillars, and identify the regimes where droplets become trapped by the underlying Faraday wavefield.

The bouncing and walking behavior of drops on a bath vibrating below the Faraday threshold have been thoroughly characterized experimentally [32, 88, 33], and considerable effort has been devoted to rationalizing this behavior theoretically [115, 71, 72, 28, 70]. We here extend the regime diagrams of Wind-Willassen *et al.* [115] for silicone oil droplets of kinematic viscosity 20 and 50 cSt at driving frequencies of 80 and 50 Hz, respectively. In Section 4.2, we describe our experimental apparatus and methods. In Section 4.3 we enumerate the dynamic states arising above the Faraday threshold. In Section 4.4, we examine the dynamics of drops bouncing erratically above the Faraday threshold, demonstrating that they exhibit behavior akin to a two-dimensional random walk. We then characterize the dependence of the effective drop diffusivity on droplet size and forcing acceleration, and rationalize this dependence via simple scaling arguments.

4.2 Experiments

We explore the bouncing and walking dynamics above the Faraday threshold in a circular bath filled to a depth of $h = 6$ mm with silicone oil of viscosity $\nu = 20$ or 50 cS. A schematic of the experimental arrangement is presented in Fig. 4-1. The bath is vibrated vertically with amplitude A, frequency f and acceleration $\Gamma(t) = \gamma\cos(2\pi ft)$, where $\gamma = A(2\pi f)^2$. Two vibrational frequencies are considered, $f = 50$ Hz for the 50 cS oil, and $f = 80$ Hz for the 20 cS oil, the combinations considered below threshold in prior work [88, 71, 115]. When the vibrational acceleration is sufficiently large, $\gamma > \gamma_F$, the surface of the bath becomes unstable to subharmonic

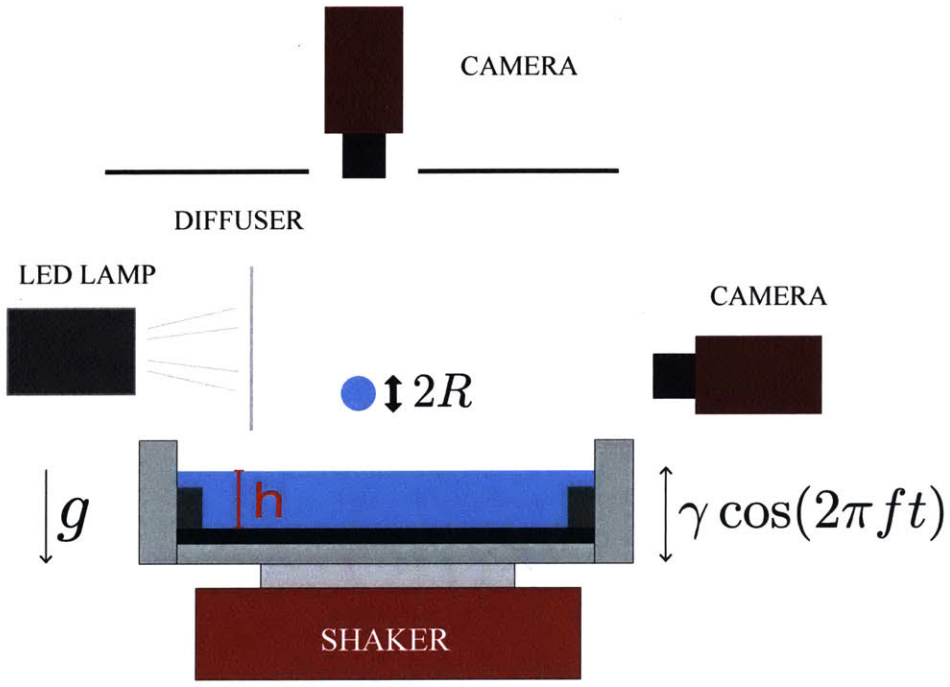

Figure 4-1: Experimental arrangement [53]. The fluid bath is shaken using an electromagnetic shaker coupled with an air bearing that constrains the vibrations to be vertical. A CCD camera placed above the bath captures the horizontal dynamics, and a high-speed Phantom camera allows for resolution of the vertical dynamics.

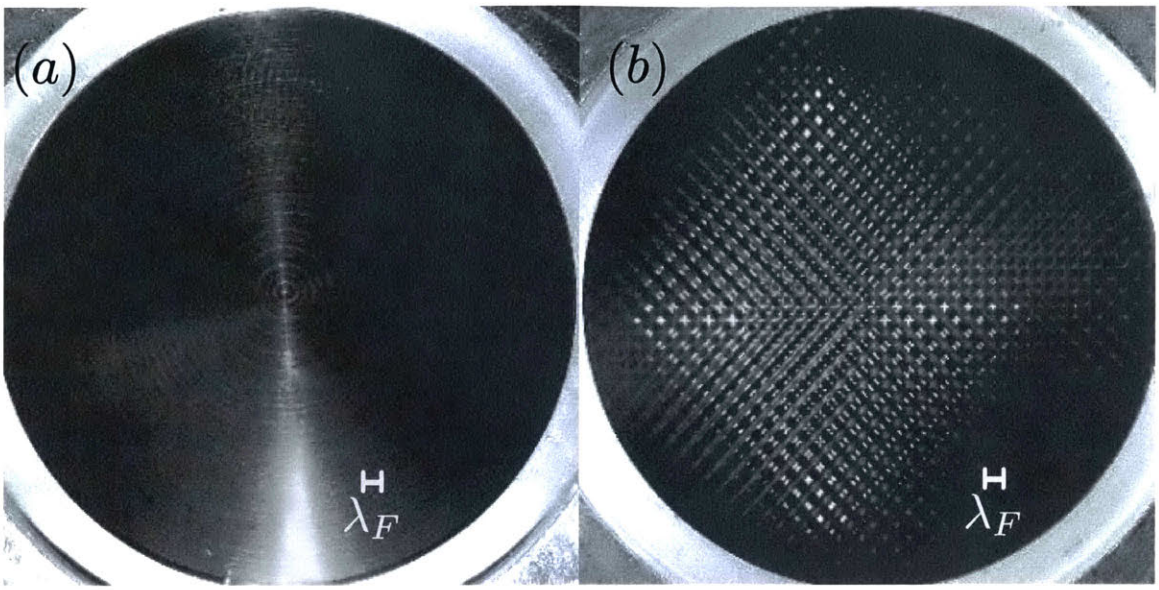

Figure 4-2: (a) Circularly-symmetric Faraday pattern arising at the onset of the Faraday instability, $\gamma/\gamma_F \approx 1.01$. (b) Checkerboard Faraday pattern emerging at $\gamma/\gamma_F = 1.05$.

Faraday waves that oscillate with frequency $f/2$ and wavelength $\lambda_F = 2\pi/k_F$. The observed wave-number k_F is well described by the standard water-wave dispersion relation

$$\omega_F^2(k) = \left(gk + \frac{\sigma}{\rho}k^3\right)\tanh(kh), \tag{4.1}$$

where $\omega_F = \omega/2 = \pi f$ is the subharmonic angular frequency, g the gravitational acceleration, σ the surface tension, ρ the fluid density. For the depth considered, $h = 6$ mm, a vibrational frequency $f = 80$ Hz corresponds to a Faraday wavelength $\lambda_F = 4.75$ mm, and 50 Hz to $\lambda_F = 6.98$ mm.

While the wavelength is prescribed by Eq. 4.1, the wave pattern realized depends on both container shape and vibrational acceleration. For our circular bath, the most unstable mode at the onset of the Faraday instability, $\gamma \simeq \gamma_F$ is a boundary-dominated circularly-symmetric wave, with crests arranged in concentric rings separated by λ_F (Fig. 4-2(a)). As the forcing acceleration γ is increased beyond approximately $1.015\gamma_F$, the circularly symmetric wavefield is replaced by a checkerboard pattern with characteristic spacing λ_F (Fig. 4-2(b)). In this regime, the boundary

Figure 4-3: Faraday wave rupture generates drops when the vibrational acceleration is sufficiently high, $\gamma > \gamma_R$ ($= 4.02\gamma_F$ for 20 cS oil vibrated at 80 Hz).

geometry has effectively no influence on the background field of Faraday waves. Successive instabilities arising as γ increases progressively beyond γ_F have been characterized by Douady [26]. At the highest forcing acceleration considered in our study, $\gamma/\gamma_F = 1.2$, the background wavefield consisted of a standing checkerboard pattern.

When the vibrational acceleration is sufficiently large, the interface breaks, generating droplets (Fig. 4-3). The critical acceleration for surface rupture in a vertically vibrating bath has been determined empirically and theoretically [90, 47]. For low viscosity fluids, the interface breaks when the upward inertial force due to the vibrational acceleration $\gamma \sim 4g$ exceeds the stabilizing force associated with surface tension: $m\gamma > 2\pi\lambda_F\sigma$, where $m \sim \rho\lambda_F^3$ is the accelerated fluid mass. Using the dispersion relation for deep-water capillary waves for λ_F yields the critical acceleration γ_R for interfacial rupture,

$$\gamma_R = C\left(\frac{\sigma}{\rho}\right)^{1/3}\omega^{4/3}, \tag{4.2}$$

where C is an $\mathcal{O}(1)$ constant that depends on the fluid-frequency combination. For 20 cS silicone oil vibrated at 80 Hz, $\gamma_R/\gamma_F \approx 4.02$, while for 50 cS oil vibrated at 50

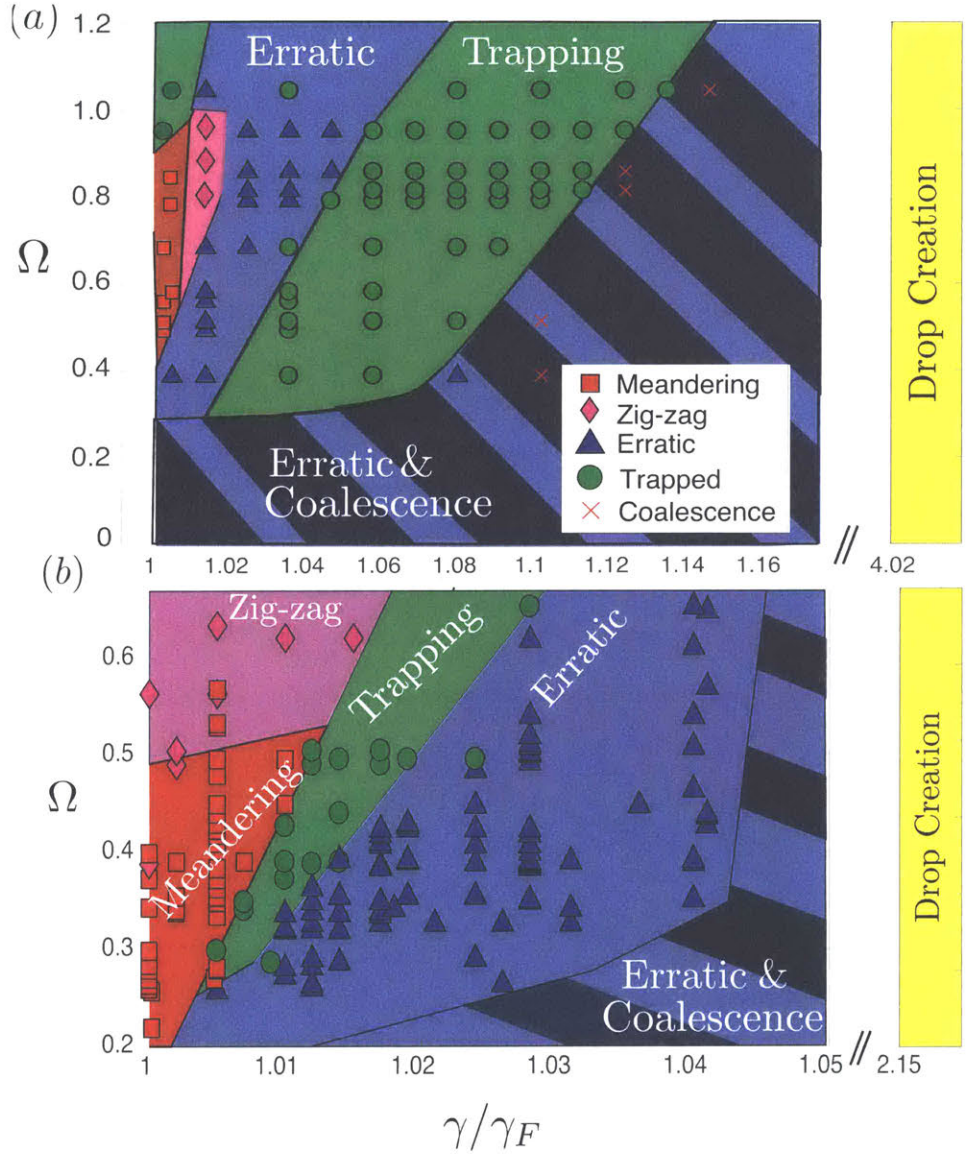

Figure 4-4: Regime diagrams indicating the behavior of drops levitated on a vibrating bath. We delineate the parameter regimes as a function of the dimensionless forcing acceleration γ/γ_F and vibration number $\Omega = \omega/\sqrt{\sigma/(\rho R^3)}$. (a) 20 cS silicone oil driven at 80 Hz and (b) 50 cS silicone oil driven at 50 Hz. The meandering regime is indicated in red, zig-zagging in pink, erratic bouncing in blue, trapping in green, and coalescing in striped black/blue regions. Yellow indicates the regime of spontaneous drop creation from breaking Faraday waves, as arises when the forcing acceleration exceeds the threshold for interface rupture ($\gamma > \gamma_R$).

Hz, $\gamma_R/\gamma_F \approx 2.15$.

In order to characterize the droplet dynamics above the Faraday threshold, we use a piezo-electric droplet generator [54] to repeatably create drops of uniform radii R in the range 0.2 mm $< R <$ 0.5 mm (with $\pm 0.5\%$ variability). We generate a single drop, place it at the center of the domain, and then affix a circular acrylic lid on top of the bath to eliminate the influence of air currents. We gradually increase the forcing acceleration beyond the Faraday threshold, $\gamma > \gamma_F$. A CCD camera placed above the bath captures the horizontal motion of the drop. An LED lamp and diffuser illuminate the setup from the side while a high-speed Phantom camera placed beside the bath captures the vertical dynamics, also allowing for accurate measurement of the drop radius.

We sweep through the forcing accelerations above the Faraday threshold, $\gamma/\gamma_F > 1$, at increments $\Delta\gamma/\gamma_F = 0.001$ for drops with radii in the range 0.1 mm $< R <$ 0.5 mm, corresponding to non-dimensional vibration numbers $\Omega \equiv \omega/\sqrt{\sigma/(\rho R^3)}$ in the range $[0.1, 1.2]$. For each value of the forcing acceleration, we record the trajectory of the drop for one minute, or until it reaches the edge of the circular bath. We use the recordings to characterize the dynamics, as will be summarized in Section 4.3.

We characterize droplet trajectories in terms of a persistence length [40] L_p, defined as

$$\langle \cos\theta \rangle = e^{-s/L_p}, \tag{4.3}$$

where θ is the angle between the tangent velocity vectors at an initial point and at another point an arclength s further along the trajectory. $\langle \cdot \rangle$ indicates the average value over all initial points along a single trajectory. The relative magnitudes of L_p, the characteristic length over which the drop changes direction, and the Faraday wavelength λ_F provides a quantitative means of classifying the coherence of the trajectories through the non-dimensional persistence length $\Lambda = L_p/\lambda_F$.

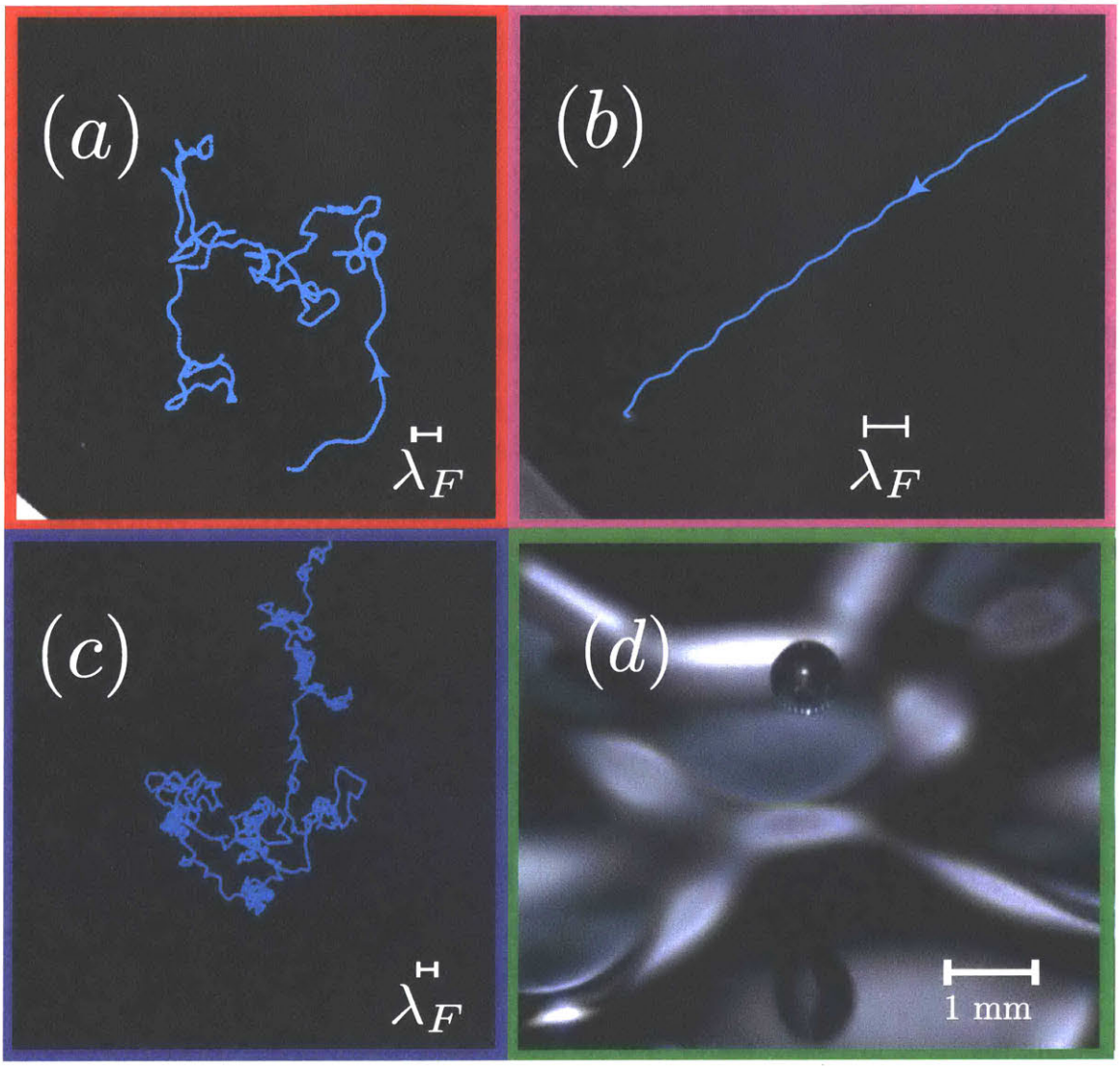

Figure 4-5: Dynamic states observed for $\gamma > \gamma_F$. (a) Meandering trajectory, characterized by a persistence length greater than the Faraday wavelength, $\Lambda = L_p/\lambda_F > 1$. For this particular trajectory, $\Lambda = 1.15$. (b) A zig-zagging trajectory is characterized by small amplitude lateral oscillations, with wavelength on the order of λ_F, along a mean rectilinear trajectory. The drop navigates the crests and troughs of the underlying checkerboard Faraday wave pattern. (c) Erratic walking, characterized by a dimensionless persistence length $\Lambda < 1$. For this particular trajectory, $\Lambda = 0.24$. (d) Side view of a droplet trapped above the Faraday threshold in a (4,1) bouncing mode. The drop bounces in place on the trough of the underlying subharmonic wave once every 4 driving periods (with period $2T_F$).

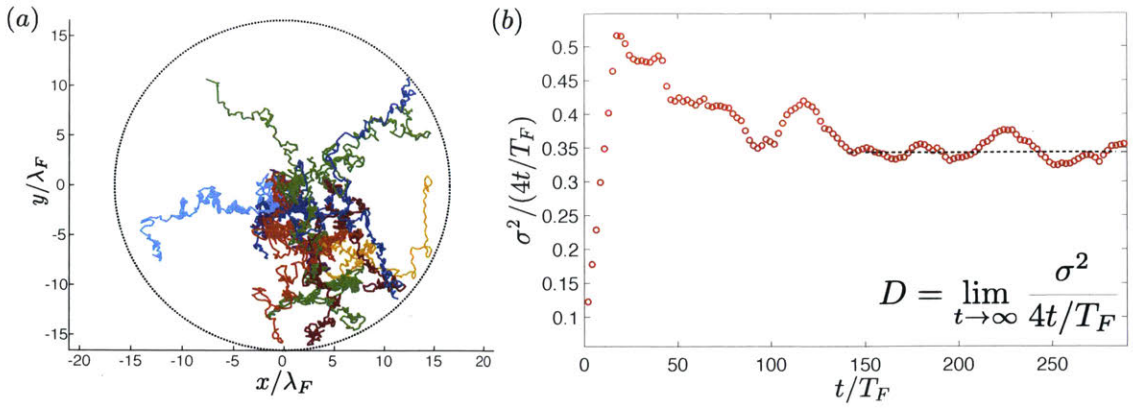

Figure 4-6: (a) Erratic trajectories resembling two-dimensional Brownian motion. The circle indicates the boundary of the bath. (b) The effective diffusivity D for the trajectories in Fig. 4-6(a) may be computed from the long-time limit of the mean-squared displacement scaled by the non-dimensional time $4t/T_F$.

4.3 Results

We summarize the observed droplet dynamics above the Faraday threshold for 20 cS silicone oil driven at 80 Hz in the regime diagram shown in Fig. 4-4(a). For all driving accelerations above γ_F, the smallest drops ($R < 0.2$ mm, corresponding to $\Omega < 0.31$) tend to bounce irregularly, moving erratically in the horizontal until eventually coalescing. We note that similar behavior also arises for these drops below the Faraday threshold [71].

Slightly larger drops (0.2 mm $< R <$ 0.4 mm, or $0.31 < \Omega < 0.86$) walk along straight paths below γ_F. For $\gamma > \gamma_F$, they follow meandering trajectories, such as that shown in Fig. 4-5(a), characterized by a relatively large non-dimensional persistence length, $1 < \Lambda < 2$. In this regime, the amplitude of the Faraday wavefield is small relative to the drop's pilot-wave, so only weakly alters the walker's direction. We note also that small loops of radius $\lambda_F/2$ were often apparent in meandering trajectories (Fig. 4-5(c)), indicating a tendency towards hydrodynamic spin states [79, 63]. However, the underlying wavefield is still insufficient to stabilize these spin states: in the parameter regime considered, the loops were always transient, never stable.

As the forcing acceleration is further increased ($\gamma/\gamma_F \sim 1.015$), meandering gives way to relatively regular zig-zagging trajectories, as shown in Fig. 4-5(b), a transition

that coincides with the emergence of a checkerboard Faraday pattern on the fluid surface (Fig 4-2(b)). In zig-zagging trajectories, the drop slightly deviates from a straight-line path, with oscillations perpendicular to its direction of mean motion. The oscillations occur with a characteristic wavelength on the order of λ_F, indicating that the drop is navigating the background checkerboard field of Faraday waves.

For $1.015 \lesssim \gamma/\gamma_F \lesssim 1.04$, the amplitude of the underlying Faraday wave becomes significantly larger than that of the pilot-wave generated by the drop, and the droplet motion becomes highly irregular (see Fig. 4-5(c)). Due to the loss of resonance in the vertical dynamics, each impact arises at a different phase, so the drop impacts a different waveform at every bounce. Since the drop's horizontal motion is driven by the gradient of the underlying wave, it changes direction in response to these varying impulses on the time-scale of its characteristic bouncing period T_F. The frequent change of direction translates to a dimensionless persistence length less than 1, typically in the range $0.1 < \Lambda < 0.5$, allowing for differentiation from the meandering trajectories arising at lower γ/γ_F.

For $\gamma/\gamma_F \gtrsim 1.04$, the checkerboard pattern is able to trap droplets of a certain size, causing them to bounce in place. A trapped droplet is shown in Fig. 4-5(d); the droplet bounces periodically in a (4,1) bouncing mode, once every 4 driving periods [44]. We note also that the trapping is relatively robust; perturbations to trapped states cause the drop to move erratically for a few seconds of transient motion before being trapped in another trough. A further increase in forcing acceleration ($\gamma/\gamma_F \gtrsim 1.12$) leads to longer transients thereby increasing the likelihood of drop coalescence. Finally, the largest drops considered ($R > 0.45$ mm, or $\Omega > 0.86$) tend to bounce in place at the onset of the Faraday threshold, but then undergo similar transitions, from erratic motion to trapping, and eventually erratic bouncing and coalescence.

Fig. 4-4(b) shows the regime diagram for 50 cS oil driven at 50 Hz above the Faraday threshold. The observed dynamical states are similar to those observed for the 20 cS – 80 Hz viscosity-frequency combination, but the transitions happen over a significantly smaller range of forcing accelerations. We note that the range of droplet

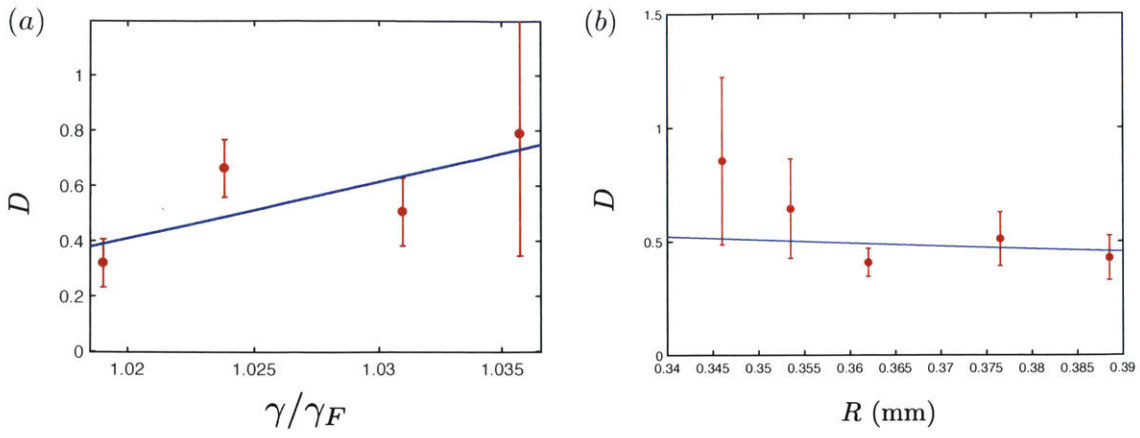

Figure 4-7: The observed dependence of the effective diffusion coefficient D on (a) the forcing acceleration γ/γ_F for a drop of radius $R = 0.376$ mm, and (b) the droplet radius R for $\gamma/\gamma_F = 1.031$. Dashed curves correspond to the effective diffusivity obtained from scaling arguments, Eq. 4.6. We note that surface diffusion arises in a relatively narrow region of parameter space ($1.015 \lesssim \gamma/\gamma_F \lesssim 1.04$) for 20 cS – 80 Hz configuration as shown in Fig. 4-4(a), so only small variations in the effective diffusivity are apparent.

sizes that can be levitated in this parameter regime is smaller. Below the Faraday threshold, all droplets are walkers in the drop size range considered [115]. Just above the threshold, smaller droplets ($R < 0.38$ mm, $\Omega < 0.50$) meander, while larger drops ($R > 0.38$ mm, $\Omega > 0.50$) zig-zag. Stable droplet trapping is observed over a narrow range of forcing accelerations ($1.005 \lesssim \gamma/\gamma_F \lesssim 1.02$). For larger γ, trapping states become unstable, giving rise to erratic bouncing. Drops of all sizes eventually coalesce for $\gamma/\gamma_F \gtrsim 1.04$. Spontaneous droplet creation through interfacial fracture occurs for $\gamma > \gamma_R = 2.15\gamma_F$.

4.4 2D effective diffusion

Brownian motion may be characterized in terms of a diffusion coefficient,

$$D = \lim_{t\to\infty} \frac{\sigma^2(t)}{4t}, \tag{4.4}$$

where $\sigma^2(t)$ is the variance in position, or mean-squared displacement, of many realizations of the associated random walk as a function of time. We can thus compute

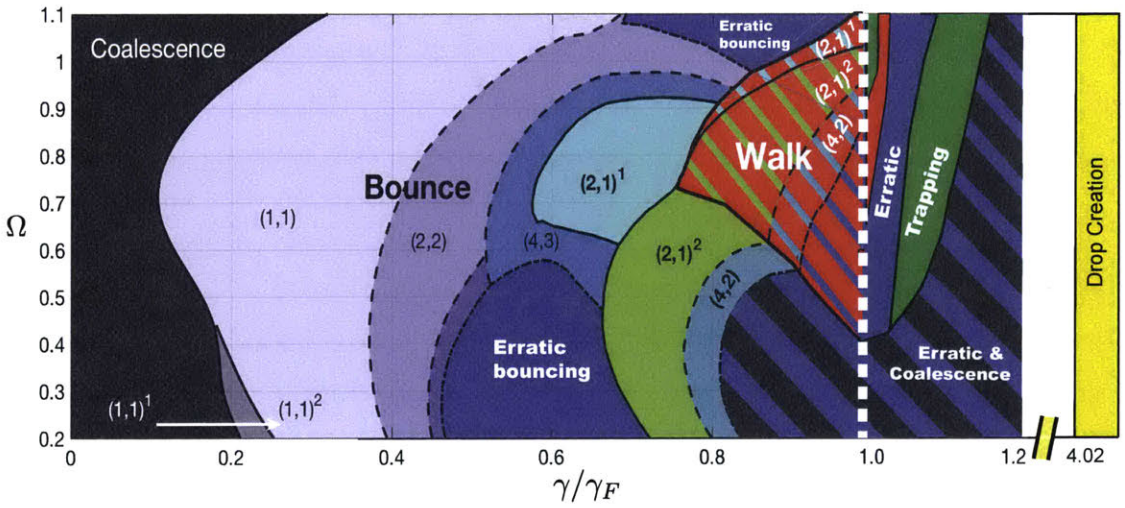

Figure 4-8: An extension of the regime diagram obtained by Moláček & Bush [72] for 20 cS silicone oil driven at 80 Hz, including droplet dynamics above the Faraday threshold, as reported in Fig. 4-4(a). We delineate the parameter regimes as a function of the dimensionless forcing acceleration γ/γ_F and vibration number $\Omega = \omega/\sqrt{\sigma/(\rho R^3)}$. Walkers transition into the meandering and zig-zagging regimes. Small erratic bouncers ($R < 0.2$ mm, $\Omega < 0.31$) tend to coalesce just above the Faraday threshold, while large bouncers ($R > 0.45$ mm, $\Omega > 0.86$) tend to drift until being trapped.

the effective diffusivity in the erratic bouncing (blue) region in Fig. 4-4. For each combination of droplet size and forcing acceleration, we recorded 10 trajectories such as those shown on Fig. 4-6(a), and calculated the corresponding mean-squared displacement, which is shown to scale linearly with time in the long-time limit (Fig. 4-6(b)). We take the last 100 values of the mean-squared displacement and use their mean to obtain the effective diffusivity, and their standard deviation for error bars.

Over the relatively small parameter regime of interest (see Fig. 4-4), the effective diffusivity depends only weakly on forcing acceleration and droplet size. As γ increases, the diffusion process is slightly enhanced, as suggested by Fig. 4-7(a). Similarly, Fig. 4-7(b) suggests that smaller drops tend to diffuse slightly faster than larger drops. We proceed by obtaining a rough scaling argument for the dependence of diffusivity on drop size and forcing acceleration by modeling the impact of the droplet with the bath using a linear spring [71] with a spring constant proportional to the surface tension σ [44]. A drop of radius R and mass $m = 4\rho\pi R^3/3$ will have characteristic speed $v \propto \sqrt{\sigma/\rho R}$ after impact, assuming a penetration depth $\Delta z \sim R$. The horizontal component of the drop's velocity v_x depends on the slope of the surface, which scales as $\eta/\lambda_F \sim \sqrt{(\gamma/\gamma_F - 1)}$ due to the supercritical bifurcation at the onset of the Faraday instability [118]; thus,

$$v_x \sim \sqrt{\frac{\sigma}{\rho R}}\frac{\eta}{\lambda_F} \sim \sqrt{\frac{\sigma(\gamma/\gamma_F - 1)}{\rho R}}. \tag{4.5}$$

Over one bounce, the droplet will traverse a characteristic distance $\Delta x = v_x T_F$. Since the drop is changing directions at nearly every bounce in the erratic regime, the characteristic time-scale is $\Delta t = T_F$, yielding a scaling for the effective diffusivity

$$D \equiv \frac{(\Delta x)^2}{\Delta t} = v_x^2 T_F \sim \frac{\sigma T_F}{\rho R}\left(\gamma/\gamma_F - 1\right). \tag{4.6}$$

The weak trends evident in Fig. 4-7, of D increasing with the distance from threshold $(\gamma/\gamma_F - 1)$ and decreasing with radius R are both consistent with this simple scaling. While these trends are barely discernible over the limited parameter regime

accessible in the systems considered, they may have some bearing in a more general pilot-wave setting.

4.5 Discussion

We have expanded the characterization of bouncing and walking droplet dynamics, extending the regime diagrams for 20 cS–80 Hz and 50 cS–50 Hz configurations above the Faraday threshold. We classified the droplet dynamics into the following regimes: trapped, coalescing, zig-zagging, meandering, and erratic bouncing. The meandering and erratic bouncing regimes were differentiated on the basis of the dimensionless persistence length $\Lambda = L_p/\lambda_F$. At the onset of the Faraday instability, while the drop's pilot-wave is still comparable in amplitude to the unstable background Faraday wave, coherent motion (zig-zagging or meandering) arises, characterized by a dimensionless persistence length $\Lambda \gtrsim 1$. As the forcing acceleration is increased further, the background Faraday wavefield dominates the pilot-wave, causing the drop to change directions more frequently and abruptly, so that $0.1 < \Lambda < 0.5$. The impact of the relative contribution of the pilot-wave and the unstable Faraday wavefield on drop dynamics in different geometric settings is a subject of current interest. In Chapter 5, we discuss the interaction of a walker and the wavefield generated by a circular well, assessing the ability of the well-induced waves to trap the walkers.

In Fig. 4-8, we summarize our results in a regime diagram for levitating drops of 20 cS oil driven at 80 Hz that combines Fig. 4-4(a) with the regime diagram presented in Fig. 11(d) of Moláček & Bush [72]. We note that the meandering and zig-zagging regimes are a continuous extension of the walking regime observed below the Faraday threshold. Likewise, the erratic bouncing and coalescing regime arising for smaller drops is simply a continuation of that below the threshold. We note that the boundaries of the regime diagram are determined empirically. The form of previous regime diagrams was rationalized through consideration of the dynamic interaction between the bouncing drop and its wavefield [115, 71, 72]. Below γ_F, the wave forms may be described in terms of a superposition of linear waves, an

assumption that breaks down at and above the Faraday threshold. While providing theoretical rationale for the behavior for $\gamma > \gamma_F$ is thus not straightforward, it is hoped that our study may serve to motivate and guide further theoretical developments.

We have further characterized the emergence of Brownian motion above the Faraday threshold. In the erratic regime, when the bouncing of the drop is not synchronized with the Faraday wave, the force imparted by the bath changes at every impact in both magnitude and direction. This asynchrony introduces an irregular component into the drop's trajectories, leading to the emergence of trajectories that may be described in terms of classical diffusion, with a diffusivity that increases with forcing amplitude and decreases with drop size, trends rationalized with simple scaling arguments.

If unperturbed by boundaries or applied forces, a walker at $\gamma < \gamma_F$ executes rectilinear motion at its free walking speed. This simple base state might be taken as a shortcoming of the walker system as a quantum analog system if one assumes that quantum particles diffuse in some fashion. However, the solution of the time-dependent linear Schrödinger equation for the probability density of a single free particle initially localized to the extent possible given Heisenberg's uncertainty relation, $\Delta p \Delta x \geq \hbar/2$, indicates ballistic diffusion, for which the variance $\sigma^2 \sim t^2$. This solution is thus consistent with the rectilinear motion of an ensemble of quantum particles with initial positions and momentum distributions prescribed by the uncertainty relations. According to the ensemble or statistical interpretation of quantum mechanics [1], quantum diffusion may thus be simply understood as resulting from the uncertainty of the particle's initial conditions [48].

The walker's base state of rectilinear motion is thus not necessarily a shortcoming of the system as a hydrodynamic quantum analog, and its free walking velocity should be taken as the analog of $\hbar\mathbf{k}/m$. It remains an open question as to whether a stochastic forcing need be invoked in the walker system to capture certain features of quantum mechanics, or whether chaotic pilot-wave dynamics will be sufficient.

Chapter 5

Orbital dynamics in a generalized pilot-wave framework

5.1 Introduction

The vertical and horizontal dynamics of a droplet walking on a vibrating fluid bath have been subject of considerable recent interest [17, 14]. The walking droplet system is the first macroscopic realization of a pilot-wave system of the form envisioned by Louis de Broglie [20], displaying various quantum-like features, including quantized orbits [41, 52], double quantization [86, 28], tunneling [31, 73], and the emergence of multimodal statistics in confined geometries [55, 94]. In this hydrodynamic pilot-wave system, walking droplets generate a wave at impact with the bath surface, and are in turn piloted by the resulting superposition of waves. The temporal decay time of the waves T_M increases monotonically with vibrational acceleration γ, provided $\gamma < \gamma_F$, the Faraday threshold above which waves form on the surface in the absence of a drop. The horizontal motion of the droplet depends on the gradient of the pilot-wave at the impact position, and a time-averaged drag term, proportional to the droplet's velocity [80, 72]. A drop's trajectory may be further affected by an external force acting on the drop, such as a Coriolis force, as arises on a rotating

This chapter was submitted for publication as: "Exploring orbital dynamics and trapping with a generalized pilot-wave framework," L. D. Tambasco and J. W. M. Bush (Submitted, 2018) [102].

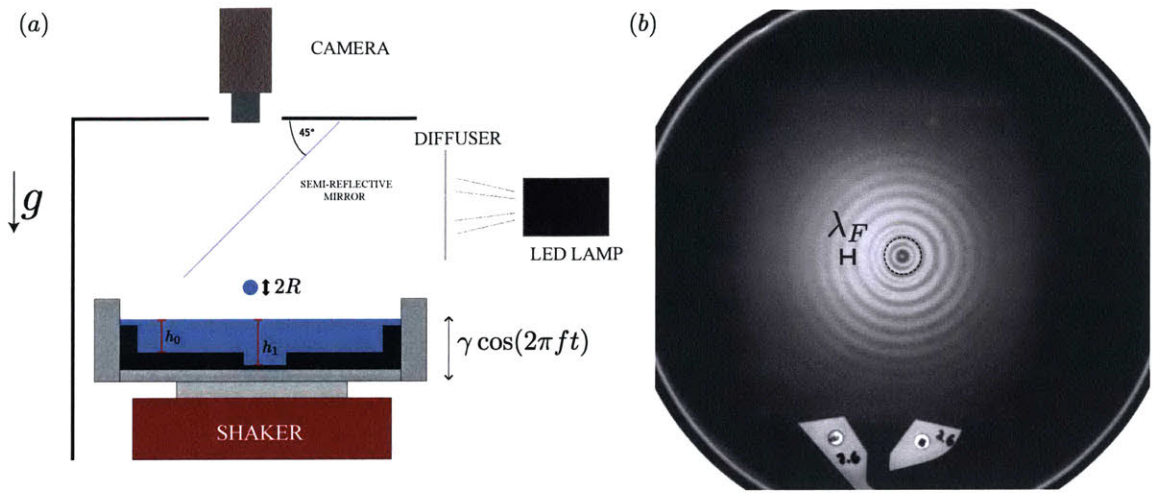

Figure 5-1: (a) Experimental setup. A droplet of radius R bounces on a bath vibrating vertically with frequency $f = 80$ Hz and vibrational acceleration γ, with a central circular well of depth $h_1 = 6.5$mm. The experiment is imaged from above, illuminated by a diffused light via a semi-reflective mirror. (b) Top view of the most unstable circularly-symmetric Faraday mode induced by the well for $\gamma = 4.0$g. The boundary of the well is delineated by a dashed line. The Faraday threshold has been crossed only in the region directly above the well, so that $\gamma_F^d < \gamma < \gamma_F^s$.

bath [52, 41, 79, 83], or a linear spring force as generated from a magnetic field acting on a drop with encapsulated ferrofluid [86, 61, 28, 59]. These scenarios may be modeled by incorporating an additional force term into the stroboscopic trajectory equation of Oza *et al.* [80].

The majority of walker studies have been undertaken in the deep-water limit, in which the walker wavefield decays in amplitude before reaching the lower boundary of the bath, so the walker dynamics is uninfluenced by bottom topography. In their study of walker motion in elliptical corrals, Sáenz *et al.* demonstrated the viability of pilot-wave hydrodynamics in shallow water [94]. Furthermore, they demonstrated that, in this shallow-water regime, bottom topography can be used to serve as effective potentials. Specifically, they demonstrated that submerged circular wells act to attract walkers, and so play a role analogous to magnetic impurities in the quantum corrals [67]. Motivated by their insights, we here examine the interaction of a walker with a submerged circular well in an otherwise open system.

We are motivated by an experiment in which a walking droplet interacts with the

wavefield produced by a circular well at the center of the bath. In the deep region, the vibrational acceleration γ exceeds the Faraday threshold γ_F, the critical acceleration above which unstable Faraday waves form on the fluid surface in the absence of the drop. Outside the well, $\gamma < \gamma_F$; thus, the well excites a circularly symmetric Faraday wave across the bath that decays beyond the well. In Chapter 4, we showed that an unstable checkerboard Faraday wave pattern may trap walking droplets, causing them to bounce in place [104]. We investigate here how the well-induced circularly-symmetric Faraday pattern may trap the droplet onto circular orbits.

The stability of circular orbits in a rotating frame [79] and in a harmonic potential [61, 28] have been characterized theoretically using the stroboscopic model of Oza *et al.* [80]. In both settings, an increase in forcing acceleration destabilized circular orbits into wobbling and eventually chaotic orbits. In Chapter 2, we characterized the transition to chaos for both these external forces, as well as for a 2-dimensional Coulomb force [103]. Walking drops acted upon by a Coriolis or Coulomb force underwent a period-doubling cascade, while drops in a harmonic potential became chaotic via a path reminiscent of the Ruelle-Takens-Newhouse scenario [93, 77]. Here, we characterize the transition to chaos for a drop in a circular orbit over a well-induced wavefield. We model the well-induced wave as an oscillatory force field with characteristic wavelength λ_F and a spatial decay rate corresponding to that of a Bessel function.

When the vibrational forcing acceleration is sufficiently high, a droplet will explore the domain of the bath erratically. Provided the memory time is larger than the crossing time of the bath, coherent statistics will emerge in the drop's position probability density function [55, 94]. Durey *et al.* [29] derived that the mean wavefield $\bar{\eta}$ is related to the droplet's stationary probability distribution $\mu(\boldsymbol{x})$ via a convolution with the bouncer wavefield η_B (Theorem 1). Here, we validate this relationship between mean wavefield and position distribution in the case of a particle interacting with a well-induced wavefield. We further characterize numerically the time-scale of convergence to this asymptotic result.

In Section 5.2, we describe the experimental methods and present trajectories of

a droplet walking on a bath with a well-induced wavefield. In Section 5.3, we present the integro-differential equation used to simulate drop trajectories and discuss the numerical methods used. In Section 5.4, we present a generalized pilot-wave framework in which tuning the relative magnitudes of the inertia and wave force terms renders all circular orbits unstable. We investigate the manner in which small circular orbits destabilize for sufficiently high vibrational acceleration, and characterize their transition to chaos. We also examine the relationship between the drop's mean wavefield and its statistics. We discuss the implications of these results and future directions in Section 5.5.

5.2 Experiments

The experimental setup is shown in Fig. 5-1(a). Silicone oil with viscosity $\nu = 20$ cS, surface tension $\sigma = 20.9 \times 10^{-3}$ N/m, and density $\rho = 949$ kg/m^3 fills a circular container with a central well of radius $d = 12$ mm. The fluid depth is $h_1 = 6.5 \pm 0.1$ mm inside the well, and $h_0 = 5.5 \pm 0.1$ mm outside.

The bath is vibrated vertically with frequency $f = 80$ Hz, amplitude A, and acceleration $\Gamma(t) = \gamma \cos(2\pi f t)$, where $\gamma = A(2\pi f)^2$. When the vibrational acceleration of the bath γ exceeds a critical value, the Faraday threshold γ_F, the surface of the bath becomes unstable, and subharmonic waves (with Faraday period $T_F = 2/f$) appear throughout the bath [3]. We note that the Faraday threshold decreases with depth of the fluid bath. Denoting the Faraday thresholds in the deep and shallow regions by γ_F^d and γ_F^s, we operate in a regime such that $\gamma_F^d < \gamma < \gamma_F^s$. Consequently, the deep fluid serves as a source of Faraday waves that decay beyond the well (Fig. 5-1(b)).

The wave number of the most unstable Faraday mode, k_F is obtained from the standard water-wave dispersion relation,

$$\omega_F^2(k) = \left(gk + \frac{\sigma}{\rho}k^3\right)\tanh(kh), \tag{5.1}$$

where $\omega_F = \omega/2 = \pi f$ is the subharmonic angular frequency, and g the gravitational

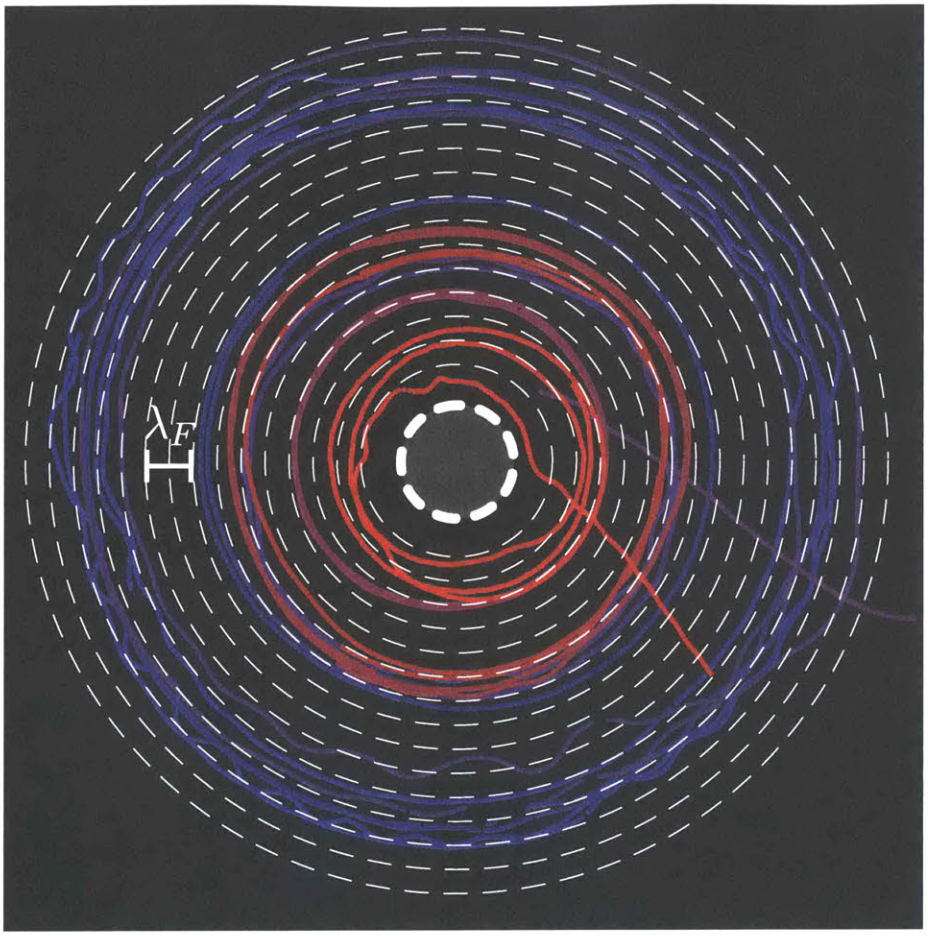

Figure 5-2: Preliminary experimental trajectories of droplets of radius $R = 0.4 \pm 0.01$ mm walking in the Faraday wavefield shown in Fig 5-1(b), with forcing acceleration $\gamma = 4.0$g. The droplets tend to stabilize onto quantized circular orbits, with preferred radii corresponding to half-integer multiples of the Faraday wavelength λ_F. Each color corresponds to a different trajectory, with white dashed lines indicating orbits of half-integer multiples of the Faraday wavelength, $r = (n+1)\lambda_F/2$.

acceleration. Between the shallow ($h_0 = 5.5$ mm) and deep ($h_1 = 6.5$ mm) regions, the Faraday wavelength changes negligibly, taking the values of $\lambda_F = 2\pi/k_F = 4.75 \pm .01$ mm, within measurement errors.

A drop of radius $R = 0.4 \pm 0.01$ mm deposited onto the surface of a vibrating fluid bath bounces indefinitely, provided the vibrational acceleration of the bath γ is sufficiently large. At each impact, the drop generates a circularly symmetric wave centered at its bouncing position. Provided that $\gamma < \gamma_F$, the amplitude of such waves decay in time, with a characteristic time-scale $T_M = T_d/(1 - \gamma/\gamma_F)$, where

$T_d \sim \lambda_F^2/\nu \approx 0.018$ is the decay time of waves in the absence of vibration. As the vibrational acceleration is increased further, the bouncing state destabilizes and the drop begins to walk in response to the gradient of the underlying wavefield. A drop walking below the Faraday threshold performs rectilinear motion in the absence of boundaries and external forces at a free speed prescribed by the balance of the propulsive wave force and a linear drag [72, 80].

In the presence of the well, the walker interacts with a well-induced wavefield. To characterize this interaction, we track the position of droplets walking on the corrugated wavefield (Fig. 5-2). For all initial conditions considered, droplets lock into stable circular orbits. Droplets initially placed in unstable positions wobble until eventually settling onto a stable orbit. Circular orbits are separated by half-integer multiples of the Faraday wavelength $\lambda_F/2$. This spacing may be rationalized by the variability in the vertical phase of the walking droplet at impact: a π-shift in phase is sufficient to change the stability of the orbits. We proceed by investigating the drop's interaction with the well-induced wavefield using the stroboscopic model of Oza *et al.* with an additional topographically induced potential [80, 94].

5.3 Trajectory equation

Building upon the model of Moláček & Bush [72], Oza *et al.* developed an integro-differential trajectory equation to describe the horizontal motion of a droplet of mass m walking on a vibrating fluid bath [80]. The droplet's trajectory, $\boldsymbol{x}_p(t) = (x_p(t), y_p(t))$, is given by

$$m\ddot{\boldsymbol{x}}_p + D\dot{\boldsymbol{x}}_p = mg\nabla h|_{\boldsymbol{x}=\boldsymbol{x}_p(t)} + \boldsymbol{\mathcal{F}}(|\boldsymbol{x}_p(t)|), \tag{5.2}$$

where D is the time-averaged drag coefficient, g the gravitational acceleration, and $\boldsymbol{\mathcal{F}}(|\boldsymbol{x}_p(t)|)$ an externally applied radial force to be specified. Provided the vertical bouncing time-scale T_F is much smaller than the horizontal time-scale $\lambda_F/|\dot{\boldsymbol{x}}|$, or equivalently the drop's vertical speed greatly exceeds its horizontal speed, the wave-

field h may be approximated as an integral:

$$h(\boldsymbol{x},t) = A\int_{-\infty}^{t} J_0\left(k_F\left|\boldsymbol{x}-\boldsymbol{x}_p(s)\right|\right)e^{-(t-s)/T_M}\,\mathrm{d}s, \tag{5.3}$$

where A is the wave amplitude.

If we take the natural length and time-scales to be the Faraday wavelength λ_F and the memory time T_M, we may non-dimensionalize Eq. 5.2 via $\tilde{\boldsymbol{x}} = k_F\boldsymbol{x}$, $\tilde{t} = t/T_M$. Dropping tildes, we obtain the dimensionless equation:

$$\kappa\ddot{\boldsymbol{x}}_p + \dot{\boldsymbol{x}}_p = \beta\int_{-\infty}^{t}\frac{J_1\left(\left|\boldsymbol{x}_p(t)-\boldsymbol{x}_p(s)\right|\right)}{\left|\boldsymbol{x}_p(t)-\boldsymbol{x}_p(s)\right|}\left(\boldsymbol{x}_p(t)-\boldsymbol{x}_p(s)\right)e^{-(t-s)}\,\mathrm{d}s + \tilde{\boldsymbol{\mathcal{F}}}(|\boldsymbol{x}_p(t)|), \tag{5.4}$$

where

$$\kappa = m/DT_M, \quad \beta = Fk_FT_M^2/DT_F \tag{5.5}$$

are respectively the non-dimensional drop inertia and pilot-wave force parameters. $\tilde{\boldsymbol{\mathcal{F}}}(\tilde{\boldsymbol{x}}_p) = k_FT_M\boldsymbol{\mathcal{F}}(\boldsymbol{x}_p)/D$ is the externally-applied force. We note that this corresponds to the Generalized Pilot-wave Framework (GPF) outlined by Bush [14], as will be further explored in Section 5.4.

We proceed by specifying the imposed external force $\boldsymbol{\mathcal{F}}(|\boldsymbol{x}_p(t)|)$ whose form is chosen in order to best match the influence of the well-induced wavefield. We model the well-induced standing Faraday wave as a subharmonic, circularly-symmetric Bessel function of the first kind, with wavelength λ_F: $h_w(\boldsymbol{x},t) = A_wJ_0\left(|k_F\boldsymbol{x}|\right)\sin(\pi ft)$, where A_w is the well-induced wave amplitude. A walking drop in the (2,1) mode resonant with the well-induced wave will experience a normal force prescribed by the gradient of the standing wave, $\boldsymbol{\mathcal{F}}(\boldsymbol{x}_p) = -mg\,\nabla h_w|_{\boldsymbol{x}=\boldsymbol{x}_p(t)}$. In non-dimensional terms, we thus obtain

$$\tilde{\boldsymbol{\mathcal{F}}}(\boldsymbol{x}_p) = QJ_1(|\boldsymbol{x}_p(t)|)\hat{\boldsymbol{r}}, \tag{5.6}$$

where $Q = mgA_wk_F^2T_M\sin(\phi)/D$ is the dimensionless well-induced wave parameter, and $\hat{\boldsymbol{r}}$ the unit radial vector. We solve the integro-differential system (Eq. 5.4) using a fourth-order Adams-Bashforth linear multistep method [83].

Circular orbits of radius r_0 and orbital angular speed ω, $\boldsymbol{x}_p(t) = r_0(\cos(\omega t), \sin(\omega t))$, are solutions to Eq. 5.4 provided they satisfy the following system of algebraic equations:

$$\begin{aligned} -\kappa r_0 \omega^2 =& \beta \int_0^\infty J_1\left(2r_0 \sin\left(\frac{\omega z}{2}\right)\right) \sin\frac{\omega z}{2} e^{-z}\,\mathrm{d}z + Q J_1(r_0) \\ r_0 \omega =& \beta \int_0^\infty J_1\left(2r_0 \sin\left(\frac{\omega z}{2}\right)\right) \cos\frac{\omega z}{2} e^{-z}\,\mathrm{d}z. \end{aligned} \tag{5.7}$$

We solve Eq. 5.7 in order to obtain the values of ω and Q corresponding to various initial radii r_0. We initialize the simulations assuming circular orbits of radius r_0 for time $t < 0$. At $t = 0$, we impose an external force given by Eq. 5.6, and solve the system using a non-dimensional time-step $\Delta t/T_M = 2^{-8}$. Fig. 5-3 displays trajectories simulated for $\gamma/\gamma_F = 0.9$, superimposed on the wavefield observed experimentally. We see that the radii of stable, quantized orbits deduced numerically correspond roughly to the extrema of the well-induced Faraday wavefield, indicating that the external force proposed in Eq. 5.6 is sufficient to capture the behavior observed experimentally. We note that trajectories initialized at unstable radii wobble until eventually tending to a stable circular orbit, as in experiments. For the forcing accelerations ($0.85 < \gamma/\gamma_F < 0.99$) and initial radii ($0.1 < r_0/\lambda_F < 3$) considered, trajectories always settled into stable orbital solutions, corresponding to extrema of the imposed Bessel function.

5.4 Generalized pilot-wave framework

One can imagine much richer system behavior, including chaotic switching between unstable orbits, as has been observed in a number of hydrodynamic quantum analogues [55, 52, 43, 94]. With a view to observing transitions to unstable regimes, we thus proceed by exploring a generalized pilot-wave framework, where the externally applied force $\boldsymbol{\mathcal{F}}$ and system parameters β and κ may be altered relative to those of the fluid system. Particular attention will be given to characterizing how circular orbits destabilize and quantum-like statistics emerge.

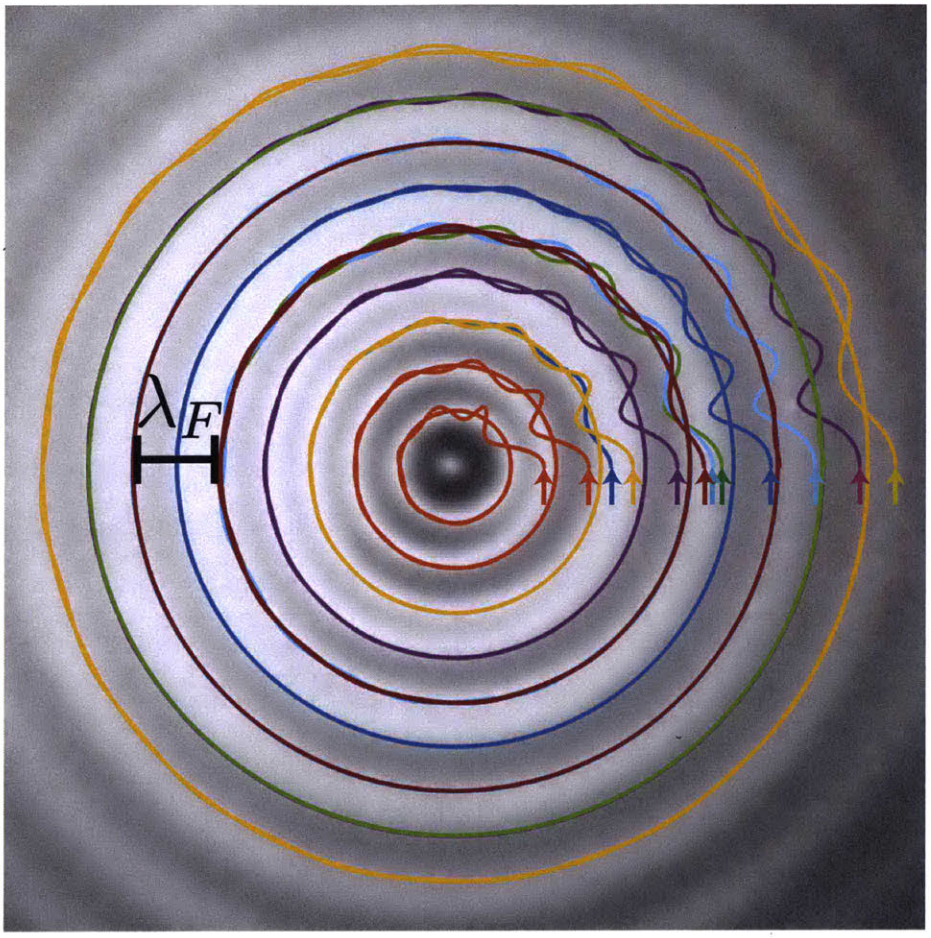

Figure 5-3: Droplet trajectories calculated from the stroboscopic model (Eq. 5.2) with an additional oscillatory force prescribed by Eq. 5.6, superimposed on the experimental wavefield from Fig. 5-1(b). Trajectories were initialized in circular orbits with various initial radii, indicated by colored arrows. After small oscillations, all trajectories converged onto stable quantized orbits separated by half-integer multiples of the Faraday wavelength λ_F.

In order to destabilize the circular orbits observed in simulations of droplets walking in an oscillatory potential (Fig. 5-3), we introduce an additional force term into the stroboscopic model (Eq. 5.4). Specifically, we consider a radial force arising from a harmonic potential, $\boldsymbol{\mathcal{F}}(\boldsymbol{x}_p) = -k\boldsymbol{x}_p$, where k is the non-dimensional spring constant, and explore the resulting dynamics. As we vary the relative magnitudes of the spring and wave force coefficients, k and Q, circular orbits may become unstable. For a fixed value of the spring constant $k = 0.1$, we note that lowering Q prompts a transition from stable to wobbling, and eventually, chaotic orbits, as detailed in Fig. 5-4.

5.4.1 Transition to chaos

We here detail the manner in which smaller circular trajectories ($r/\lambda_F \sim 0.5$) transition to chaos in this generalized pilot-wave system with oscillatory and harmonic potentials. We consider fixed values of the spring constant $k = 0.1$ and well-induced wave force coefficient $Q = 0.3$. We vary non-dimensional parameters β and κ according to the vibrational forcing acceleration γ/γ_F in a manner prescribed by Eq. 5.5. We increase the forcing acceleration gradually and analyze the stability of the resulting orbits. The transition to chaos for smaller orbits is summarized in Fig. 5-4, where columns correspond respectively to the particle's trajectory, the radius as a function of time, and frequency decomposition of the radius signal.

We initialize the drop in a stable circular orbit of radius $r/\lambda_F = 0.5$ and $\gamma/\gamma_F = 0.94$, and introduce a small non-dimensional perturbation $\delta x/\lambda_F = 0.01$ at $t = 0$. We track the drop radius as a function of time; for stable circular orbits, the initial perturbation decays exponentially and the drop radius tends to a constant. As γ/γ_F is increased gradually, the circular orbit destabilizes. For $\gamma/\gamma_F > 0.945$, the initial perturbation grows exponentially until eventually settling to a non-linear wobbling state (Fig. 5-4(a)). The orbital radius wobbles periodically between two values, with a wobbling frequency $f_1 \approx 2f_0$, where f_0 is the orbital frequency. When $\gamma/\gamma_F \sim 0.963$ (Fig. 5-4(b)), a second frequency f_2 emerges in the power spectrum, with $f_2/f_1 \approx 0.24$. The lower frequency corresponds to the slow modulation in the radius signal. The amplitude of the modulation increases with γ/γ_F, reaching its maximal value at

$\gamma/\gamma_F = 0.9667$ (Fig. 5-4(c)). Finally, for $\gamma/\gamma_F > 0.9668$, the orbit becomes chaotic, as suggested by the broadband frequency spectrum shown in Fig. 5-4(d).

5.4.2 Emerging statistics

We may further explore the generalized pilot-wave framework by altering the dependence of the pilot-wave force β, and the inertial coefficient κ parameters relative to those arising in the fluid system ($\kappa \in [0, 1.5]$, $\beta \in [1, 500]$ for $\gamma/\gamma_F < 0.985$). In particular, we seek a parameter regime characterized by unstable orbits between which walkers switch chaotically. We focus on a pilot-wave system in the large-β, low-κ regime, where the non-dimensional wave force is significantly larger than the non-dimensional inertial term. Physically, this corresponds to a particle with lower mass than the droplets generating a higher-amplitude wave. Although not realizable in a hydrodynamic setting, this regime is known to exhibit additional quantum features. For example, Oza *et al.* [81] showed that hydrodynamic spin states characterized by a drop spontaneously orbiting in its own wavefield [63, 79] are stable in this regime.

At low forcing acceleration $\gamma/\gamma_F = 0.95$ (corresponding to $\beta = 40.5$, $\kappa = 0.35$ via Eq. 5.5) all orbits are stable, as those shown in Fig. 5-3. As the forcing acceleration is increased, circular orbits tend to become unstable. We note that smaller orbits destabilize more rapidly, as seen in Fig 5-5. In this case, an orbit is perturbed from an initial radius $r_0/\lambda_F \sim 1.5$ at $\gamma/\gamma_F = 0.97$ and the drop begins to wobble, with an amplitude that increases until the drop reaches the next-largest stable radius, $r/\lambda_F \sim 2.5$. The growth of the wobbling amplitude and eventual stabilization at the next orbital radius are evident in the time series of $r(t)$ reported Fig. 5-5(b). We note that wave-like statistics begin to emerge in the drop's radial position probability density function (Fig 5-5(c)); however a steady state is never reached, due to the short-lived transient.

In Fig. 5-6(a), we see a trajectory simulated at $\gamma/\gamma_F = 0.98$ ($\beta = 252.8$, $\kappa = 0.14$) where a structure of concentric rings appears in the drop's trajectory indicating the preferred orbital radii. We track the drop's radial position as a function of time (Fig. 5-6(b)), which indicates that the radius does not change monotonically; rather,

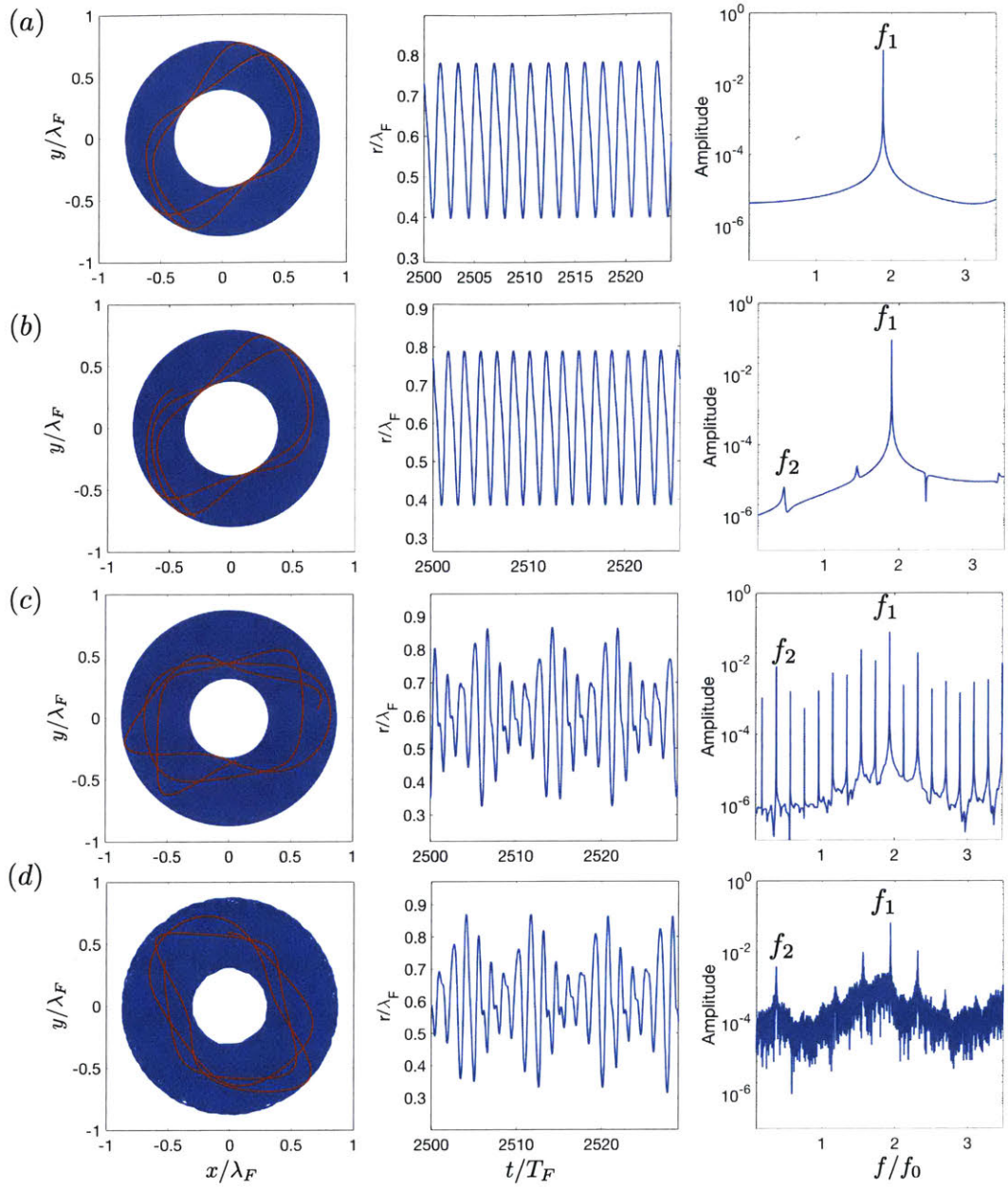

Figure 5-4: The first column corresponds to the simulated trajectories of walking droplets in a generalized pilot-wave framework with $Q = 0.3$, $k = 0.1$. A few orbital periods are highlighted in red. The second column shows the radius of the drop as a function of time, with corresponding frequency spectrum in the third column. (a) The onset of wobbling at $\gamma/\gamma_F = 0.945$, where the wobbling frequency is approximately twice the orbital frequency. $f_1 \approx 2f_0$. (b) A second frequency f_2 appears at $\gamma/\gamma_F \sim 0.963$, corresponding to small-amplitude modulations in wobbling. (c) $\gamma/\gamma_F = 0.9667$. (d) The wobbling state destabilizes when $\gamma/\gamma_F > 0.9668$, being replaced by a chaotic trajectory characterized by a broadband frequency spectrum. We note that the transition to chaos occurs over a narrow range of $\Delta\gamma/\gamma_F$, requiring high numerical precision beyond that attainable experimentally.

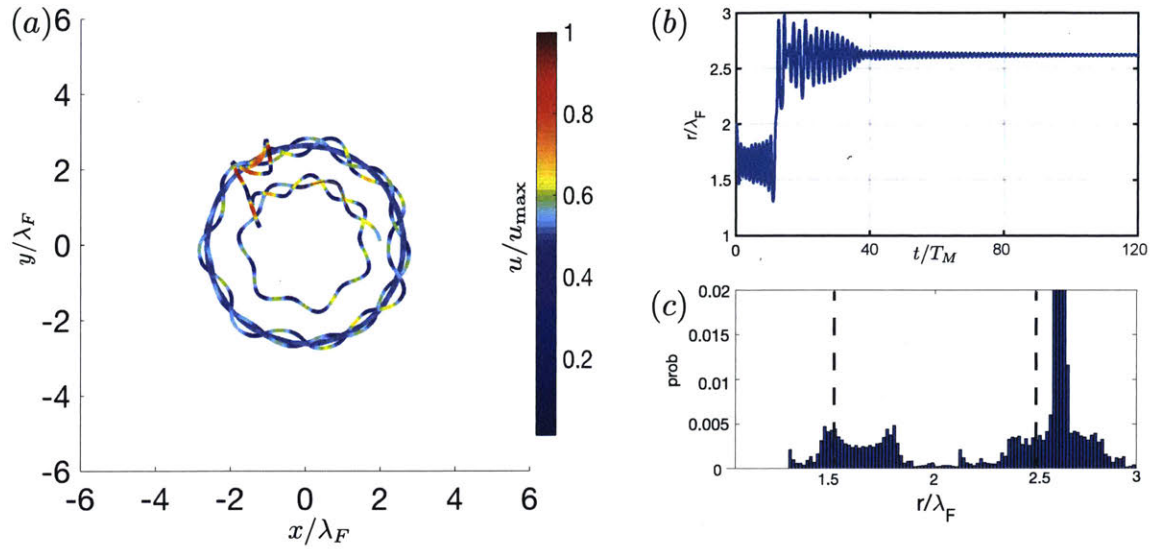

Figure 5-5: An orbit initialized at an unstable radial position ($r_0/\lambda_F = 1.5$) wobbles until settling onto a larger stable radius. (a) Trajectory of a single drop with $\kappa = 0.14$, $\beta = 252.8$, simulated from Eq. 5.4 with $\gamma/\gamma_F = 0.97$, $Q = 0.3$, and $k = 0.1$, with time step $\Delta t/T_M = 2^{-8}$ and total time $t_{\max}/T_M = 120$. The trajectory is color-coded according to drop speed. (b) The corresponding radius as a function of time and (c) the probability distribution. The transient state is short-lived, with the drop locking onto the next largest orbital state ($r/\lambda_F \sim 2.5$).

it jumps from small to large orbits and back again. The droplet eventually settles into a stable circular orbit of radius $r/\lambda_F \approx 4.5$, after approximately $t/T_M \sim 170$. The preferred radial positions during the transient motion are evident in the drop's radial probability density function shown in Fig. 5-6(c). The preferred radii are half-integer multiples of the Faraday wavelength $(n+1)\lambda_F/2$, which correspond to those of stable orbits at lower forcing accelerations γ.

We then lower the inertial non-dimensional coefficient $\tilde{\kappa} = 0.7\kappa$, while maintaining the pilot-wave force β as that obtained from fluid parameters with $\gamma/\gamma_F = 0.98$. Specifically, $\tilde{\kappa} = 0.042$ and $\beta = 252.8$. The simulated trajectories are shown in Fig. 5-7(a). Once again, the concentric-ring structure in the particle trajectory highlights the preferred orbital radii. In this case, however, all orbits are unstable, and the droplet switches chaotically between them. We record the orbital radius as a function of time (Fig. 5-7(b)), and the corresponding radial probability distribution (Fig. 5-7(c)). In this chaotic regime, wave-like statistics emerge in the probability density function.

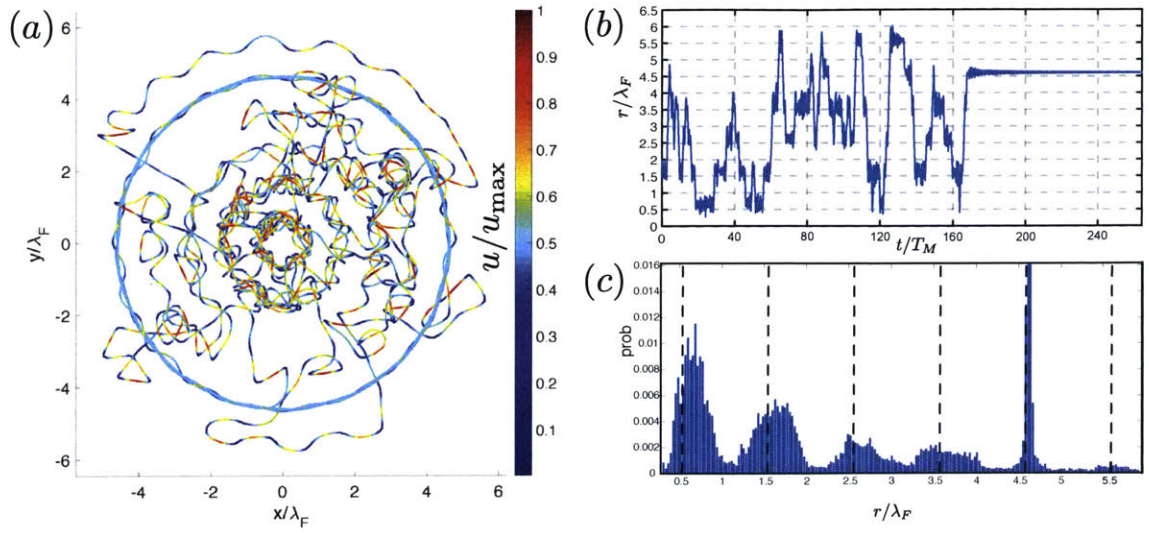

Figure 5-6: Transient approach to a stable orbit deduced numerically from the generalized pilot-wave framework. (a) A single drop with $\kappa = 0.14$, $\beta = 252.8$, simulated from Eq. 5.4 with $\gamma/\gamma_F = 0.98$, $Q = 0.3$, and $k = 0.1$, with time step $\Delta t/T_M = 2^{-8}$ and total time $t_{\max}/T_M = 250$. The trajectory is color-coded according to drop speed. (b) Corresponding radius as a function of time and (c) probability distribution. During its long transient, the drop explores 6 orbitals before locking onto the second largest ($r/\lambda_F \sim 4.5$).

The p.d.f. saturates after approximately $t/T_M \sim 200$ indicating the time-scale of approach to a statistically steady state. Thereafter, the p.d.f. reflects the relative instability of the unstable circular orbits.

5.4.3 Mean pilot-wave field

Durey *et al.* [29] demonstrated that, for unbounded systems such as this, the mean wavefield $\bar{\eta}(\boldsymbol{x})$ is related to the emerging statistics through the convolution:

$$\bar{\eta}(\boldsymbol{x}) = \int_{\mathcal{R}^2} \eta_B(\boldsymbol{x} - \boldsymbol{y})\mu(\boldsymbol{y})\,\mathrm{d}\boldsymbol{y}, \tag{5.8}$$

where $\eta_B(\boldsymbol{x})$ is the wavefield of a bouncer at the origin (Fig 5-8(a)) and $\mu(\boldsymbol{x})$ is the steady probability density function for the drop's position. We proceed by computing the mean wavefield analytically for a periodic orbit, and characterizing numerically the convergence time-scale of this result for chaotic orbits in our generalized pilot-

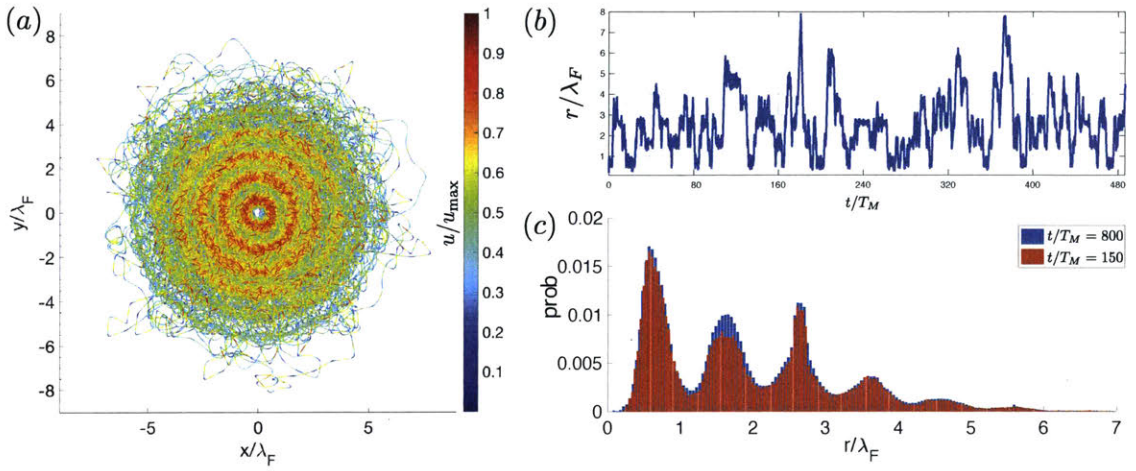

Figure 5-7: (a) Trajectory of a walker switching chaotically between unstable orbits, as obtained from simulations of our generalized pilot-wave framework. The non-dimensional inertia $\tilde{\kappa} = 0.042$ and pilot-wave force $\beta = 152.8$ were tuned to render all circular orbits unstable. The trajectory is color-coded according to drop speed. (b) Radial position of the droplet as a function of time displays no periodicity. (c) The probability distribution of the drop's radial position indicates the relative instability of the unstable circular orbits. We note that the p.d.f. saturates after approximately $t/T_M \sim 200$, thereafter, there is no significant change in the wave-like structure of the statistics.

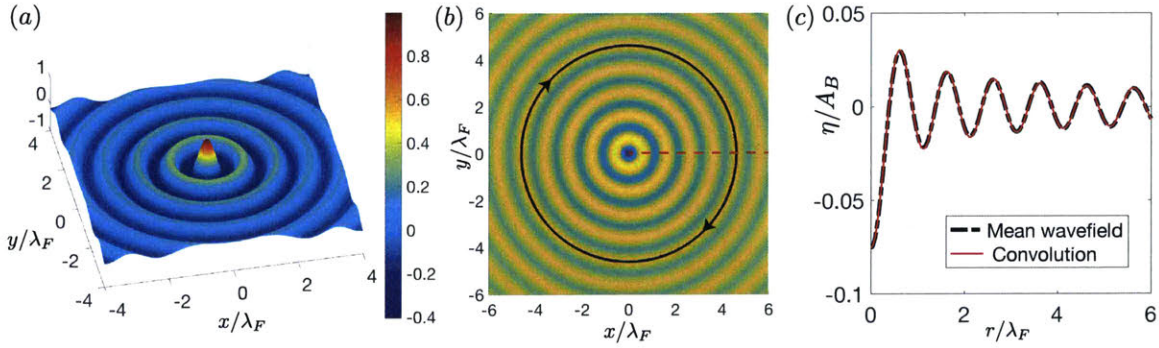

Figure 5-8: (a) Non-dimensionalized wavefield of a bouncer at the origin, $\eta_B(\boldsymbol{x})/A_B$, computed from Eq. 5.3 with $\boldsymbol{x}_p(t) = \mathbf{0}$. (b) A stable circular trajectory with radius $r/\lambda_F \sim 4.5$ obtained following the transient state shown in Fig. 5-6(a) is superimposed onto the convolution of a bouncer wavefield and the steady pdf, given by a radial δ-function. (c) A radial section comparing the mean wavefield computed numerically to the convolution result (Eq. 5.9), for a stable circular trajectory after a time $t/T_M \sim 50$.

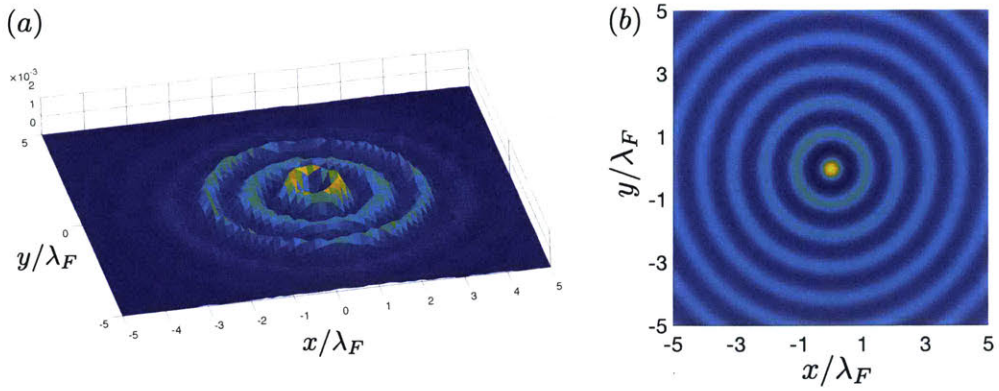

Figure 5-9: The statistics and mean wavefield of the trajectory shown in Fig. 5-7(a). (a) Probability density function for droplet position, $\mu(\boldsymbol{x})$, generated from simulations of the generalized pilot-wave (Eq. 5.4) with non-dimensional drop inertia $\kappa = 0.042$ and pilot-wave force $\beta = 152.8$. The peaks of the wave-like statistics correspond to extrema of the well-induced potential. In this parameter regime, all circular orbits are unstable and the drop switches chaotically between them. (b) The convolution of bouncer wavefield and drop's p.d.f. [29], $\eta_B(\boldsymbol{x}) * \mu(\boldsymbol{x})$ after $t/T_M = 800$ is computed from Eq. 5.8. It is indistinguishable from the mean wavefield computed numerically.

wave framework. In particular, we show numerically the existence of a steady-state probability density function for a chaotic orbit.

We first consider the steady-state circular orbit that emerges following the transient behavior depicted in Fig. 5-6(a). In the case of a stable periodic circular orbit of radius $r_0 \sim 4.5\lambda_F$ (Fig. 5-8(b)), the radial probability distribution is given by $\mu(\boldsymbol{x}) = \delta(|\boldsymbol{x}| - r_0)/2\pi r_0$. Since both the steady probability distribution and bouncer wavefield are radially symmetric, we may perform the required convolution (Eq. 5.8) analytically in polar coordinates:

$$\frac{\bar{\eta}(r)}{A_B} = \int_{\mathcal{R}^2} \frac{J_0(\sqrt{r^2+\rho^2-2r\rho\cos(\theta)})\delta(\rho - r_0)}{2\pi r_0} \rho \, \mathrm{d}\rho \, \mathrm{d}\theta$$

Using the identity [111]

$$J_0(\sqrt{r^2+\rho^2-2r\rho\cos(\theta)}) = \sum_{m=0}^{\infty} \epsilon_m J_m(r) J_m(\rho) \cos(m\theta),$$

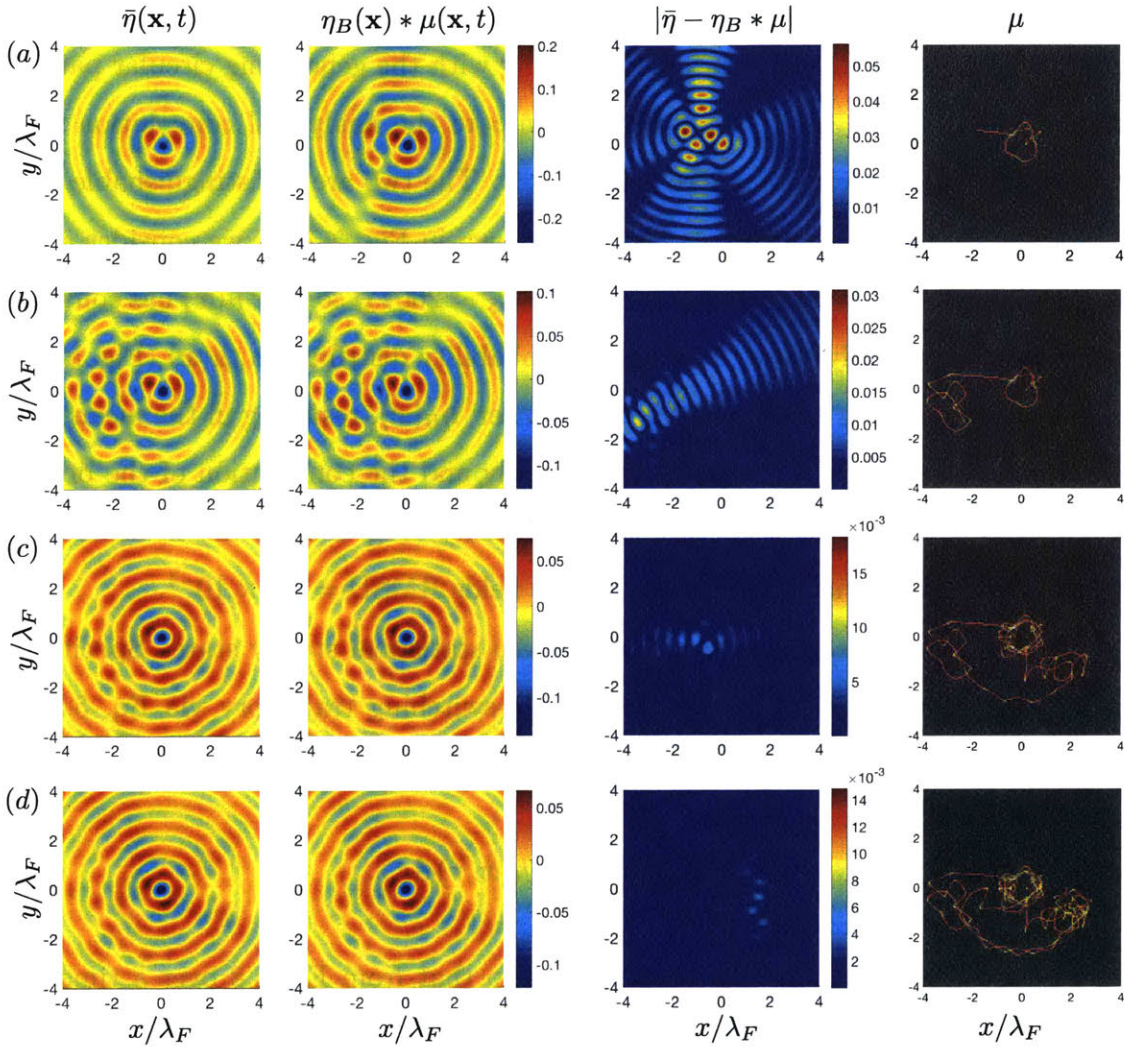

Figure 5-10: First column: Mean wavefield $\bar{\eta}(\boldsymbol{x}, t)$ for the chaotically-switching trajectory (Fig. 5-7). Second column: Convolution of steady probability density function $\mu(\boldsymbol{x}, t)$ with stationary wavefield of a bouncer $\eta_B(\boldsymbol{x})$. Third column: Absolute error $|\bar{\eta}(\boldsymbol{x}, t) - \mu(\boldsymbol{x}, t) * \eta_B(\boldsymbol{x})|$. Fourth column: Probability density function of the drop $\mu(\boldsymbol{x}, t)$ We track the evolution of these quantitites as a function of time for (a) $t/T_M = 3.5$, (b) $t/T_M = 8.2$, (c) $t/T_M = 22.3$, (d) $t/T_M = 34.0$.

with $\epsilon_0 = 1, \epsilon_m = 2$ for $m \neq 0$ yields the simple result

$$\bar{\eta}(r) = A_B J_0(r) J_0(r_0). \tag{5.9}$$

The mean wavefield has the form of $J_0(r)$ and an amplitude prescribed by the orbital radius r_0. The resulting convolution field along with the generating circular path are shown in Fig. 5-8(b). In Fig. 5-8(c), we compare the analytical convolution result with the mean wavefield computed numerically. The two are indistinguishable.

For the chaotically-switching trajectory shown in Fig. 5-7(a), we consider a time greater than the statistical relaxation time $t > \tau_S \sim 200 T_M$ so that $\mu(\boldsymbol{x})$ has converged to a statistically steady state. The steady probability distribution, $\mu(\boldsymbol{x})$ (Fig. 5-9(b)) is then convolved with the wavefield of a bouncer, $\eta_B(\boldsymbol{x})$, resulting in the mean wavefield $\bar{\eta}(\boldsymbol{x})$. The wavefield computed numerically and the convolution of the bouncer wavefield (Fig 5-8(a)) with the probability density (Fig. 5-9(a)) are in accord: the root-mean square deviation between the two fields RMSD $= 2.2 \times 10^{-4}$.

We now consider the evolution towards the statistical steady state. Specifically, we calculate the wavefield for the chaotically-switching trajectory via Eq. 5.3 and compute the resulting average wavefield numerically:

$$\bar{\eta}(\boldsymbol{x}, t) = \frac{1}{t} \int_0^t h(\boldsymbol{x}, \tau) \, \mathrm{d}\tau. \tag{5.10}$$

The average wavefield in Eq. 5.10 converges to that from Eq. 5.8 over a time-scale $\tau_S / T_M \sim 200$, the time-scale of statistical relaxation. In Fig 5-10(a), we show the computed mean wavefield $\bar{\eta}(\boldsymbol{x}, t)$, the convolution between the bouncer wavefield with the particle's probability density function, the absolute error between the two quantities, and the particle's probability density function μ at time $t/T_M = 3.5$. At early times, there are discrepancies between the two fields, since the mean wavefield is dominated by the most recent impacts, and the particle has not explored a significant portion of the domain. At $t/T_M = 8.2$ (Fig 5-10(b)), the two quantities are qualitatively similar, with minor wave-like traces evident in the absolute error, in the vicinity of the walker. As the drop explores a larger portion of the domain, as seen at

later times $t/T_M = 22.3$ (Fig 5-10(c)) and $t/T_M = 34.0$ (Fig 5-10(d)), the two fields $\bar{\eta}$ and $\eta_B * \mu$ are effectively identical, with the error between them tending to zero globally.

5.5 Discussion

We have explored the horizontal dynamics of walking droplets subject to an attractive oscillatory potential. Experiments of a droplet walking on the surface of a bath with a topographically-induced Faraday wavefield demonstrate the existence of stable quantized orbits with intra-orbital spacing $\lambda_F/2$. The radial quantization was also observed in simulations using an integro-differential trajectory equation with an imposed oscillatory potential applied to model the influence of the underlying wavefield. Similar orbital stability characteristics were observed numerically in the parameter regime explored experimentally.

We then considered a generalized pilot-wave system where the magnitudes of the drop's inertia κ and pilot-wave force β may be tuned independently, and altered relative to those appropriate for the fluid system. We also considered an applied harmonic potential in order to obtain unstable circular orbits and the resulting transition to chaos. Circular orbits destabilize into wobbling, precessing, and finally chaotic orbits. The transition from stable circular orbits to chaos is reminiscent of the Ruelle-Takens-Newhouse scenario [93, 77, 30]. In this generalized framework, there are regions in parameter space (κ, β) where all circular orbits become unstable. In this regime, drops switch chaotically between them. The corresponding probability density for the drop's radial position shows the emergence of wave-like statistics that assume a stationary form after a time-scale $\tau_S/T_M \sim 200$.

We also confirmed numerically the result of Durey *et al.* that the drop's mean wavefield is related to the emergent statistics via a convolution with the wavefield of a bouncer for both periodic and chaotic trajectories [29]. We showed that this asymptotic behavior converges rapidly over the statistical relaxation time-scale $\tau_s \sim T_M$.

Chapter 6

Concluding remarks

> *I think that when this interpretation [de Broglie's Pilot-wave theory] is further elaborated, extended, and eventually modified in some of its aspects, it will lead to a better understanding of the true coexistence of waves and particles about which actual Quantum mechanics only gives statistical information, often correct, but in my opinion incomplete.*
>
> – Louis de Broglie, 1987 [20].

We have considered the dynamics and statistics of droplets walking on the surface of a vertically-vibrating fluid bath. This hydrodynamic system represents the first realization of a pilot-wave system of the form envisioned by de Broglie [19]. The two key components of de Broglie's pilot-wave theory present in the hydrodynamic pilot-wave system are the monochromatic pilot wave, and the resonant interaction between the wave and particle. We have explored the dynamics of walking droplets subjected to various external forces and fields through an integrated experimental and theoretical approach. Particular attention has been given to deducing conditions for the trapping of walkers by an ambient wavefield, and to characterizing the transitions to chaos in orbital pilot-wave dynamics.

Our investigation of droplet behavior above the Faraday threshold was motivated by a desire to introduce a stochastic element into the drop dynamics, as has been posited for quantum particles by Nelson [74], Bohm & Vigier [9], and de Broglie [20].

In Stochastic Electrodynamics [74, 12, 48], the zero-point electromagnetic field serves as a source of fluctuations. According to de la Peña & Cetto [21, 22] in their modern version of de Broglie's mechanics, these fluctuations serve only to excite the particle vibration at its natural frequency, $mc^2/\hbar$, and have no further influence on the particle's dynamics. Likewise, in the walker system, the background is important only in exciting the drop vibration (bouncing) and the resulting monochromatic wavefield. In a number of settings, we have seen that chaotic pilot-wave dynamics may suffice to account for quantum-like statistics.

In our experimental characterization of droplet dynamics above the Faraday threshold, we observed a variety of novel dynamical states. At the onset of the Faraday instability, droplets would meander or zig-zag, surfing the troughs of the unstable Faraday wave. In the rare cases where the drop synchronized with the ambient wavefield, it would become trapped, bouncing at a local extremum of the underlying wave. More generally, droplets bouncing on this corrugated Faraday wavefield moved erratically, exhibiting behavior analogous to a 2D random walk. The diffusive properties observed for drops bouncing erratically above the Faraday threshold were purely classical, with the root-mean-square displacement scaling linearly with time. We note that all current theoretical frameworks for computing the droplet's horizontal dynamics assume the superposition of linear waves with a temporal decay, an assumption that breaks down above the Faraday threshold. The characterization of droplets bouncing and walking above the Faraday threshold was purely experimental, since an accompanying theoretical treatment would require consideration of non-linear wave effects.

In quantum mechanics, an initially localized wave-packet corresponding to a free particle with speed $\hbar |\boldsymbol{k}| /m$ diffuses ballistically, such that its variance scales as the square of time, $\sigma^2 \sim t^2$. This behavior may be simply interpreted in terms of rectilinear motion of an ensemble of identically-prepared individual particles whose initial positions and momenta satisfy Heisenberg's uncertainty relation $\Delta p \Delta x \geq \hbar/2$: the variance in this ensemble's position density function grows in a manner consistent with ballistic diffusion. The base state of the walker, corresponding to rectilinear

motion at the free-walking speed, is thus not a shortcoming of the hydrodynamic system as a quantum analog.

We have also reported a hydrodynamic optical analog arising above the Faraday threshold, namely the Faraday-Talbot effect. An array of equally-spaced circular pillars protruding from the fluid surface generates waves provided the vibrational acceleration is slightly above the Faraday threshold. The resulting wave superposition exhibits a coherent structure, with self-images forming at integer multiples of the Faraday-Talbot length. The result is a hydrodynamic analog of the optical Talbot effect [101, 116], where a monochromatic electromagnetic wave is modulated by a spatially periodic structure, generating an array of self-images in the near-field. We further demonstrated that drops may become trapped, bouncing at the troughs of the Faraday-Talbot wave field. We have thus presented a hydrodynamic analog of particle trapping with the Talbot effect [76, 98, 68].

We have provided the first theoretical characterization of the transition from periodic circular orbits to chaotic dynamics in orbital pilot-wave dynamics. We note that this transition arose over a remarkably small range of $\Delta\gamma \sim 0.005$; consequently, its characterization was well beyond existing experimental precision. Orbital motion in the presence of external Coriolis or Coulomb force transitioned from a periodic to chaotic motion through a period-doubling cascade, while circular orbits in the presence of a harmonic potential became chaotic through a path reminiscent of the Ruelle-Takens-Newhouse scenario. Although the mechanism for the transition to chaos depends on the form of the externally-applied force, we observed similar statistical forms emerging from the resulting chaotic trajectories. In particular, in the fully chaotic regime, trajectories switch between unstable periodic states, with the residence time in each state indicating their relative instability [79, 85, 62, 28]. One thus sees the manner in which chaotic pilot-wave dynamics might account for quantum-like statistics.

We exploited the fact that pilot-wave hydrodynamics is viable in shallow water, as discovered by Sáenz *et al.* [94], and so explored the possibility of walker trapping using variations in bottom topography. In particular, we considered a bath with a

central circular well that induces a circularly-symmetric Faraday wave pattern. We demonstrated that walking droplets become trapped on circular orbits whose radii correspond to the extrema of the well-induced wavefield. For the fluid parameters considered, quantized orbital trajectories were stable with a characteristic spacing of approximately $\lambda_F/2$, indicating that walker trapping in a well-induced wavefield is robust.

The hydrodynamic pilot-wave system has provided a new vehicle for extending the range of classical systems to include behavior previously associated with quantum systems. Nevertheless, the walker system does have its limitations; in particular, certain quantum-like features cannot be captured with fluid-like parameters. For example, self-orbiting spin states are observed to be unstable [63], as has been rationalized via the stroboscopic model [79, 81]. With a view to extending the phenomenological range of the hydrodynamic pilot-wave system, we considered a generalized pilot-wave framework, in which the relative magnitudes of the pilot-wave force and drop inertia could be altered relative to those achievable in the fluid system. Using this generalized pilot-wave framework, we extended our experimental study of well-induced trapping by considering a walker subjected to both oscillatory and harmonic potentials.

With this generalized framework, we have shown that orbital trapped states, such as those reported in Chapter 5, may be rendered unstable and eventually chaotic. From these chaotic trajectories, we observed the emergence of wave-like statistics that converge to a statistically steady state for times greater than the statistical relaxation time τ_s, which scales with the memory time. We computed the mean wavefield numerically, and compared it with the convolution of the drop's probability density function and a bouncer wavefield, testing the validity of the theoretical result deduced by Durey *et al.* [29]. We noted the rapid convergence of the mean wavefield to the convolution result for both periodic and chaotic trajectories. The relation between the particle's dynamics and statistics in this pilot-wave system provides an important step towards a hydrodynamic interpretation of quantum dynamics, where a particle's position and momentum exist independent of measurement, and non-local quantum interactions may be rationalized in terms of wave-mediated effects.

Existing theoretical models [80, 71, 72] used throughout this thesis provide a well-benchmarked framework for exploring hydrodynamic systems consisting of a single particle in the absence of boundaries. Our study has made clear the value of extending this theoretical framework beyond that governing the fluid system. The generalized pilot-wave framework has allowed us to extend the phenomenological range of pilot-wave systems beyond that achievable in the laboratory. The development and exploration of further extensions would thus seem a fruitful direction for future research. Possibilities include further exploration of non fluid-like parameters. Efforts are underway to incorporate variable vertical dynamics through extension of the stroboscopic models to include the dependence of bouncing phase on local wave amplitude. One might also explore different wave forms, including different forms of spatio-temporal damping. Finally, we envisage an extension of the stroboscopic model to three-dimensional space, where a pulsating particle is guided by a spherically-symmetric pilot-wavefield.

We expect that future work will firm up the new links established between a drop's dynamics and emerging statistics. A clear objective is the derivation of a Schrödinger-like equation for the particle's statistics that is consistent with an underlying chaotic deterministic dynamics. Further characterization of this macroscopic pilot-wave system may help bridge the gap between quantum and classical realms, restoring a realist view of quantum mechanics similar to that originally envisioned by Louis de Broglie. Sensing that the plethora of quantum interpretations was incomplete, Bush [14] concocted his own:

> *[...] the Many-Many-Worlds Interpretation, according to which each quantum interpretation is realized in some edition of the multimultiverse, and there is even one world in which there is only one world [...] and beables be.*

My hope is that *this* is that world, the edition of the multimultiverse where beables just be.

Bibliography

[1] L. E. Ballentine. The statistical interpretation of quantum mechanics. *Review Modern Physics*, 42:358–381, 1970.

[2] J. S. Bell. *Speakable and unspeakable in quantum mechanics.* Cambridge University Press, 1988.

[3] T. B. Benjamin and F. Ursell. The stability of the plane free surface of a liquid in vertical periodic motion. *Proceedings of the Royal Society A*, 225:505–515, 1954.

[4] M. V. Berry, R G Chambers, M. D. Large, C. Upstill, and J. C. Walmsley. Wavefront dislocations in the Aharonov-Bohm effect and its water wave analogue. *European Journal of Physics*, 1(3):154, 1980.

[5] M. V. Berry and S. Klein. Integer, fractional and fractal Talbot effects. *Journal of Modern Optics*, 43(10):2139–2164, 1996.

[6] F. Blanchette. Modeling the vertical motion of drops bouncing on a bounded fluid reservoir. *Physics of Fluids*, 28(3), 2016.

[7] D. Bohm. A suggested interpretation of the quantum theory in terms of hidden variables, I. *Physical Review*, 85:166–179, 1952.

[8] D. Bohm and B. J. Hiley. The de Broglie pilot wave theory and the further development of new insights arising out of it. *Foundations of Physics*, 12(10):1001–1016, 1982.

[9] D. Bohm and J. P. Vigier. Model of the causal interpretation of quantum theory in terms of a fluid with irregular fluctuations. *Physical Review*, 96:208–216, 1954.

[10] N. Bohr. *Essays 1958-1962 on Atomic Physics and Human Knowledge.* Ox Bow Press, 1963.

[11] Max Born. Nobel lecture: The statistical interpretations of quantum mechanics, 1954.

[12] T. H. Boyer. Any classical description of nature requires classical electromagnetic zero-point radiation. *American Journal of Physics*, 79:1163–1167, 2011.

[13] J. W. M. Bush. The new wave of pilot-wave theory. *Physics Today*, 68:47, 2015.

[14] J. W. M. Bush. Pilot-wave hydrodynamics. *Annual Review of Fluid Mechanics*, 49:269–292, 2015.

[15] W. B. Case, M. Tomandl, S. Deachapunya, and M. Arndt. Realization of optical carpets in the Talbot and Talbot-Lau configurations. *Optics Express*, 17(23):20966–20974, 2009.

[16] M. S. Chapman, C. R. Ekstrom, T. D. Hammond, J. Schmiedmayer, B. E. Tannian, S. Wehinger, and D. E. Pritchard. Near-field imaging of atom diffraction gratings: The atomic Talbot effect. *Physics Review A*, 51:R14–R17, 1995.

[17] Y. Couder, S. Protière, E. Fort, and A. Boudaoud. Dynamical phenomena: Walking and orbiting droplets. *Nature*, 437(208), 2005.

[18] L. de Broglie. On the theory of quanta. *Annales de Physique, 10*, 3, 1925.

[19] L. de Broglie. *Ondes et mouvements.* Gauthier-Villars, 1926.

[20] L. de Broglie. Interpretation of quantum mechanics by the double solution theory. *Annales de la Fondation Louis de Broglie*, 12(4), 1987.

[21] L. de la Peña and A. M. Cetto. *The quantum dice: an introduction to stochastic electrodynamics.* Kluwer Academic, 1996.

[22] L. de la Peña, A.M. Cetto, and A.V. Hernández. *The Emerging Quantum: The Physics Behind Quantum Mechanics.* Springer International Publishing, 2014.

[23] B. C. Denardo, J. J. Puda, and A. Larraza. A water wave analog of the Casimir effect. *American Journal of Physics*, 77(12):1095–1101, 2009.

[24] L. Deng, E. W. Hagley, J. Denschlag, J. E. Simsarian, Mark Edwards, Charles W. Clark, K. Helmerson, S. L. Rolston, and W. D. Phillips. Temporal, matter-wave-dispersion Talbot effect. *Physical Review Letters*, 83:5407–5411, 1999.

[25] B. S. DeWitt and N. Graham. *The Many-Worlds Interpretation of Quantum Mechanics.* Princeton University Press, 2015.

[26] S. Douady. Experimental study of the Faraday instability. *Journal of Fluid Mechanics*, 221:383–409, 1990.

[27] H. Dukas and V. V. Raman. Albert Einstein: The Human Side. *American Journal of Physics*, 47:1107–1107, 1979.

[28] M. Durey and P. A. Milewski. Faraday wave-droplet dynamics: discrete-time analysis. *Journal of Fluid Mechanics*, 821:296–329, 2017.

[29] M. Durey, P. A. Milewski, and J. W. M. Bush. Mean wave field effects and emerging statistics of Faraday pilot-waves. Submitted.

[30] J.-P. Eckmann. Roads to turbulence in dissipative dynamical systems. *Reviews of Modern Physics*, 53(4):643, 1981.

[31] A. Eddi, E. Fort, F. Moisy, and Y. Couder. Unpredictable tunneling of a classical wave-particle association. *Physical Review Letters*, 102(240401), 2009.

[32] A. Eddi, E. Sultan, J. Moukhtar, E. Fort, M. Rossi, and Y. Couder. Information stored in Faraday waves: the origin of path memory. *Journal of Fluid Mechanics*, 675:433–463, 2011.

[33] A. Eddi, D. Terwagne, E. Fort, and Y. Couder. Wave propelled ratchets and drifting rafts. *Europhysics Letters*, 82(4):44001, 2008.

[34] A. Einstein, M. Born, and H. Born. Born-Einstein Letters. 1971.

[35] A. Einstein, B. Podolsky, and N. Rosen. Can quantum-mechanical description of physical reality be considered complete? *Physical review*, 47(10):777, 1935.

[36] H. Everett. "Relative State" Formulation of Quantum Mechanics. *Review of Modern Physics*, 29:454–462, 1957.

[37] M. Faraday. On a peculiar class of acoustical figures, and on certain forms assumed by groups of particles upon vibrating elastic surfaces. *Philosophical Transactions of the Royal Society of London*, 121:299–340, 1831.

[38] L. M. Faria. A model for Faraday pilot waves over variable topography. *Journal of Fluid Mechanics*, 811:51–66, 2017.

[39] B. Filoux, M. Hubert, P. Schlagheck, and N. Vandewalle. Walking droplets in linear channels. *Physical Review Fluids*, 2:013601, 2017.

[40] P.J. Flory. *Statistical mechanics of chain molecules.* Interscience Publishers, 1969.

[41] E. Fort, A. Eddi, A. Boudaoud, J. Moukhtar, and Y. Couder. Path-memory induced quantization of classical orbits. *Proceedings of the National Academy of Sciences*, 107(41):17515–17520, 2010.

[42] T. Gilet. Dynamics and statistics of wave-particle interactions in a confined geometry. *Physical Review E*, 90:052917, 2014.

[43] T. Gilet. Quantumlike statistics of deterministic wave-particle interactions in a circular cavity. *Physical Review E*, 93:042202, 2016.

[44] T. Gilet and J. W. M. Bush. The fluid trampoline: droplets bouncing on a soap film. *Journal of Fluid Mechanics*, 625:167–203, 2009.

[45] J. P. Gollub and S. V. Benson. Many routes to turbulent convection. *Journal of Fluid Mechanics*, 100(3):449–470, 1980.

[46] J. P. Gollub and H. L. Swinney. Onset of turbulence in a rotating fluid. *Physical Review Letters*, 35(14):927, 1975.

[47] C. L. Goodridge, W. T. Shi, H. G. E. Hentschel, and D. P. Lathrop. Viscous effects in droplet-ejecting capillary waves. *Physical Review E*, 56:472–475, 1997.

[48] G. Grössing, S. Fussy, J. Mesa Pascasio, and H. Schwabl. Elements of subquantum thermodynamics: quantum motion as ballistic diffusion. *Journal of Physics: Conference Series*, 306(1):012046, 2011.

[49] M. C. Gutzwiller. Periodic orbits and classical quantization conditions. *Journal of Mathematical Physics*, 12(3):343–358, 1971.

[50] A. M. Guzmán and C. H. Amon. Transition to chaos in converging–diverging channel flows: Ruelle–Takens–Newhouse scenario. *Physics of Fluids*, 6(6), 1994.

[51] D. M. Harris. *The pilot-wave dynamics of walking droplets in confinement.* Thesis, Massachusetts Institute of Technology. Department of Mathematics, 2015.

[52] D. M. Harris and J. W. M. Bush. Droplets walking in a rotating frame: from quantized orbits to multimodal statistics. *Journal of Fluid Mechanics*, 739:444–464, 2014.

[53] D. M. Harris and J. W.M. Bush. Generating uniaxial vibration with an electrodynamic shaker and external air bearing. *Journal of Sound and Vibration*, 334:255 – 269, 2015.

[54] D. M. Harris, T. Liu, and J. W. M. Bush. A low-cost, precise piezoelectric droplet-on-demand generator. *Experiments in Fluids*, 56(4):83, 2015.

[55] D. M. Harris, J. Moukhtar, E. Fort, Y. Couder, and J. W. M. Bush. Wavelike statistics from pilot-wave dynamics in a circular corral. *Physical Review E*, 88(011001), 2013.

[56] J. Hietarinta and S. Mikkola. Chaos in the one-dimensional gravitational three-body problem. *Chaos: An Interdisciplinary Journal of Nonlinear Science*, 3(2):183–203, 1993.

[57] G. Jannes, R. Piquet, P. Maïssa, C. Mathis, and G. Rousseaux. Experimental demonstration of the supersonic-subsonic bifurcation in the circular jump: A hydrodynamic white hole. *Physical Review E*, 83:056312, 2011.

[58] K. Kumar. Linear theory of Faraday instability in viscous fluids. *Proceedings of the Royal Society A*, 452:1113–1126, 1996.

[59] K. M. Kurianski, A. U. Oza, and J. W. M. Bush. Simulations of pilot-wave dynamics in a simple harmonic potential. *Physical Review Fluids*, 2:113602, 2017.

[60] M. Labousse. *Etude d'une dynamique à mémoire de chemin: une expérimentation théorique.* Thesis, Université Pierre et Marie Curie - Paris VI, 2014.

[61] M. Labousse, A. U. Oza, S. Perrard, and J. W. M. Bush. Pilot-wave dynamics in a harmonic potential: Quantization and stability of circular orbits. *Physical Review E*, 93:033122, 2016.

[62] M. Labousse and S. Perrard. Non-Hamiltonian features of a classical pilot-wave dynamics. *Physical Review E*, 90(022913), 2014.

[63] M. Labousse, S. Perrard, Y. Couder, and E. Fort. Self-attraction into spinning eigenstates of a mobile wave source by its emission back-reaction. *Physical Review E*, 94:042224, 2016.

[64] M. Lockwood. 'Many Minds' Interpretations of Quantum Mechanics. *The British Journal for the Philosophy of Science*, 47(2):159–188, 1996.

[65] E.N. Lorenz. *The Essence Of Chaos.* Jessie and John Danz lectures. Taylor & Francis, 1995.

[66] E. Madelung. The hydrodynamical picture of quantum theory. *Zeitschrift für Physik*, 40:322–326, 1926.

[67] H. C. Manoharan, C. P. Lutz, and D. M. Eigler. Quantum mirages formed by coherent projection of electronic structure. *Nature*, 403:512–515, 2000.

[68] C. Mennerat-Robilliard, D. Boiron, J. M. Fournier, A. Aradian, P. Horak, and G. Grynberg. Cooling cesium atoms in a Talbot lattice. *Europhysics Letters*, 44(4):442–448, 1998.

[69] J. Miles and D. Henderson. Parametrically forced surface waves. *Annual Review of Fluid Mechanics*, 22:143–165, 1990.

[70] P. Milewski, C. Galeano-Rios, A. Nachbin, and J. W. M. Bush. Faraday pilot-wave dynamics: modelling and computation. *Journal of Fluid Mechanics*, 778:361–388, 2015.

[71] J. Moláček and J. W. M. Bush. Drops bouncing on a vibrating bath. *Journal of Fluid Mechanics*, 727:582–611, 2013.

[72] J. Moláček and J. W. M. Bush. Drops walking on a vibrating bath: towards a hydrodynamic pilot-wave theory. *Journal of Fluid Mechanics*, 727:612–647, 2013.

[73] A. Nachbin, P. A. Milewski, and J. W. M. Bush. Tunneling with a hydrodynamic pilot-wave model. *Physical Review Fluids*, 2:034801, 2017.

[74] E. Nelson. Review of stochastic mechanics. *Journal of Physics: Conference Series*, 361(1):012011, 2012.

[75] J. Neumann. *Mathematische Grundlagen der Quantenmechanik.* Grundlehren der mathematischen Wissenschaften. Springer Berlin Heidelberg, 1932.

[76] R. Newell, J. Sebby, and T. G. Walker. Dense atom clouds in a holographic atom trap. *Optics Letters*, 28(14):1266–1268, 2003.

[77] S. Newhouse, D. Ruelle, and F. Takens. Occurrence of strange axiom A attractors near quasi periodic flows on T^m, $m \geq 3$. *Communications in Mathematical Physics*, 64(1):35–40, 1978.

[78] I. Newton. *Opticks, Or, A Treatise of the Reflections, Refractions, Inflections & Colours of Light.* Dover Books on Physics. Dover Publications, 1952.

[79] A. U. Oza, D. M. Harris, R. R. Rosales, and J. W. M. Bush. Pilot-wave dynamics in a rotating frame: on the emergence of orbital quantization. *Journal of Fluid Mechanics*, 744:404–429, 2014.

[80] A. U. Oza, R. R. Rosales, and J. W. M. Bush. A trajectory equation for walking droplets: hydrodynamic pilot-wave theory. *Journal of Fluid Mechanics*, 737:552–570, 2013.

[81] A. U. Oza, R. R. Rosales, and J. W. M. Bush. Hydrodynamic spin states. Submitted.

[82] A. U. Oza, E. Siéfert, D. M. Harris, J. Moláček, and J. W. M. Bush. Orbiting pairs of walking droplets: Dynamics and stability. *Physical Review Fluids*, 2:053601, 2017.

[83] A. U. Oza, Ø. Wind-Willassen, D. M. Harris, R. R. Rosales, and J. W. M. Bush. Pilot-wave hydrodynamics in a rotating frame: Exotic orbits. *Physics of Fluids*, 26(082101), 2014.

[84] S. Perrard. *A wave-mediated memory: Eigenstates, Chaos and Probabilities.* Thesis, Université Paris Diderot, 2014.

[85] S. Perrard, M. Labousse, E. Fort, and Y. Couder. Chaos driven by interfering memory. *Physical Review Letters*, 113(104101), 2014.

[86] S. Perrard, M. Labousse, M. Miskin, E. Fort, and Y. Couder. Self-organization into quantized eigenstates of a classical wave-driven particle. *Nature Communications*, 5(3219), 2014.

[87] H. Poincaré and F. Maitland. *Science and Method.* Dover books on science. Dover Publications, 1958.

[88] S. Protière, A. Boudaoud, and Y. Couder. Particle-wave association on a fluid interface. *Journal of Fluid Mechanics*, 554:85–108, 2006.

[89] G. Pucci, D. M. Harris, L. M. Faria, and J. W. M. Bush. Walking droplets interacting with single and double slits. *Journal of Fluid Mechanics*, 835:1136–1156, 2018.

[90] B. A. Puthenveettil and E. J. Hopfinger. Evolution and breaking of parametrically forced capillary waves in a circular cylinder. *Journal of Fluid Mechanics*, 633:355–379, 2009.

[91] A. Rahman and D. Blackmore. Neimark-Sacker bifurcations and evidence of chaos in a discrete dynamical model of walkers. *Chaos, Solitons & Fractals*, 91:339 – 349, 2016.

[92] Lord Rayleigh. On copying diffraction-gratings, and on some phenomena connected therewith. *Philosophical Magazine*, 11(67):196–205, 1881.

[93] D. Ruelle and F. Takens. On the nature of turbulence. *Communications in Mathematical Physics*, 20(3):167–192, 1971.

[94] P. J. Sáenz, T. Cristea-Platon, and J. W. M. Bush. Statistical projection effects in a hydrodynamic pilot-wave system. *Nature Physics*, 2017.

[95] J. J. Sakurai and J. J. Napolitano. *Modern Quantum Mechanics (2nd Edition)*. Pearson, 2010.

[96] M. Schlosshauer, J. Kofler, and A. Zeilinger. A snapshot of foundational attitudes toward quantum mechanics. *ArXiv e-prints*.

[97] T. Shinbrot, C. Grebogi, J. Wisdom, and J. Yorke. Chaos in a double pendulum. *American Journal of Physics*, 60:491–491, 1992.

[98] Y. Y. Sun, X.-C. Yuan, L. S. Ong, J. Bu, S. W. Zhu, and R. Liu. Large-scale optical traps on a chip for optical sorting. *Applied Physics Letters*, 90(3):031107, 2007.

[99] N. Sungar, J. P. Sharpe, J. J. Pilgram, J. Bernard, and L. D. Tambasco. Faraday-Talbot effect: Alternating phase and circular arrays. *submitted to Chaos: An Interdisciplinary Journal of Nonlinear Science*, 2018.

[100] N. Sungar, L. D. Tambasco, G. Pucci, P. J. Sáenz, and J. W. M. Bush. Hydrodynamic analog of particle trapping with the talbot effect. *Physical Review Fluids*, 2:103602, 2017.

[101] H.F. Talbot. Facts relating to optical science. *Philosophical Magazine*, 9(56):401–407, 1836.

[102] L. D. Tambasco and J. W. M. Bush. Exploring orbital dynamics and trapping with a generalized pilot-wave framework. *submitted to Chaos: An Interdisciplinary Journal of Nonlinear Science*, 2018.

[103] L. D. Tambasco, D. M. Harris, A. U. Oza, R. R. Rosales, and J. W. M. Bush. The onset of chaos in orbital pilot-wave dynamics. *Chaos: An Interdisciplinary Journal of Nonlinear Science*, 26(10):103107, 2016.

[104] L. D. Tambasco, J. J. Pilgram, and J. W. M. Bush. Bouncing droplet dynamics above the Faraday threshold. *submitted to Chaos: An Interdisciplinary Journal of Nonlinear Science*, 2018.

[105] Max Tegmark. Many lives in many worlds. *Nature*, 448:23, 2007.

[106] D. Terwagne, T. Gilet, N. Vanderwalle, and S. Dorbolo. Metastable bouncing droplets. *Physics of Fluids*, 21(054103), 2009.

[107] F. J. Torcal-Milla, L. M. Sanchez-Brea, F. J. Salgado-Remacha, and E. Bernabeu. Self-imaging with curved gratings. *Optics Communications*, 283(20):3869 – 3873, 2010.

[108] S. E. Turton, M. M. P. Couchman, and J. W. M. Bush. A review of the theoretical modeling of walking droplets: towards a generalized pilot-wave framework. Submitted.

[109] W. G. Unruh. Experimental black-hole evaporation. *Physical Review Letters*, 46:1351–1353, 1981.

[110] J. Walker. Drops of liquid can be made to float on the liquid. What enables them to do so? *Scientific American*, 238-6:151–158, 1978.

[111] G. N. Watson. *A Treatise on the Theory of Bessel Functions (Cambridge Mathematical Library)*. Cambridge University Press, 1922.

[112] T. Weitkamp, A. Diaz, C. David, F. Pfeiffer, M. Stampanoni, P. Cloetens, and E. Ziegler. X-ray phase imaging with a grating interferometer. *Optics Express*, 13(16):6296–6304, 2005.

[113] J. Wen, Y. Zhang, and M. Xiao. The Talbot effect: recent advances in classical optics, nonlinear optics, and quantum optics. *Advances in Optics and Photonics*, 5(1):83–130, 2013.

[114] G.B. Whitham. *Linear and Nonlinear Waves*. Pure and Applied Mathematics: A Wiley Series of Texts, Monographs and Tracts. Wiley, 2011.

[115] Ø. Wind-Willassen, J. Moláček, D. M. Harris, and J. W. M. Bush. Exotic states of bouncing and walking droplets. *Physics of Fluids*, 25(082002), 2013.

[116] E. Wolf and K. Patorski. *Progress in Optics*. Number v. 27 in Progress in optics. North-Holland, 1989.

[117] T. Young. The Bakerian lecture: Experiments and calculations relative to physical optics. *Philosophical Transactions of the Royal Society of London*, 94:1–16, 1804.

[118] W. Zhang and J. Viñals. Pattern formation in weakly damped parametric surface waves. *Journal of Fluid Mechanics*, 336:301–330, 1997.

[119] W. Zhang, J. Wang, Y. Cui, and S. Teng. Talbot effect of curved grating. *Optics Communications*, 341:245 – 251, 2015.

[120] W. Zhang, C. Zhao, J. Wang, and J. Zhang. An experimental study of the plasmonic Talbot effect. *Optics Express*, 17(22):19757–19762, 2009.